Continuum Modeling of Mixed Conductors: a Study of Ceria

Thesis by

Francesco Ciucci

In Partial Fulfillment of the Requirements

for the Degree of

Doctor of Philosophy

California Institute of Technology

Pasadena, California

2009

(Defended June 6, 2009)

to my loving family

Acknowledgements

I am very thankful I had a chance to attend Caltech in spite of the many neurological diseases that have struck my advisors, first Fred Culick then Dave Goodwin. At Caltech I met many remarkable people, some of whom will be my friends forever, and I was exposed to a wide research spectrum, only a fraction of my work is written here.

I would like to thank my now former advisor Prof. Dave Goodwin for his continuous help and support through the duration of my thesis work. Dave Goodwin is a true gentleman and I will always be thankful for what he has taught me.

I am greatly indebted to Prof. Colonius for serving as chair of my commitee and for his advice and support through difficult times.

I would like to thank Prof. Haile for serving on my committee panel, for reading this thesis and for coauthoring a paper with William Chueh and me. I wish to thank Prof. Melany Hunt and Prof. Joe Shepherd for their advice, for serving on my committee and for reading this thesis.

I am particular indebted to my collaborators William Chueh, Yong Hao, Tomonori Honda and Maria Yang; it has been an honor working with you guys! My group-mates Jeff Hanna and Vaughan Thomas have also been instrumental in this process. So thank you too.

I wish to express my sincere gratitude to my father Gabriele, my mother Donatella and

my sister Sara, for their love, support, patience and encouragement.

Finally I wish to thank my beautiful mate Mariapaola for bearing with me and for making me smile when it was most needed. Her presence alone has helped me in countless ways.

Abstract

In this thesis we have derived a new way to analyze the impedance response of mixed conducting materials for use in solid oxide fuel cells (SOFCs), with the main focus on anodic materials, in particular cerium oxides.

First we have analyzed the impact of mixed conductivity coupled to electrocatalytic behavior in the linear time-independent domain for a thick ceria sample. We have derived that, for a promising fuel cell material, Samarium Doped Ceria, chemical reactions are the determining component of the polarization resistance.

As a second step we have extended the previous model to the time-dependent case, where we focused on single harmonic excitation, the impedance spectroscopy conditions. We extended the model to the case where some input diffusivities are spatially nonuniform. For instance we considered the case where diffusivities change significantly in the vicinity of the electrocatalytic region.

As a third and final step we use to model to capture the two dimensional behavior of mixed conducting thin films, where the electronic motion from one side of the sample to the other is impeded. Such conditions are similar to those encountered in fuel cells where an electrolyte conducting exclusively oxygen ions is placed between the anode and the cathode. The framework developed was also extended to study a popular cathodic material, Lanthanum Manganite.

The model is used to give unprecedented insight in SOFC polarization resistance analysis of mixed conductors. It helps elucidate rigorously rate determining steps and to address the interplay of diffusion with diffusion losses. Electrochemical surface losses dominate for most experimental conditions of Samarium Doped Ceria and they are shown to be strongly dependent on geometry.

List of Figures

List of Tables

Nomenclature

α Ratio of the maximum allowable vacancy concentration and the bulk vacancy concentration, page 20

α_{ion} Ratio between near interface and bulk diffusivity of vacancies, page 93

$\bar{n}$ ratio of bulk electrons to dopant, page 20

$\bar{p}$ ratio of bulk vacancies to dopant, page 20

χ_{chem} Volume specific chemical capacitance, page 44

$\Delta\hat{V}$ Fourier transform of the bias, page 40

ΔH_r Reduction enthalpy of the electrochemical reaction $O_O^x \rightleftharpoons V_O^{\bullet\bullet} + \frac{1}{2}O_2(\text{gas}) + 2e'$, page 8

ΔS_r Reduction entropy of the electrochemical reaction $O_O^x \rightleftharpoons V_O^{\bullet\bullet} + \frac{1}{2}O_2(\text{gas}) + 2e'$, page 8

ΔV Bias or electric potential drop, page 40

$\dot{\Omega}_{eon}$ Net volumetric rate of generation of electrons, page 18

$\dot{\omega}_{eon}$ Flux of electrons into the bulk as a result of reactions occurring at the boundary between gas and mixed conducting phase, page 28

$\dot{\Omega}_{ion}$ Net volumetric rate of generation of vacancies, page 18

$\dot{\omega}_{ion}$ Flux of vacancies into the bulk as a result of reactions occurring at the boundary between gas and mixed conducting phase, page 28

Γ_1 Symmetry center line, page 23

Γ_2 Translational symmetry line, page 23

Γ_3 Translational symmetry line, page 23

Γ_4 Interface between the metal and the mixed conductor, page 23

Γ_5 Interface between the gas phase and the mixed conductor, page 23

$\hat{\phi}^{(1)}$ Fourier transform of the first order perturbation of the dimensionless electric potential, page 35

$\hat{I}$ Fourier transform of the current, page 40

$\hat{j}^{(1)}$ Fourier transform of the small AC current, page 79

$\hat{n}^{(1)}$ Fourier transform of the first order perturbation of the dimensionless electron concentration, page 35

$\hat{n}^{(1)}_{\mathrm{DL}}$ Fourier transform of the double layer correction of the dimensionless electron concentration, page 103

$\hat{n}^{(1)}_{\mathrm{EN}}$ Fourier transform of the dimensionless electron concentration computed using the electroneutral approximation, page 103

$\hat{n}^{(1)}_{\mathrm{FULL}}$ Fourier transform of the dimensionless electron concentration, page 103

$\hat{p}^{(1)}_{\mathrm{DL}}$ Fourier transform of the double layer correction of the dimensionless vacancy concentration, page 103

$\hat{p}^{(1)}_{\mathrm{EN}}$ Fourier transform of the dimensionless vacancy concentration computed using the electroneutral approximation, page 103

$\hat{p}^{(1)}_{\mathrm{FULL}}$ Fourier transform of the dimensionless vacancy concentration, page 103

$\hat{p}hi^{(1)}_{\mathrm{DL}}$ Fourier transform of the double layer correction of the dimensionless electric potential, page 103

$\hat{p}hi^{(1)}_{\mathrm{EN}}$ Fourier transform of the dimensionless electric potential computed using the electroneutral approximation, page 103

$\hat{p}hi^{(1)}_{\mathrm{FULL}}$ Fourier transform of the dimensionless electric potential, page 103

$\hat{q}$ Total charge per unit of surface area of the layer, page 106

$\hat{V}^{(1)}$ Fourier transform of the small AC bias, page 79

λ_D Debye length, page 19

$\mathbf{x}$ $(x,\ y,\ z)$ space coordinates, page 20

ν Average distance between 1D and 2D solution in frequency space at a given horizontal slice, page 87

ν Total distance between 1D and 2D solution in frequency space at a given horizontal slice, page 87

ϕ Electric potential, page 17

ρ Charge density, page 18

σ_m Conductivity of species m, page 10

σ_T Total conductivity, page 10

σ_{eon} Conductivity of electrons, page 10

σ_{ion} Conductivity of vacancies, page 10

τ Characteristic timescale of diffusion, page 19

τ_n Characteristic timescale of electronic diffusion, page 19

τ_p Characteristic timescale of vacancy diffusion, page 19

$\tilde{\mu}_m$ Electrochemical potential of species m, page 16

$\tilde{\mu}^{\star}_m$ Star electrochemical potential of species m, i.e., the electrochemical potential of m divided by the elementary charge of m, page 19

$\tilde{\mu}_{eon}$ Electrochemical potential of electrons, page 19

$\tilde{\mu}^{\star}_{eon}$ Electrochemical potential of species electrons, page 19

$\tilde{\mu}_{ion}$ Electrochemical potential of vacancies, page 19

$\tilde{\mu}^{\star}_{ion}$ Electrochemical potential of species vacancies, page 19

$\tilde{\phi}$ Dimensionless electrical potential, page 20

$\tilde{A}_{\phi}$ Dimensionless proportionality constant for the Chang-Jaffé condition on the derivative of the dimensionless electric potential $\tilde{\phi}^{(1)}$, page 30

$\tilde{A}_n$ Dimensionless proportionality constant for the Chang-Jaffé condition on the derivative of the dimensionless electron concentration $n^{(1)}$, page 30

$\tilde{k}^0_f$ Dimensionless forward rate of the reaction $H_2(\text{gas}) \rightleftharpoons H_2O(\text{gas}) + V_O^{\bullet\bullet} + 2e'$, page 28

$\tilde{p}_k$ Dimensionless partial pressure of species k, page 24

$\tilde{t}$ Dimensionless time, page 20

$\tilde{\mathbf{x}}$ $(\tilde{x},\ \tilde{y},\ \tilde{z})$ dimensionless space coordinates, page 20

$\triangle$ $\frac{\partial^2}{\partial x^2} + \frac{\partial^2}{\partial y^2} + \frac{\partial^2}{\partial z^2}$ Laplacian, page 20

$\triangle_{\tilde{x}}$ $\frac{\partial^2}{\partial \tilde{x}^2} + \frac{\partial^2}{\partial \tilde{y}^2} + \frac{\partial^2}{\partial \tilde{z}^2}$ Dimensionless Laplacian, page 20

ε Permittivity of the medium, page 18

ε_F Relative distance between the 1D and the 2D impedance, page 81

A_ϕ Proportionality constant for the Chang-Jaffé condition on the derivative of the dimensionless electric potential $\tilde{\phi}^{(1)}$, page 30

A_n Proportionality constant for the Chang-Jaffé condition on the derivative of the dimensionless electron concentration $n^{(1)}$, page 30

B Background negative charge concentrations, page 19

C Capacitance, page 40

c_m Concentration of species, page 17

C_{chem} Chemical resistance, page 46

c_{eon} Electron concentration, page 18

c_{ion} Vacancy concentration, page 18

c_{ion}^{MAX} Maximum concentration of vacancies, page 19

C_{surf} Surface capacitance, page 108

D_m Diffusivity of species m, page 17

D_{eon} Diffusivity of electrons, page 18

D_{ion} Diffusivity of vacancies, page 18

e Elementary charge of an electron, page 17

e' Electron in the lattice, page 11

f_{eon-DD} Fraction of the area specific resistance due to the electronic drift-diffusion, page 60

f_{pol} Fraction of the area specific resistance due to the polarization effects, page 65

f_{surf} Fraction of the area specific resistance due to surface reactions, page 60

I Current, page 40

I_e^{CP} Electron cross plane current, page 57

I_g^{CP} Vacancy cross plane current, page 57

I_g^{IP} Electron in-plane current, page 57

j_m^P Particle flux of species m, page 16

j_{eon}^P Flux of electrons, page 18

j_{ion}^P Flux of vacancies, page 18

k_B Boltzmann Constant, page 16

k_f Forward rate of the reaction $H_2(\text{gas}) \rightleftharpoons H_2O(\text{gas}) + V_O^{\bullet\bullet} + 2e'$, page 28

K_g Equilibrium constant of the gas phase chemical reaction $H_2(\text{gas}) + O_2(\text{gas}) \rightleftharpoons H_2O(\text{gas})$, page 24

K_r Equilibrium constant of the electrochemical reaction $O_O^x \rightleftharpoons V_O^{\bullet\bullet} + \frac{1}{2}O_2(\text{gas}) + 2e'$, page 11

k_r Reverse rate of the reaction $H_2(\text{gas}) \rightleftharpoons H_2O(\text{gas}) + V_O^{\bullet\bullet} + 2e'$, page 28

L Inductance, page 40

l_2 Thickness of the mixed conductor, page 55

l_c Characteristic length scale of the sample, page 19

n Dimensionless electron concentration (n is for negative), page 20

O_O^x Oxygen site in the lattice, page 11

p Dimensionless vacancy concentration (p is for positive), page 20

p_k Dimensional partial pressure of species k, page 24

Q Charge, page 40

R Resistance, page 40

R_{avg} Portion of the area specific resistance due to the averaging, page 59

R_{eon-DD} Portion of the area specific resistance due to the electronic drift-diffusion, page 59

R_{eon} Electronic resistance, page 45

R_{ion} Vacancy resistance, page 45

$R_{ion}^{\perp}$ Area specific resistance, page 58

R_{pol} Portion of the area specific resistance due to the actual polarization effects, page 59

R_{surf} Portion of the area specific resistance due to the surface reaction, page 59

T Temperature, page 17

t Time, page 20

u_m Mobility of species m, page 10

u_{eon} Mobility of electrons, page 10

u_{ion} Mobility of vacancies, page 10

$V_O^{\bullet\bullet}$ Vacant oxygen site in the lattice, page 11

W_1 Half width of the current collector mixed conductor interface, page 55

W_2 Half width of the mixed conductor interface exposed to the gas, page 55

z_m Integer charge of species m, page 17

Z_{2D} Impedance for the 2D model at a given pressure and temperature, page 79

Z_{GFLW} Impedance of the Generalized Finite-Length Warburg Element (GFLW), page 41

$\mathbf{x}_+$ The singular perturbation coordinates, page 105

Contents

Chapter 1

Introduction

In this thesis we develop novel analytical and numerical methods for the study of solid oxide fuel cells (SOFCs). The goal of this work is to understand the chemistry and the physics of SOFCs and to develop first-principles tools that will eventually aid their design.

Work in electrochemical energy conversion systems is not only intellectually stimulating, but it is also very relevant for the well-being of humanity because a cheap, environmentally friendly, and reliable energy supply is a core requirement for our society. Given rising energy prices, dwindling oil supplies, the presence of hydrocarbon resources in unstable countries and imminent threats of global warming*, governments and industries require better ways to convert fuels into electrical energy. Electrochemical devices make this conversion directly, and they could play a pivotal role in increasing efficiency.

Solid Oxide Fuel Cells (SOFCs) are currently the most efficient devices to directly convert the chemical energy of a fuel into electrical energy [SK03]. In cogeneration systems for stationary power generation and thermal energy distribution, themodynamical efficiencies up to 75% can be achieved, much higher than for gas turbines and internal combustion

*Recent events have sparked interest in global warming among economists. The Nobel winning Economist Paul Krugman recently wrote in the New York Times [Kru09]: "...The scientific consensus on prospects for global warming has become much more pessimistic over the last few years. Indeed, the latest projections from reputable climate scientists border on the apocalyptic. Why? Because the rate at which greenhouse gas emissions are rising is matching or exceeding the worst-case scenarios. And the growth of emissions from China, already the worlds largest producer of carbon dioxide, is one main reason for this new pessimism..."

engines. Solid oxide fuel cells have the great advantage over other fuel cells, such as Proton Exchange Membrane (PEM) fuel cells, of being fuel flexible: they work on hydrogen, methanol, ethanol, methane, propane, coal-derived syngas etc. SOFCs are characterized by higher operating temperatures (600^oC - 1000^oC) than PEM fuel cells and hold promise for use in a wide variety of applications, ranging from powering small electronic devices to large cogeneration systems.

Due to their high efficiency, fuel flexibility and scalability, SOFC could replace combustion systems in the near future. In the medium term, hydrogen could serve as a way to store energy from the sun to be used at night. To this end, researchers are developing more efficient ways to split water with sunlight [LN06]. If we assume that producing hydrogen from water using solar energy will someday be profitable, then SOFCs will be the technology of choice to generate electrical power from hydrogen and, if needed, with hydrocarbon fuels. The latter fuels are expected to be employed in the future because of their high energetic content per unit volume under standard conditions and because they can be generated in an environmentally friendly way. Hydrocarbon fuels can be produced from biomass, or synthetic hydrocarbons can be produced by reaction of hydrogen with atmospheric CO_2 [BSBR06].

Despite their promise, SOFCs that are still too costly[†]. With few exceptions, most SOFC industrial work is a variation on half-a-century-old designs; for example the Ni/YSZ (Yttrium Stabilized Zirconia) cermet anodes used in the vast majority of SOFCs do not differ qualitatively from those submitted for patenting by Spacil in 1964 [Spa70]. Empirical improvements over the years have been made, but the basic designs have not changed

[†]The Department of Energy's Solid State Energy Conversion Alliance (SECA) set 60% efficiency and the \$400/kW cost target of the SECA Program by 2010. Costs in 2003 were estimated by [SK03] to be between \$1000/kW and \$2000/kW. If these goals are met, the cost of electricity can be projected to \$0.048/kWh for a SOFC-Gas Turbine system, still 20% above the cost of wind energy, around \$0.038/kWh [oE09].

significantly over the past few decades and, again, SOFC technology is not yet profitable.

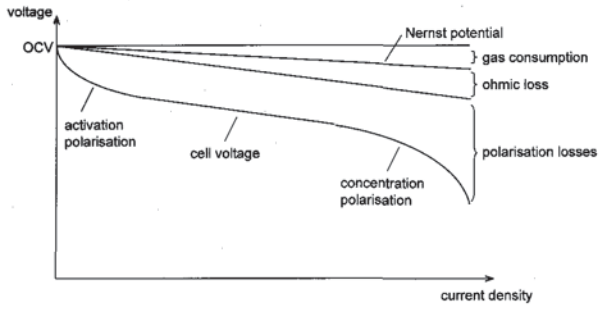

Figure 1.1: Schematic plot of voltage versus current density showing different types of polarization. Polarization losses dominate at various current densities. From [SK03].

Thus, it is paramount to start improving SOFCs rationally using first-principles modeling tools, which are validated against accurate, repeatable and reliable experiments. State-of-the-art experiments are usually compared against one-dimensional models [SK03]. The approach of this thesis is to study interesting new SOFC materials, to start from first principles and to study these materials in multiple dimensions. One of the goals is to link the first principle physics to directly measurable quantities.

In this thesis we will attempt to study from first principles polarization losses. In figure 1.1, we plot such polarization losses, which are voltage losses (or overpotentials) dependent on current density. The three dominant polarizations are:

1. Ohmic losses;

2. Concentration losses;

3. Activation losses.

Specifically this work will focus on the losses that scale proportionally to the area, which we call area specific resistance or area specific polarization. For example, we will show in

chapter 4 that the area specific resistance of a conventional doped ceria anode is directly related to the electrochemical properties on its electrochemically active interfaces.

1.1 Background

SOFCs have been under development since they were invented by Baur and Preis in 1937 [BP37]. In order to commercialize SOFCs it is necessary to reduce their cost of fabrication and operation. Mixed conducting materials may help decrease the internal electrical resistance of the SOFC by reducing the polarization resistance in both the anode and the cathode.

The electrolyte of an SOFC must consist of a good ionic conductor, which transports oxygen ions from the cathode to the anode. An often-used electrolyte material is yttria-stabilised zirconia (YSZ). On the other hand, the electrodes must be good electron conductors in order to facilitate the electrochemical reactions and to collect the current from the cell. A typical SOFC anode contains metallic nickel for this purpose. The anodic oxidation of the fuel, for example H_2, takes place in the vicinity of the so-called three-phase boundary (TPB), where gas phase, oxide (for example Yttrium Stabilized Zirconia YSZ) and metal (Ni) meet. This provides a region for all reactants to meet. In the case of SOFCs the reactants are oxygen ions, adsorbed species on the surface (H, OH, etc.) and electrons. In order to increase the total reaction rate, one can extend the length of the TPB zone by making a composite of Ni and YSZ called a $Ni|YSZ$-cermet, this design was patented by Spacil in 1970 [Spa70]. Another way to extend the total reacting area is to use a mixed ionic and electronic conductor, which in principle can support electrochemical reactions all over the surface as shown in figure 1.2. However mixed conductivity is not sufficient for a SOFC electrode, because the electrode must also possess a sufficiently high electrocatalytic

activity.

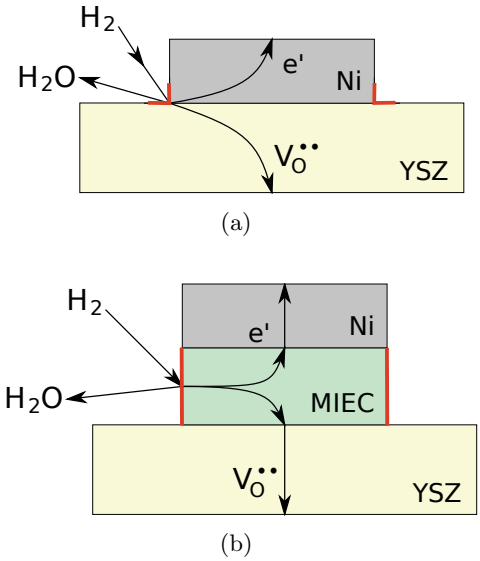

Figure 1.2: Difference between an anode based on an ionic conductor and metal assembly and a mixed conducting anode. The latter extends the area available for electrocatalytic reactions. (a) In an electrode where the electrode material is exclusively an electronic conductor, the reaction zone is restrained to the vicinity of the triple phase boundary (TPB). (b) In a mixed ionic-electronic conductor (MIEC) the electrode reactions can take place on the entire electrode surface.

In SOFCs it is also required that the electrode material is reasonably stable and that it does not change its volume as a result of reduction or oxidation. In addition, the thermal expansion coefficient of the electrode material must be close to the electrolyte material. Hence, lowering the operating temperature might be beneficial. With Ceria it is possible to use less pretreatment and lower water (steam) partial pressure in the fuel lines due to lower susceptibility to coke formation on ceria containing anodes. Also, ceria-based anodes are less sensitive to sulphur poisoning.

In order to understand the electrochemistry it is important to first have a grasp onthe crystallographical and electrical properties of Ceria. The next sections briefly describe ceria defect chemistry, while the rest of the thesis will describe the continuum level modeling of SOFC mixed conducting anodes in the linear regime, focusing mainly on ceria but also

showing that the tools developed here can be applied to cathodic mixed conductors.

1.1.1 Lattice Structure of Cerium Dioxide

Cerium with a $4f^2 5d^0 6s^2$ electron configuration can exhibit both the +3 and the +4 oxidation states, and there exist intermediate oxides whose composition is in the range Ce_2O_3-CeO_2. Thermodynamic data indicate that cerium metal is unstable in the presence of oxygen and that Ce_2O_3 and CeO_2 are easily formed, where the final stoichiometry is strongly dependent on temperature and oxygen pressure. The CeO_2 crystallizes in the fluorite structure which is named after the mineral form of calcium fluorite, CaF_2. It has a face-centered cubic unit cell (fcc) with space group $Fm3m$ and lattice length of $a = 5.411$ Å. In the structure each cerium cation is coordinated by eight oxygen anions at the corner of the cube. Each cation is tetrahedrally coordinated by four cations. The structure can be thought as a fcc array of cerium ions with oxygen occupying all the tetrahedral holes. This clearly shows that there are large vacant holes in the strucure, a significant feature when we consider the movement of ions through the defect structure.

Reduced ceria arises from the removal of O^{2-} anions from the CeO_2 lattice, which in turn generates a vacant site in the lattice. We can study this effect using the reaction

$$4Ce^{4+} + O^{2-} \rightarrow 4Ce^{4+} + 2e^- + O_O^x + \frac{1}{2}O_2 \rightarrow 2Ce^{4+} + 2Ce^{3+} + O_O^x + \frac{1}{2}O_2, \qquad (1.1)$$

where O_O^x is an empty site or anion vacant site (site deprived of an anion) originating from the removal of O^{2-} from the lattice, here represented as an oxygen tetrahedral site (Ce_4O). Electrostatic charge conservation is maintained by the reduction of two cerium cations from +4 to +3.

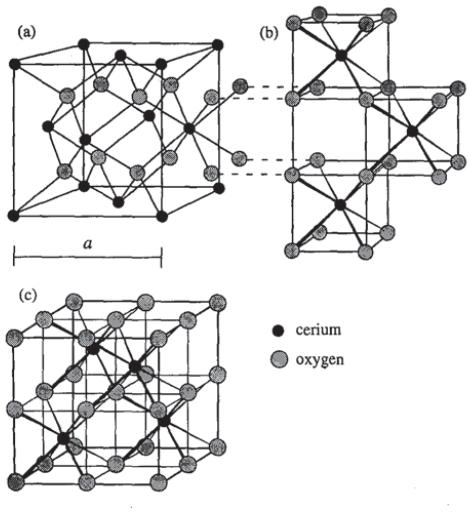

Figure 1.3: Axonometric view of the structure of CeO_2, which can be decomposed as a collection of cubic and cubic centered (with cerium in the middle) crystallographic oxygen elements. From Trovarelli [Tro01].

1.1.2 Chemistry of Defects in Doped Ceria

In this thesis we focus on acceptor-doped ceria[‡], in particular on Samarium Doped Ceria (SDC).

Defects in doped ceria can be created intrinsically, due to thermochemical conditions of the lattice ceria, or extrinsically, due to addition of dopant to the Ceria structure. We will not discuss the defect chemistry of pure Cerium oxides for which we refer to the monograph edited by Trovarelli [Tro01], but we will focus on doped Ceria.

Under reducing conditions, e.g., in H_2 and H_2O atmospheres, Ceria will exchange oxygen anions to the ambient atmosphere (or equivalently lattice oxygen ions are in thermodynamic equilibrium with ambient oxygen molecules). This exchange can also be understood as the creation of oxygen vacancies and a change in the cerium oxidation state from Ce^{4+} to Ce^{3+}.

[‡]During doping, impurity atoms are introduced to a mixed conductor. Impurity atoms are atoms of a different element than the atoms of the mixed conductor acting either as donors or acceptors of electrons. Electron donor doping makes the electron concentration increase (this will in turn decrease the resistivity) while acceptor impurity atoms will make the vacancy concentration increase, leading to a net increase of vacancy conductivity.

In Kröger-Vink notation [KV56] this equilibrium can be written as

$$O_O^x \rightleftharpoons \frac{1}{2}O_2 + V_O^{\bullet\bullet} + 2Ce'_{Ce}, \tag{1.2}$$

where O_O^x indicates an oxygen sitting in an oxygen lattice site, $V_O^{\bullet\bullet}$ is an oxygen-vacant site and Ce'_{Ce} is a Ce^{3+} ion residing on a Ce^{4+} site (Ce'_{Ce} can be denoted as e').

We consider the case where the impurity is samarium and we will suppose Sm_2O_3 is added into two CeO_2 lattice elements, subsequently producing vacant sites $V_O^{\bullet\bullet}$ given by the reaction

$$Sm_2O_3 + 2Ce_{Ce}^x + 4O_O^x \rightarrow 2Sm'_{Ce} + 3O_O^x + V_O^{\bullet\bullet} + 2CeO_2, \tag{1.3}$$

where Ce_{Ce}^x represents a Ce^{4+} ion residing on a Ce^{4+} site and Sm'_{Ce} is a Sm^{3+} ion residing on a Ce^{4+} site.

The concentrations of oxygen vacancies and electrons, indicated respectively with c_{ion} and c_{eon}, must satisfy the equilibrium condition derived from reaction (1.2)

$$K_r = \frac{c_{eon}c_{ion}^2 p_{O_2}^{1/2}}{[O_O^x]}, \tag{1.4}$$

where $[O_O^x]$ is the concentration of oxygen sites and K_r is given by an Arrhenius expression

$$K_r = K_r^0 \exp\left(\frac{\Delta S_r}{k_B}\right) exp\left(-\frac{\Delta H_r}{k_B T}\right), \tag{1.5}$$

where k_B is Boltzmann's constant, T the temperature in Kelvin, ΔS_r the reduction entropy, ΔH_r the reduction enthalpy.

We note that dopant addition as given by (1.3) will require neutrality in sample at equilibrium, thus the following will need to be satisfied:

$$B + c_{eon} = 2c_{ion}. \tag{1.6}$$

The equations (1.4) and (1.6) form a system of two equations with two unknowns c_{eon} and c_{ion}; the system has one unique real solution.

1.1.3 Transport Properties

Electrical conduction and other transport properties of oxides, such as oxygen and electron diffusion, are determined by the presence, concentration and mobility of lattice defects. The application of materials as electrolyte or electrocatalyst relies intimately on their conductive properties. At high temperature and low oxygen partial pressures, as they occur in SOFC anodes, ceria behaves mesoscopically as an n-type semiconductor.

In this range the dopant can be assumed as immobile while vacancies hop between neighboring anion-vacant sites as a result of a thermally activated process. Similarly, electronic conduction does not take place on electronic bands, as it would at very low temperatures in ionic crystals because of tunneling [Kad63] or an n-type semiconductor. Instead it is believed to occur via small Holstein polaron hopping [Hol59a] and [Hol59b] as Tuller and Nowick have argued experimentally [TN75].

The total conductivity σ_T of a solid is defined as the sum of the conductivities of its charge carriers

$$\sigma_T = \sum_m \sigma_m, \tag{1.7}$$

where m is a charge carrier in the solid, which could be either electronic (electrons e' or

holes $h^\bullet$) or atomic (anionic or cationic defect). In the case of SDC the mobile defects are only e' (charge $-e$) and vacancies $V_O^{\bullet\bullet}$ (charge $+2e$). Each conductivity σ_m, measured in Scm^{-1}[§] is given by the expression

$$\sigma_m = c_m z_m e u_m, \tag{1.8}$$

where c_m, $z_m e$ and u_m are respectively concentration, charge and mobility of species m. For SDC the total conductivity σ_T is given by

$$\sigma_T = [Ce'_{Ce}]eu_e + 2[V_O^{\bullet\bullet}]eu_{V_O^{\bullet\bullet}}. \tag{1.9}$$

1.1.3.1 Mobilities

We have seen in the previous section that the conductivities depend linearly on the mobilities as given by (1.8). It is useful then to write a few more words about them. Mobilities in ionic conductors follow an Arrhenius type of law because conduction is a thermally activated process. The mobility of oxygen vacancies u_{ion} is given by

$$u_{ion} = \frac{u_{ion}^0}{T} \exp\left(-\frac{\Delta H_{ion}}{k_B T}\right), \tag{1.10}$$

where u_{ion}^0 is a constant and ΔH_{ion} is the activation energy for ionic hopping [Tro01]. Similarly, at high temperature, polarons diffuse thanks to thermally activated hopping and their mobility is generally given by [BvD70]

[§] $1\mathrm{S} = \Omega^{-1}$ (one Siemens is the inverse of one Ohm).

$$u_{eon} = \frac{u^0_{eon}}{T^\alpha} \exp\left(-\frac{\Delta H_{eon}}{k_B T}\right), \tag{1.11}$$

where u^0_{eon} is a constant and ΔH_{eon} is the activation energy for polaronic hopping and here we choose adiabatic hopping, i.e., $\alpha = 1$.

1.1.3.2 Conductivities

As we have shown above, the conductivities are the product of charge per unit of volume and the mobility, leading to

$$\sigma_{eon} = 2eu_{ion}c_{ion}, \tag{1.12}$$

$$\sigma_{ion} = eu_{eon}c_{eon}. \tag{1.13}$$

If the sample is heavily doped and the oxygen partial pressure p_{O_2} is sufficiently low, then

$$c_{ion} = \frac{B}{2}, \tag{1.14}$$

$$c_{eon} = \sqrt{\frac{2K_r}{B}} p_{O_2}^{1/4}, \tag{1.15}$$

which gives a total conductivity $\sigma_T = \sigma_{ion} + \sigma_{eon}$

$$\sigma_T = \sigma_{ion} + \sigma^0_{eon} p_{O_2}^{-1/4}. \tag{1.16}$$

In the ionic regime of ceria (oxidizing conditions or high p_{O_2}) the total conductivity of SDC is independent of oxygen partial pressure. Under reducing conditions, the electronic conductivity depends on the oxygen partial pressure via the $-1/4$ power law. We further

notice that the dependence of σ^0_{eon} on the temperature is given by [Lai07]

$$\sigma^0_{eon} = \frac{\sigma^{00}_{eon}}{T} \exp\left(-\frac{\Delta H_{eon} + \frac{1}{2}\Delta H_r}{k_B T}\right), \tag{1.17}$$

where σ^{00}_{eon} is a constant and the activation energy is $\Delta H_{eon} + \frac{1}{2}\Delta H_r$.

1.2 Measurable Quantities and General Modeling Issues of Mixed Conductors

1.2.1 Impedance Spectroscopy

Electrochemical Impedance Spectroscopy (EIS or IS) is a powerful method for characterizing the properties of electrochemically active materials and their interfaces. IS can be used to investigate the fundamental microscopic processes that are activated by electric forces imposed on ionic or mixed conducting materials. IS is a very popular tool in electrochemistry of SOFC because it involves relatively simple electrical measurements that can be automated and whose results can often be correlated to complex material properties (electro-catalytic reaction rates, diffusion constants, defect concentrations, dielectric properties, etc.). IS can also predict certain aspects of SOFC performance, notably the polarization resistance.

The IS of an electrochemical system is based on the perturbation of a steady state condition of that system by applying a single frequency voltage or current to the interface and measuring the phase shift and amplitude of the resulting current (see figure 1.4). The IS measurement is usually gathered using impedance analyzers which can measure the IS as a function of frequency in a range approximately from 1 mHz to 1 MHz. IS usually explores a wide frequency domain, leading ultimately to knowledge of the linear macroscopic

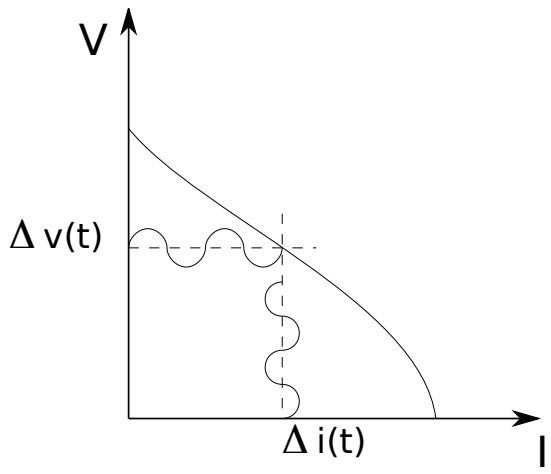

Figure 1.4: Schematic depiction of an impedance experiment. A sinusoidal voltage perturbation $\Delta v(t)$ is applied to the system and the current response $\Delta i(t)$ is recorded, the ratio of the two give the absolute value of the impedance and the phase difference between gives the its argument in complex space.

response of the system under study in frequency space. If the underlying physical-chemical phenomena of the system studied are characterized by sufficiently spaced time-scales, and some of those constants are known *a priori*, then each peak of the frequency response (its frequency location and intensity) can be, in principle, linked quantitatively to a specific physical phenomena.

Let us stress again that IS consists of automated measurement of Z as a function of ω over a wide frequency range. It is from the structure of $Z(\omega)$ that one can deconvolve the physical and chemical behavior of the system under study, this makes underlying models key. For non-linear systems (the vast majority of SOFCs are non-linear), IS measurements are meaningful only for signals of magnitude such that the response of the system is linear (or additive). One method to evaluate linearity is to check whether a monochromatic input generates non monochromatic output.

There are various techniques that are commonly used to analyze impedance data. For example, the Kramers-Kronig relations (basically formulas derived from Hilbert transform)

allow one to check the validity of the data obtained [AOGR92] and [Bou95]. Also the experimental data can be fitted via some non-linear technique (typically Complex Non-linear Least Square is used) against plausible one-dimensional electric circuits which describe a likely set of electrochemical phenomena taking place in the system under study.

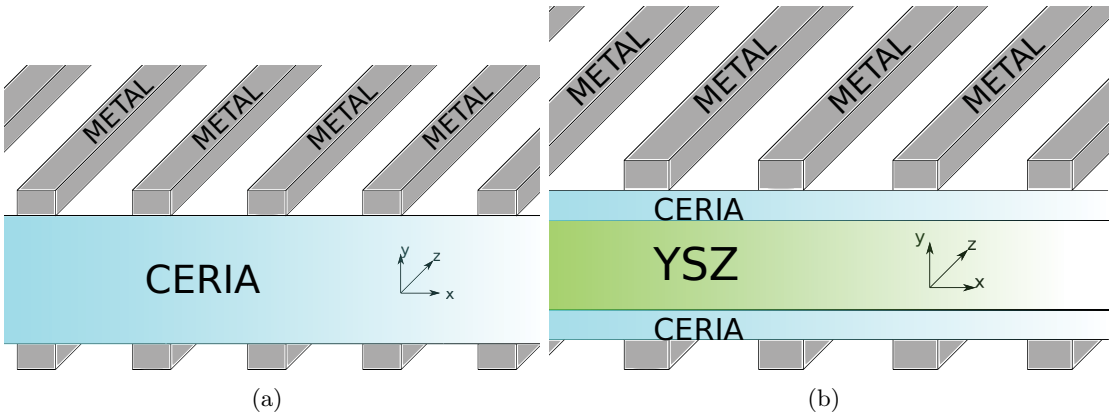

Figure 1.5: Schematics of the systems studied numerically. (a) Ceria slab sandwiched between two patterned ceria metal current collectors. (b) Ionic conductor slab sandwiched between two ceria thin films patterned with stripes of metal which serves as current collector. The function of the ionic conduction is to inhibit the electrons to migrate from the top to the bottom portion of the assembly.

The disadvantages of IS are mainly associated with ambiguities in its interpretation. An important complication of analyses based on an equivalent circuit is that ideal circuits (capacitance, resistance and inductance) represent lumped constant properties and may be inadequate to describe the electrical response of a multidimensional system. This is because electrochemical phenomena are distributed in three-dimensional space and they feature nonuniform properties. The utilization of nonelementary impedance elements aids the process of fitting observed impedance data for distributed properties. For example, one could use nonideal capacitance with the following Fourier transform $C_\alpha = \dfrac{1}{i\omega^\alpha C_\alpha}$ (an ideal capacitance has $\alpha = 1$). However, such impedance elements may only have a phenomenological nature (we shall reserve this analysis for chapter 3). Another problem with equivalent

circuit analysis is the potential nonuniqueness of the model used to fit the experimental data. For instance an equivalent circuit involving three or more circuit elements can often be rearranged in many ways to give the same equivalent impedance [BM05]. In order to solve these questions, it is beneficial to study the same electrochemical system under several different experimental settings, for example varying geometry, temperature or chemical conditions. However such studies could prove inconclusive if the underlying model is not mechanistic [FKJM08].

1.3 Structure of the Thesis

We will initially develop the mathematical framework for the study of the two systems depicted in figure 1.5. We will then specialize the framework in the one-dimensional case. This will help lay down some of the qualitative properties for the mathematical study of linear impedance. Incidentally, we will also derive one "new" analytical expression for the study of quasi-one-dimensional thin films. It is important to stress that one-dimensional formulations are usually utilized to interpret experimental data.

Then we will focus on extending this work to two dimensions, first studying numerically the system in figure 1.5(a) under small bias conditions, corresponding to an impedance excitation at zero frequency. We will then extend the model to study the full impedance range for both figure 1.5(a) and figure 1.5(b), where the latter configuration is close to the fuel cell setting.

Chapter 2

Mathematical Modeling

2.1 Bulk Material Modeling: The Drift-Diffusion Equations

In order to model the electrochemical phenomena in SOFCs, we have to be able to solve ordinary and partial differential equations which, among other things, will let us determine electric potentials and currents. The first step is then to determine which equations will satisfy mass and charge transport. In ionic materials, under linear conditions (see Callen and Welton [CW51] or Kubo [Kub66]) diffusion and migration result from a gradient in electrochemical potential $\tilde{\mu}$ [DGM84], [Pri61]. Consider a "small" element of ionic material connecting two points $\mathbf{x}_1$ and $\mathbf{x}_2$ sufficiently close, where for a certain species m, $\tilde{\mu}_m(\mathbf{x}_1) \neq \tilde{\mu}_m(\mathbf{x}_2)$. This difference of $\tilde{\mu}_m$ can arise because there is a difference of concentration (or chemical activity) of species m or because there is an electric field. In general $\mathbf{j}_m^P$, the particle flux of species m, is proportional to the gradient of electrochemical potential

$$\mathbf{j}_m^P \propto \nabla \tilde{\mu}_m, \tag{2.1}$$

where the constant of proportionality is $\frac{c_m D_m}{k_b T}$, leading to

$$\mathbf{j}_m^P = -c_m D_m \nabla \frac{\tilde{\mu}_m}{k_b T}, \tag{2.2}$$

where c_m is the concentration of species m, D_m is its diffusivity and where the electrochemical potential is given by

$$\tilde{\mu}_m = \tilde{\mu}_m^0 + k_b T \log a_m\left(c_m\right) + z_m e \phi. \tag{2.3}$$

If we take $a_m = \frac{c_m}{c_m^0}$ (this corresponds to the condition where species m are non-interacting or sufficiently "dilute"), we recover the so-called Nernst-Planck equation, where the flux of particles is given by

$$\mathbf{j}_m^P = -D_m \nabla c_m - \frac{z_m e}{k_B T} D_m c_m \nabla \phi. \tag{2.4}$$

If the particles are charged, i.e., $z_m \neq 0$, then the current density $\mathbf{j}$ is proportional to the flux $\mathbf{j}_m$ of species m:

$$\begin{aligned} \mathbf{j} &= \textstyle\sum_m z_m e \mathbf{j}_m^P \\ &= \underbrace{\frac{e^2}{k_B T}\left(\sum_m z_m^2 D_m c_m\right)\nabla\phi}_{\text{DRIFT}} + \underbrace{e\left(\sum_m z_m D_m \nabla c_m\right)}_{\text{DIFFUSION}}. \end{aligned} \tag{2.5}$$

We further note that u_m, the mobility of species m, is linked to the diffusion coefficient D_m by the Einstein-Smochulowski equation (for a derivation see Van Kampen's textbook [VK07]):

$$u_m = \frac{|z_m| e D_m}{k_B T}. \tag{2.6}$$

In order to be consistent with the principles of electromagnetism, the continuity equations have to be used in conjunction with Gauss's law, which in this case is equivalent to the Poisson equation for the potential

$$\nabla \cdot (\varepsilon \nabla \phi) = -\rho, \tag{2.7}$$

where ρ is the local charge per unit volume of the medium and ε is the local permittivity of the medium. Hence, in order to find the electrical properties of the MIEC, one needs to solve Poisson's equation for the electric field, (2.7), and the conservation equations for each of the species present in the sample (2.2). We can summarize the equations to solve as follows:

$$\begin{aligned} \nabla \cdot (\varepsilon \nabla \phi) &= -\rho, && \text{(2.8a)} \\ \partial_t c_{eon} + \nabla \cdot \mathbf{j}^P_{eon} &= \dot{\Omega}_{eon}, && \text{(2.8b)} \\ \partial_t c_{ion} + \nabla \cdot \mathbf{j}^P_{ion} &= \dot{\Omega}_{ion}, && \text{(2.8c)} \end{aligned}$$

where c_{eon} and c_{ion} are the electron and vacancy density (number of electrons per unit volume) respectively and where $\mathbf{j}^P_{eon}$ and $\mathbf{j}^P_{ion}$ indicate the fluxes of electrons and vacancies respectively. In expression (2.8c) we also include the net volumetric rate of generation of electrons and vacancies, $\dot{\Omega}_{eon}$ and $\dot{\Omega}_{ion}$ respectively.

We set here that electrons are dilute and follow a Boltzmann distribution, while vacancies are present in much greater number. It follows that site exclusion and interaction effects have to be taken into account. For lack of other sources Hendriks' empirical approach can

be used [Hen01] and we will express the electrochemical potentials in this way:

$$\tilde{\mu}_{eon} = \tilde{\mu}^0_{eon} + k_b T \log\left(\frac{c_{eon}}{c^0_{eon}}\right) - e\phi, \tag{2.9a}$$

$$\tilde{\mu}_{ion} = \tilde{\mu}^0_{ion} + k_b T \log\left(\frac{c_{ion}}{c^{\mathrm{MAX}}_{ion} - c_{ion}}\right) + 2e\phi. \tag{2.9b}$$

2.2 Nondimensional Parameters and Equations

It is useful to nondimensionalize equations (2.8) and derive as many fundamental parameters as possible. The idea is to rescale all the unknowns (concentrations and electric potential) such that they are equal to unity in the bulk. First we define

$$U_T = \frac{k_b T}{e}, \tag{2.10a}$$

$$\lambda_D = \sqrt{\frac{\varepsilon U_T}{eB}}, \tag{2.10b}$$

$$\lambda^2 = \left(\frac{l_c}{\lambda_D}\right)^2, \tag{2.10c}$$

$$\tau_n = \frac{l_c^2}{D_{eon}}, \tag{2.10d}$$

$$\tau_p = \frac{l_c^2}{D_{ion}}, \tag{2.10e}$$

$$\tau = \min\left(\tau_n, \tau_p\right), \tag{2.10f}$$

where U_T is a voltage, λ_D is the Debye length, l_c is the characteristic length (in our case $l_c \approx 10\mu m$), τ_n and τ_p are respectively the polaron and vacancy characteristic diffusion times. We further define the follfowing three quantities describing non dimensional bulk

concentrations of conducting species:

$$\bar{n} = \frac{c_{eon}^{\text{BULK}}}{B}, \tag{2.11a}$$

$$\bar{p} = \frac{c_{ion}^{\text{BULK}}}{B}, \tag{2.11b}$$

$$\alpha = \frac{c_{ion}^{\text{MAX}}}{c_{ion}^{\text{BULK}}}, \tag{2.11c}$$

where $\bar{n}$ is the ratio of bulk electrons to dopant, $\bar{p}$ is the ratio of bulk ions to dopant (under the assumptions above always equal to 2) and α is a phenomenological constant.

Since our goal is to rewrite (2.8) in dimensionless form, we first need to transform the coordinates using $(t, \mathbf{x}) \mapsto \left(\tilde{t}, \tilde{\mathbf{x}}\right)$ such that

$$\tilde{t} = \frac{t}{\tau}, \tag{2.12a}$$

$$\tilde{\mathbf{x}} = \frac{1}{l_c}\mathbf{x}. \tag{2.12b}$$

Then we need to transform the variables $(\phi, c_{eon}, c_{ion}) \mapsto \left(\tilde{\phi}, n, p\right)$ (n stands for negative and p for positive) according to

$$\tilde{\phi} = \frac{\phi}{U_T}, \tag{2.13a}$$

$$n = \frac{c_{eon}}{\bar{n}B}, \tag{2.13b}$$

$$p = \frac{c_{ion}}{\bar{p}B}. \tag{2.13c}$$

The definition above will allows us to rewrite (2.8) as

$$\triangle_{\tilde{x}}\tilde{\phi} = \lambda^2 \left(1 + \bar{n}n - 2\bar{p}p\right), \tag{2.14a}$$

$$\frac{\tau_n}{\tau}\partial_{\tilde{t}} n + \nabla_{\tilde{x}} \cdot \left(n\nabla_{\tilde{x}}\tilde{\phi} - \nabla_{\tilde{x}} n\right) = 0, \tag{2.14b}$$

$$\frac{\tau_p}{\tau}\partial_{\tilde{t}} p - \nabla_{\tilde{x}} \cdot \left(2p\nabla_{\tilde{x}}\tilde{\phi} + \frac{\alpha}{\alpha - p}\nabla_{\tilde{x}} p\right) = 0. \tag{2.14c}$$

The equations (2.14) with $\alpha \to \infty$ constitute the starting point for this thesis. Hence, it is beneficial to describe their use, their limitations and their most striking qualitative properties.

The range of applicability of the equations above is quite vast and in particular they can be used to model the bulk behavior of mixed conductors that are commonly employed in solid oxide fuel cells:

- The equations (2.14) were derived in the linear regime [CW51], where fluxes are sufficiently small, and their range of validity is then comparable to the conditions usually employed in electrochemisty of ionic materials [Mai04];

- The equations (2.14) are based on the continuum assumption which may break down at the atomic level. However, works by Armstrong et al. [AH97], Corry et al. [CKC00] and the review of Vlachy [Vla99] strongly suggest that Monte-Carlo simulations and continuum descriptions converge to the same macroscopic results for sufficiently big samples when the size of the system is at least three times the Debye length λ_D;

- We have assumed that the dielectric constant of the medium is uniform, however this may not be the case near interfaces where orientation effects may play a role [HP07a];

- We have assumed that the chemical potential in the medium is uniquely defined by a

function that supposes dilution or at best that accounts empirically for site exclusion. Near interfaces, where surface states may be preferable, the chemical potential may change significantly, hereby changing the activity.

We further note that (2.14a) depends on the very significant parameter λ^2, which is the square of the ratio of the characteristic length of the sample l_c and Debye length λ_D. In the case of Samarium Doped Ceria with 15% doping the Debye length is of the order of $1\mathring{A}$*; if we take the characteristic length of variation to be of the order of $10\mu m$ we will get that $\lambda \approx 10^5$. We can then follow a heuristic argument: suppose we take a mixed conducting material sample with high λ, suppose that we bias the sample with a finite bias, and suppose also that the deviation from neutrality in the bulk of the material is finite; then the Laplacian of the potential is very high, which results in a strong electric field, leading to a contradiction. Hence, in order to have "small" second derivatives of the electric potential in most of the bulk we will require that the total charge is very close to zero or $1 + \bar{n} - 2\bar{p}p = 0$. This results in the electroneutrality condition that has to be satisfied in the bulk of the material and will allow us to conveniently discard (2.14a), leaving only two time dependent partial differential equations. It is necessary to note that deviations from the electroneutrality will be allowed for small sample sizes ($l_c \approx \lambda_D$) and in the vicinity of interfaces, where charged layers may occur (in the ionics community they are commonly called double layers).

Interfaces bring about another set of interesting questions. As it is well known, the solution of a partial differential equation, or for that matter of a system of PDEs, is strongly dependent on the boundary conditions utilized. In general reactions will occur at the SOFC surfaces exposed to the gas stream (the interface for example between the MIEC and the

*We take $\varepsilon = \varepsilon_r \varepsilon_0$ where $\varepsilon_0 = 8.85 \times 10^{-12}$, $\varepsilon_r = 3$ and $B = 3.7 \times 10^{27} \frac{\#particles}{m^3}$ which gives $\lambda_D = \sqrt{\frac{\varepsilon_r \varepsilon_0}{eB}} \approx 2 \times 10^{-10} m$.

GAS, in red in figure 1.2(b)) leading to net electric current, and, for our purposes, boundary conditions for the PDEs in (2.14). Similarly interfaces between the MIEC and the metal current collector, between the MIEC and an ionic conductors and between different grains of the MIEC will need to be evaluated using appropriate boundary conditions.

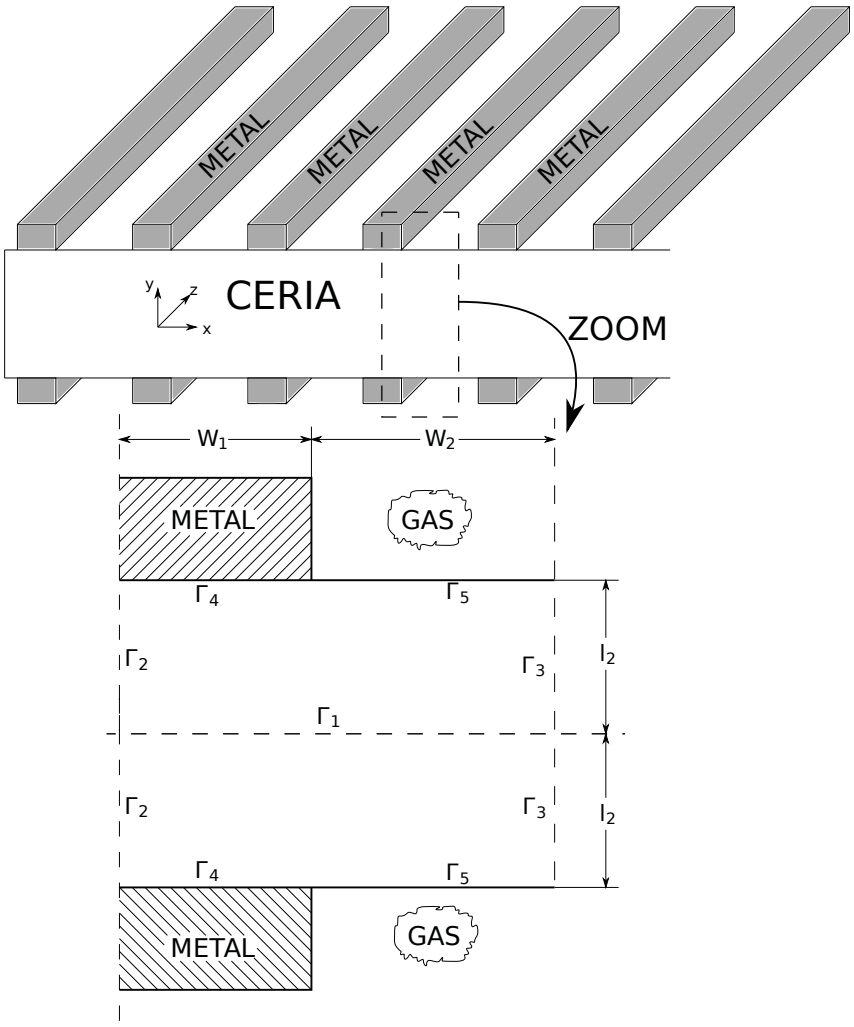

Figure 2.1: (top): A symmetric cell with patterned Pt stripes on both sides of dense ceria placed in a uniform gas environment. (bottom): Schematic depiction of the boundaries. Γ_1, Γ_2, and Γ_3 are symmetry lines, while Γ_4 is the metal | ceria interface, and Γ_5 is the gas | ceria interface. The width of the metal and the of the ceria directly exposed to the gas phase are respectively $2W_1$ and $2W_2$. The thickness of the Ceria sample is $2l_2$.

2.3 Bulk Equilibrium Conditions

We indicate the equilibrium quantities, such as electron and oxygen vacancy concentration, with the superscript (0). In order to determine equilibrium concentrations of charge carriers, we consider the following gas phase and bulk defect reactions:

$$\begin{aligned} H_2(\text{gas}) + O_2(\text{gas}) &\rightleftharpoons H_2O(\text{gas}), \\ O_O^x &\rightleftharpoons V_O^{\bullet\bullet} + \tfrac{1}{2}O_2(\text{gas}) + 2e', \end{aligned} \tag{2.15}$$

where the Kroger-Vink notation is used. We can also write the following equilibrium constants:

$$K_g = \frac{\tilde{p}^2_{H_2O}}{\tilde{p}^2_{H_2}\tilde{p}_{O_2}}, \tag{2.16a}$$

$$K_r = \left(\frac{c^{(0)}_{eon}}{B}\right)^2 \frac{c^{(0)}_{ion}}{B}\tilde{p}^{1/2}_{O_2}, \tag{2.16b}$$

where $\tilde{p}_k = \dfrac{p_k}{1\text{atm}}$ and p_k is the partial pressure of species k. If we couple (2.16) (equilibrium of reactions in (2.15)) with the electroneutrality conditions, i.e., $1 + \dfrac{c^{(0)}_{eon}}{B} - 2\dfrac{c^{(0)}_{ion}}{B} = 0$, we will be able to deduce the equilibrium concentrations of vacancies $c^{(0)}_{ion}$ and electrons $c^{(0)}_{eon}$ in the dilute limit at a given temperature and partial pressures. As we have shown in the section 1.1.3.2 we can assume that the equilibrium concentrations of electrons and vacancies

is given by

$$c_{ion} = \frac{B}{2} \tag{2.17}$$

$$c_{eon} = \sqrt{\frac{2K_r}{B}} p_{O_2}^{1/4}. \tag{2.18}$$

For SDC-15 we have that the concentration of samaria atoms in the lattice $[Sm'_{Ce}] = 0.15$, [KV56], the n_c coordination number is 4 [ASS$^+$06] and the cell length is $5.43 \times 10^{-10} m$ [ZWTL01], so its volume V_0 is given by $V_0 = l_{cell}^3$. This implies that the concentration of background negatively charged ions in the bulk can be expressed as $B = n_c \frac{[Sm'_{Ce}]}{V_0} = 3.74759 \times 10^{27} \ \frac{\#\text{particles}}{m^3}$.

2.4 The Model for the Off-Equilibrium Bulk Behavior

We suppose a time-independent small bias off-equilibrium perturbation is performed in our system. Experimentally, this is achieved by subjecting the electrochemical cell to a small DC voltage relative to the open circuit voltage. Alternatively, we can obtain the same information by making an AC impedance measure at open circuit and taking the resistance at the the low frequency limit where the frequency approaches zero. We indicate these small perturbations with the subscript (1) and the basic conditions with the superscript (0). These working conditions can be summarized as follows:

- $n = n^{(0)} + n^{(1)}$ with $\nabla n^{(0)} = 0$ and $1 = |n^{(0)}| \gg |n^{(1)}|$;
- $p = p^{(0)} + p^{(1)}$ with $\nabla n^{(0)} = 0$ and $1 = |p^{(0)}| \gg |p^{(1)}|$;
- $\tilde{\phi} = \tilde{\phi}^{(0)} + \tilde{\phi}^{(1)}$ with $\nabla \tilde{\phi}^{(0)} = 0$ and $|\tilde{\phi}^{(0)}| \gg |\tilde{\phi}^{(1)}|$;

Table 2.1: Temperature range and material constants for the simulations.

T	500^oC	550^oC	600^oC	650^oC
K_g	5.059E+27	4.814E+25	7.757E+23	1.944E+22
K_r	5.008E−22	2.263E−20	6.610E−19	1.340E−17
u_{eon} $\left[\frac{m^2}{V^2 s}\right]$	4.762E − 8	6.257E−8	6.873E−8	8.123E−8
u_{ion} $\left[\frac{m^2}{V^2 s}\right]$	1.166E−9	2.070E−9	3.359E−9	4.936E−9

Incidentally we note that the we chose the 0th order solution such that it corresponds to equilibrium conditions. The ensuing equations are then greatly simplified. We could imagine starting from off equilibrium conditions but that would make the algebra much more complex. If we enforce electroneutrality we will have that at first order

$$\bar{n}n^{(1)} = 2\bar{p}p^{(1)} \tag{2.19}$$

Substituting the above definitions and properties above into (2.14) and keeping only first order terms yields the following system of linear PDEs:

$$\triangle n^{(1)} = 0, \tag{2.20a}$$

$$\triangle \tilde{\phi}^{(1)} = 0. \tag{2.20b}$$

The (2.20) will be the starting point for the subsequent steady-state analysis.

2.4.1 Boundary Conditions for the Steady State Case

Realistic boundary conditions are complex due to the formation of charge double layers [Sze81], [RW00]. Work by Fleig et al. [Fle05], [FMM07] suggests that such electrification

effects are relevant for SOFC mixed conducting cathodes. Because we suppose that the sample is sufficiently thick, we do not consider charge double layer in our system (this issue will be addressed in Chapter 6). Furthermore, we do not consider surface diffusion since the the need to specify the surface roughness may lead to over-fitting of the data and since the experiments we use to check the validity of our results did not feature a thorough analysis of the surface.

As shown in figure 2.1 (bottom), there are five boundaries in our electrochemical system each corresponding to significantly different boundary conditions. We start with the simplest boundary conditions: it follows from symmetry that $\partial_x \tilde{\mu}_{eon}^{(1)} = 0$, $\partial_x \tilde{\mu}_{ion}^{(1)} = 0$ on Γ_2 and Γ_3. Since the metal is ion blocking we will have $\partial_y \tilde{\mu}_{ion}^{(1)} = 0$ on Γ_4. By assuming that the response of the metal to any perturbation is fast compared to the oxide, we can suppose $\phi^{(1)}$ is uniform on Γ_4. Because of linearity, we can choose $\phi^{(1)} = k_b T/e$ on Γ_4 (so that $\tilde{\phi}^{(1)} = 1$) and $\phi^{(1)} = 0$ on Γ_1.

The remaining boundary, Γ_5, is complex due to the gas-solid surface reaction electrochemistry. Specifically, the fuel cell anode condition under which our computation is performed requires us to consider the interaction of oxygen vacancies and electrons SDC and gas-phase hydrogen, oxygen and water vapor. A complete treatment of the surface require a detailed understanding of the electrochemical reaction pathway and kinetics parameters of various reactions that occur in series and/or parallel. However, there is little experimental data in literature regarding the surface reactions for SDC (or for any other composition of doped ceria). In the case of ceria, AC impedance spectroscopy is unable to separate multiple processes that occur on the electrode | electrolyte interface due to the overwhelming "chemical" capacitance that results from redox of cerium cation between +4 and +3 oxidation states.

In this work, we treat the surface reaction pathway as a single step (see appendix C for more details). Specifically, we assume that the surface chemistry can be described by

$$H_2(\text{gas}) \rightleftharpoons H_2O(\text{gas}) + V_O^{\bullet\bullet} + 2e'. \tag{2.21}$$

Furthermore, we assume that the rate of reaction, specifically, the rate of injection of vacancies at Γ_5 satisfy

$$\begin{aligned} \mathbf{j}_{ion} \cdot \mathbf{e}_y &= \tfrac{1}{2}\mathbf{j}_{eon} \cdot \mathbf{e}_y, \\ -\mathbf{j}_{ion} \cdot \mathbf{e}_y &= k_f \tilde{p}_{H_2} - k_r \tilde{p}_{H_2O} c_{ion} c_{eon}^2. \end{aligned} \tag{2.22}$$

where $\mathbf{e}_y$ is the unit vector that is perpendicular to Γ_5, k_f and k_r are the forward and reverse reaction rate constants, respectively. At equilibrium, the net rate of injection of both oxygen vacancies and electrons are zero, so k_f and k_r can be related to the equilibrium concentrations of the reactants and products

$$k_r = \frac{2k_f \tilde{p}_{H_2}}{\left(c_{eon}^{(0)} + B\right)\left(c_{eon}^{(0)}\right)^2 \tilde{p}_{H_2O}}. \tag{2.23}$$

Using the same perturbative approach of section 2.4, we compute the perturbation in the boundary condition upon applying a small bias perturbation. At first order we derive a Chang-Jaffé boundary condition [CJ52] on Γ_5

$$\begin{aligned} -\dot{\omega}_{eon}^{(1)} &= -\dot{\omega}_{eon} = \tfrac{1}{2} k_r \tilde{p}_{H_2O} \left(c_{eon}^{(0)} + c_{eon}^{(1)} + B\right)\left(c_{eon}^{(0)} + c_{eon}^{(1)}\right)^2 + \\ &- k_r \tilde{p}_{H_2O} \left(c_{eon}^{(0)} + B\right)\left(c_{eon}^{(0)}\right)^2 \\ &= \frac{1}{2} k_r \tilde{p}_{H_2O} c_{eon}^{(0)} \left(2B + 3c_{eon}^{(0)}\right) c_{eon}^{(1)} \\ &= \frac{1}{2} k_r \tilde{p}_{H_2O} \left(c_{eon}^{(0)}\right)^2 \left(2B + 3c_{eon}^{(0)}\right) n^{(1)}. \end{aligned} \tag{2.24}$$

We are now set to Γ_5; we first remark that at equilibrium:

$$\frac{1}{2}k_r\tilde{p}_{H_2O}\left(c_{eon}^{(0)}+B\right)\left(c_{eon}^{(0)}\right)^2-k_f\tilde{p}_{H_2}=0\Leftrightarrow\tilde{p}_{H_2O}=\frac{2K_r(T)}{\left(c_{eon}^{(0)}+B\right)\left(c_{eon}^{(0)}\right)^2}\tilde{p}_{H_2}, \tag{2.25}$$

where $k_f=k_f(T)$, $k_r=k_r(T)$ and $K_r(T)=\frac{k_f}{k_r}$;

We can finally rewrite (2.24) using (2.16a) as:

$$\mathbf{j}_{ion}^{(1)}\cdot\mathbf{e}_y \quad = \quad 2k_f\left(1+\frac{c_{eon}^{(0)}}{4c_{ion}^{(0)}}\right)\tilde{p}_{H_2}n^{(1)}. \tag{2.26}$$

We go a little further and suppose $k_f=2\dfrac{D_{ion}}{l_c}\tilde{k}_f$ $\tilde{k}_f=\tilde{k}_f^0\tilde{p}_{O_2}^{\beta}\times\dfrac{m^3}{\#\text{particles}}$, where we choose $\beta=-1/4$ to give[†]:

$$-\dot{\omega}_{eon}^{(1)}=2\frac{D_{ion}}{l_c}\tilde{k}_f^0\tilde{p}_{O_2}^{1/4}\left(1+\frac{c_{eon}^{(0)}}{4c_{ion}^{(0)}}\right)\tilde{p}_{H_2}n^{(1)}. \tag{2.27}$$

It is important to note that the choice of β is based on the oxygen partial pressure dependence of the rate limiting step(s) in the surface reaction. Since identifying the rate-limiting step in the surface reaction is beyond the scope of this work (as we described the surface reaction with a global reaction), we selected the β value so that the p_{O_2} dependence matches the experimental results [LH05] that are used for data analysis.

[†]The units of the k_fs are

$$[k_f]=\frac{\#\text{particles}}{s\times m^2},$$
$$\left[\tilde{k}_f\right]=\left[\frac{l_c}{D_{ion}}k_f\right]=\frac{\#\text{particles}}{m^3},$$
$$\left[\tilde{k}_f^0\right]=\left[\tilde{k}_f\right]=\frac{\#\text{particles}}{m^3},$$

let us look at order of magnitude of k_f: $\tilde{p}_{O_2}=10^{-24}$, $l_c=10^{-5}m$, $D_{ion}=10^{-10}m^2/s$ and $\tilde{k}_f^0\approx10^{32}$, so $k_f\approx10^{32}\times\frac{10^{-10}}{10^{-5}}\times10^{-6}$=$10^{21}\,\frac{\#\text{particles}}{m^2}\approx10^{-3}\,\frac{mol}{m^2}\approx10^{-7}\,\frac{mol}{cm^2}$.

2.4.2 Formalization of the Model

It is useful to recast the problem under study in a mathematical form that shows the smallest number of parameters in the equations and boundary conditions. In fact, one can deduce from (2.20) and the boundary conditions discussed in the previous section that

$$\triangle\tilde{\phi}^{(1)} = 0, \tag{2.28a}$$

$$\triangle n^{(1)} = 0, \tag{2.28b}$$

where $n^{(1)} = c_{eon}^{(1)}/c_{eon}^{(0)}$ and $\tilde{\phi}^{(1)} = \phi^{(1)}/U_T$ and that

$$\begin{cases} \tilde{\phi}^{(1)} = 0 & \& \quad n^{(1)} = 0 & \text{on} \quad \Gamma_1 \\ \partial_x\tilde{\phi}^{(1)} = 0 & \& \quad \partial_x n^{(1)} = 0 & \text{on} \quad \Gamma_2 \quad \& \quad \Gamma_3 \\ \tilde{\phi}^{(1)} = U_T & \& \quad \partial_y n^{(1)} = -4\frac{c_{ion}^{(0)}}{c_{eon}^{(0)}}\partial_y\tilde{\phi}^{(1)} & \text{on} \quad \Gamma_4 \\ \partial_y\tilde{\phi}^{(1)} = A_\phi n^{(1)} & \& \quad \partial_y n^{(1)} = A_n n^{(1)} & \text{on} \quad \Gamma_5 \end{cases}, \tag{2.29}$$

where $A_\phi = -\frac{1}{2}\frac{k_f\tilde{p}_{H_2}}{D_{ion}c_{ion}^{(0)}}\left(1 - \frac{D_{ion}}{D_{eon}}\right)$ and $A_n = -\frac{1}{2}\frac{k_f\tilde{p}_{H_2}}{D_{ion}c_{ion}^{(0)}}\left(1 + 4\frac{D_{ion}c_{ion}^{(0)}}{D_{eon}c_{eon}^{(0)}}\right)$. We further define $\tilde{k}_f^0 = \frac{\tilde{k}_f}{\tilde{p}_{O_2}^\beta}$[‡§]

If one defines $\mathbf{x} = l_c\tilde{\mathbf{x}}$ $(l_c = 10\mu m)$, $\tilde{A}_\phi = -\tilde{k}_f\frac{\tilde{p}_{H_2}}{c_{ion}^{(0)}}\left(1 - \frac{D_{ion}}{D_{eon}}\right)$ and $\tilde{A}_n = -\tilde{k}_f\frac{\tilde{p}_{H_2}}{c_{ion}^{(0)}}\left(1 + 4\frac{D_{ion}c_{ion}^{(0)}}{D_{eon}c_{eon}^{(0)}}\right)$

[‡]Oxygen ions cannot penetrate the metal giving that

$$\mathbf{e}_y \cdot \nabla\tilde{\mu}_{ion}^{(1)} = 0 \Leftrightarrow \partial_y\left(k_bT\frac{c_{ion}^{(1)}}{c_{ion}^{(0)}} + 2e\phi^{(1)}\right) = 0 \Leftrightarrow \partial_y\left(\frac{1}{2}\frac{c_{eon}^{(0)}}{c_{ion}^{(0)}}\frac{c_{eon}^{(1)}}{c_{eon}^{(0)}} + 2\tilde{\phi}^{(1)}\right) = 0$$

the latter gives

$$\partial_y n^{(1)} = -4\frac{c_{ion}^{(0)}}{c_{eon}^{(0)}}\partial_y\tilde{\phi}^{(1)}$$

[§]The chemical condition at the Gas|Ceria interface requires that the balance of fluxes at the interface

$$\begin{cases} \mathbf{j}_{eon}\cdot\mathbf{e}_y = -D_{eon}\partial_y c_{eon}^{(1)} + D_{eon}c_{eon}^{(0)}\partial_y\tilde{\phi}^{(1)} = -\dot{\omega}_{eon} \\ \mathbf{j}_{ion}\cdot\mathbf{e}_y = -D_{ion}\partial_y c_{ion}^{(1)} - 2D_{ion}c_{ion}^{(0)}\partial_y\tilde{\phi}^{(1)} = -\dot{\omega}_{ion} \end{cases} \Leftrightarrow \begin{cases} \partial_y c_{eon}^{(1)} - c_{eon}^{(0)}\partial_y\tilde{\phi}^{(1)} = \frac{\dot{\omega}_{eon}^{(1)}}{D_{eon}} \\ \partial_y c_{ion}^{(1)} + 2c_{ion}^{(0)}\partial_y\tilde{\phi}^{(1)} = \frac{\dot{\omega}_{eon}^{(1)}}{2D_{ion}} \end{cases}$$

then (2.20) and the boundary conditions of the previous section can be summarized as follows:

$$\begin{aligned} \triangle_{\tilde{x}} \tilde{\phi}^{(1)} &= 0, \\ \triangle_{\tilde{x}} n^{(1)} &= 0, \end{aligned} \tag{2.30}$$

$$\begin{cases} \tilde{\phi}^{(1)} = 0 & \& \quad n^{(1)} = 0 & \text{on} \quad \Gamma_1 \\ \partial_{\tilde{x}} \tilde{\phi}^{(1)} = 0 & \& \quad \partial_{\tilde{x}} n^{(1)} = 0 & \text{on} \quad \Gamma_2 \quad \& \quad \Gamma_3 \\ \tilde{\phi}^{(1)} = 1 & \& \quad \partial_{\tilde{y}} n^{(1)} = -4 \frac{c_{ion}^{(0)}}{c_{eon}^{(0)}} \partial_{\tilde{y}} \tilde{\phi}^{(1)} & \text{on} \quad \Gamma_4 \\ \partial_{\tilde{y}} \tilde{\phi}^{(1)} = \tilde{A}_\phi n^{(1)} & \& \quad \partial_{\tilde{y}} n^{(1)} = \tilde{A}_n n^{(1)} & \text{on} \quad \Gamma_5 \end{cases} . \tag{2.31}$$

2.4.2.1 Numerical Method

In order to solve numerically the Equations (2.30) with the boundary conditions (2.31) we employ an h-adapted finite element method (FEM). FEM is well known for elliptic problems such as the one we are studying, see for example [Fic65] and [QV94].

In order to employ FEM appropriately, we first recast the problem in the following weak form, where m and ψ are test functions on the domain Ω

$$\int_\Omega \nabla m \cdot \nabla n^{(1)} \, \mathrm{d}\mathcal{A} + 4 \frac{c_{ion}^{(0)}}{c_{eon}^{(0)}} \int_{\Gamma_4} m \partial_{\tilde{y}} \tilde{\phi}^{(1)} \, \mathrm{d}\gamma - \tilde{A}_n \int_{\Gamma_5} m n^{(1)} \, \mathrm{d}\gamma = 0 \tag{2.32a}$$

$$\int_\Omega \nabla \psi \cdot \nabla \phi^{(1)} \, \mathrm{d}\mathcal{A} - \tilde{A}_\phi \int_{\Gamma_5} \psi n^{(1)} \, \mathrm{d}\gamma = 0 \tag{2.32b}$$

---

then since $c_{eon}^{(1)} = 2 c_{ion}^{(1)}$

$$\begin{cases} \partial_y n^{(1)} - \partial_y \tilde{\phi}^{(1)} = \frac{\dot{\omega}_{eon}^{(1)}}{c_{eon}^{(0)} D_{eon}} \\ \frac{c_{eon}^{(0)}}{c_{ion}^{(0)}} \partial_y n^{(1)} + 4 \partial_y \tilde{\phi}^{(1)} = \frac{\dot{\omega}_{eon}^{(1)}}{c_{ion}^{(0)} D_{ion}} \end{cases} \Leftrightarrow \begin{bmatrix} 1 & -1 \\ \frac{c_{eon}^{(0)}}{c_{ion}^{(0)}} & 4 \end{bmatrix} \begin{Bmatrix} \partial_y n^{(1)} \\ \partial_y \tilde{\phi}^{(1)} \end{Bmatrix} = \dot{\omega}_{eon} \begin{Bmatrix} \frac{1}{c_{eon}^{(0)} D_{eon}} \\ \frac{1}{c_{ion}^{(0)} D_{ion}} \end{Bmatrix}$$

Solving the

$$\begin{cases} \partial_y n^{(1)} = -\frac{k_f \tilde{p}_{H_2}}{2 D_{ion} c_{ion}^{(0)}} \left(1 + 4 \frac{D_{ion} c_{ion}^{(0)}}{D_{eon} c_{eon}^{(0)}} \right) n^{(1)} \\ \partial_y \tilde{\phi}^{(1)} = -\frac{k_f \tilde{p}_{H_2}}{2 D_{ion} c_{ion}^{(0)}} \left(1 - \frac{D_{ion}}{D_{eon}} \right) n^{(1)} \end{cases}$$

with the additional conditions that

$$\tilde{\phi}^{(1)} = 0 \quad \text{on} \quad \Gamma_1 \tag{2.33a}$$

$$n^{(1)} = 1 \quad \text{on} \quad \Gamma_1 \tag{2.33b}$$

$$\tilde{\phi}^{(1)} = 1 \quad \text{on} \quad \Gamma_4 \tag{2.33c}$$

The discrete version of equations (2.32) is then solved using FreeFem++ [HP07b]. The equations are initially discretized on a triangular unstructured mesh, using quadratic continuous basis functions with a third order bubble. The mesh is adaptively refined up to seven times at each solution step and the *a posteriori* adaptation is performed against $\tilde{\mu}_{eon}^{(1)}$. The h-adaptation ensures high regularity of the H^1 *a posteriori* estimator [BS00], locally below 0.01%, and it guarantees that the mesh is finer where the sharpest gradients occur. We note that mesh adaptivity results in coarseness everywhere except in the vicinity of the interfaces. In particular, the refinement increases as we approach the triple phase boundary; this fact indicates strong nonlinearities around that area. Eleven integral tests were also implemented in order to ensure that at each solution step the numerical method satisfies conservation of species and charge.

Finally we note that FreeFem++ execution time is comparable to custom-written C++ code and its speed is enhanced by the utilization of fast direct linear solvers such as the multifrontal package UMFPACK [Dav04]. Due to the sparsity of the problem we make extensive use of the latter feature.

2.5 Time Dependent Modeling

2.5.1 Asymptotic Modeling of Mixed Conduction in the Bulk

We focus now on the time dependent version of equations (2.14) and we will utilize the same approach of section 2.4. We will perturb the fundamental equations as follows:

$$\begin{aligned}
\triangle(1+\tilde{\phi}^{(1)}) &= \lambda^2\left(1+\bar{n}(1+n^{(1)})-2\bar{p}(1+p^{(1)})\right) && \text{(2.34a)}\\
\frac{\tau_n}{\tau}\partial_t\left(1+n^{(1)}\right) &+ \nabla_{\tilde{x}}\cdot\left(-\nabla_{\tilde{x}}(1+n^{(1)})+(1+n^{(1)})\nabla_{\tilde{x}}\tilde{\phi}^{(1)}\right)=0, && \text{(2.34b)}\\
\frac{\tau_p}{\tau}\partial_t\left(1+p^{(1)}\right) &- \nabla_{\tilde{x}}\cdot\left(\nabla_{\tilde{x}}(1+p^{(1)})+2(1+p^{(1)})\nabla_{\tilde{x}}\tilde{\phi}^{(1)}\right)=0. && \text{(2.34c)}
\end{aligned}$$

If we retain in (2.34) only first order terms, we will obtain

$$\begin{aligned}
\triangle\tilde{\phi}^{(1)} &= \lambda^2\left(n^{(1)}-2\bar{p}p^{(1)}\right) && \text{(2.35a)}\\
\frac{\tau_n}{\tau}\partial_{\tilde{t}}n^{(1)} &- \triangle_{\tilde{x}}n^{(1)}+\triangle_{\tilde{x}}\tilde{\phi}^{(1)}=0, && \text{(2.35b)}\\
\frac{\tau_p}{\tau}\partial_{\tilde{t}}p^{(1)} &- \triangle_{\tilde{x}}p^{(1)}-2\triangle_{\tilde{x}}\tilde{\phi}^{(1)}=0. && \text{(2.35c)}
\end{aligned}$$

The electroneutrality condition, zero total charge, at first order gives $p^{(1)}=\frac{1}{2}\frac{c_{eon}^{(0)}}{c_{ion}^{(0)}}n^{(1)}=\frac{1}{2}\frac{\bar{n}}{\bar{p}}n^{(1)}$. Using the latter we can drop (2.35a). Defining the following two time scales:

$$\begin{aligned}
\tau_n^{\star} &= \frac{\tau_n+\frac{\bar{n}}{4\bar{p}}\tau_p}{1+\frac{\bar{n}}{4\bar{p}}}, && \text{(2.36a)}\\
\tau_{\phi}^{\star} &= \frac{\tau_p-\tau_n}{1+\frac{4\bar{p}}{\bar{n}}}, && \text{(2.36b)}
\end{aligned}$$

helps rewrite the (2.35) as (see also appendix C) a

$$\frac{\tau_n^\star}{\tau}\partial_{\tilde{t}} n^{(1)} - \triangle_{\tilde{x}} n^{(1)} = 0, \tag{2.37a}$$

$$\frac{\tau_\phi^\star}{\tau}\partial_{\tilde{t}} n^{(1)} - \triangle_{\tilde{x}} \tilde{\phi}^{(1)} = 0. \tag{2.37b}$$

2.5.2 Boundary Conditions for the Time Dependent Case

It follows from symmetry, figure 2.1, that $\partial_{\tilde{x}}\tilde{\phi}^{(1)} = \partial_{\tilde{x}}\tilde{n}^{(1)} = 0$ on Γ_2 and Γ_3. Since the metal is ion blocking, the condition $\frac{1}{2}\frac{\bar{n}}{\bar{p}}\partial_{\tilde{y}} n^{(1)} + 2\partial_{\tilde{y}}\tilde{\phi}^{(1)} = 0$ will be satisfied on Γ_4. We assume as well that the response of the metal to an electric perturbation is fast compared to the MIEC, and it follows that we can take the electric potential $\tilde{\phi}^{(1)}$ uniform on Γ_4. Due to inherent linearity and given the impedance setting, we can choose $\tilde{\phi}^{(1)} = \frac{1}{\sqrt{2\pi}}\Re\left(e^{i\omega\tau\tilde{t}}\right)$ on Γ_4 and $\tilde{\phi}^{(1)} = n^{(1)} = 0$ on Γ_1.

We assume the chemistry of the chemical reactions on Γ_5 has a finite speed and that it is correctly characterized by a one-step reaction [CWHG09] which is frequency independent (for a generalization see appendix C). Hence the y-flux of electrons and vacancies can be assumed to satisfy the same Chang-Jaffé condition that we derived in Section 2.4.1, giving the following expression along Γ_5: $\mathbf{j}_{eon}^P \cdot \mathbf{e}_y = 2\mathbf{j}_{ion}^P \cdot \mathbf{e}_y = -\dot{\omega}_{eon,S}$. If we define $\tilde{A}_\phi = \tilde{k}_f \frac{\tilde{p}_{H_2}}{c_{ion}^{(0)}}\left(1 - \frac{D_{ion}}{D_{eon}}\right)$ and $\tilde{A}_n = \tilde{k}_f \frac{\tilde{p}_{H_2}}{c_{ion}^{(0)}}\left(1 + 4\frac{D_{ion}c_{ion}^{(0)}}{D_{eon}c_{eon}^{(0)}}\right)$, we can rewrite the boundary conditions on Γ_5 as $\partial_{\tilde{y}}\hat{\phi}^{(1)} = \tilde{A}_\phi \hat{n}^{(1)}$ and $\partial_{\tilde{y}}\hat{n}^{(1)} = \tilde{A}_n \hat{n}^{(1)}$.

2.5.3 Weak Formulation of the Time Dependent Model

If we Fourier transform (2.37) and the boundary conditions with respect to $\tilde{t}$[¶], we find the following system of elliptic equations ($\hat{(\cdot)}$ indicates Fourier transformed quantity)[‖] which we call IS equations

$$i\omega\tau_n^\star\hat{n}^{(1)} - \triangle\hat{n}^{(1)} = 0, \tag{2.38a}$$

$$i\omega\tau_\phi^\star\hat{n}^{(1)} - \triangle\hat{\phi}^{(1)} = 0, \tag{2.38b}$$

with boundary conditions:

$$\begin{array}{llll}
\hat{\phi}^{(1)} = 0 & \& \quad \hat{n}^{(1)} = 0 & \text{on} \quad \Gamma_1, & \\
\partial_{\tilde{x}}\hat{\phi}^{(1)} = 0 & \& \quad \partial_{\tilde{x}}\hat{n}^{(1)} = 0 & \text{on} \quad \Gamma_2 \quad \& \quad \Gamma_3, & \\
\hat{\phi}^{(1)} = 1 & \& \quad \partial_{\tilde{y}}\hat{n}^{(1)} = -4\frac{\bar{p}}{\bar{n}}\partial_{\tilde{y}}\hat{\phi}^{(1)} & \text{on} \quad \Gamma_4, & \\
\partial_{\tilde{y}}\hat{\phi}^{(1)} = \tilde{A}_\phi\hat{n}^{(1)} & \& \quad \partial_{\tilde{y}}\hat{n}^{(1)} = \tilde{A}_n n^{(1)} & \text{on} \quad \Gamma_5, &
\end{array} \tag{2.39}$$

We can recast the (2.38) and (2.39) in weak form taking as test functions m_{Re}, $m_{Im} \in H^1(\Omega \setminus \Gamma_1)$, ψ_{Re}, $\psi_{Im} \in H^1(\Omega \setminus (\Gamma_1 \cup \Gamma_4))$ [AF03]:

[¶]We choose unitary Fourier transform $\hat{f}(\omega) = \frac{1}{\sqrt{2\pi}}\int_{-\infty}^{\infty} f(x)e^{-i\omega x}\,\mathrm{d}x$.

[‖]We factored out the Dirac distribution that comes out of Fourier transformation of an exponential.

$$\begin{aligned}\omega\tau_n^\star\int_\Omega \hat{n}_{Im}^{(1)} m_{Re}\,\mathrm{d}\tilde{A} \;&-\; \int_\Omega \nabla\hat{n}_{Re}^{(1)}\cdot\nabla m_{Re}\,\mathrm{d}\tilde{A} + \int_{\Gamma_5}\tilde{A}_n\hat{n}_{Re}^{(1)} m_{Re}\,\mathrm{d}\tilde{x} + \\ &-\; 4\frac{\bar{p}}{\bar{n}}\int_{\Gamma_4}\partial_{\tilde{y}}\hat{\phi}_{Re}^{(1)} m_{Re}\,\mathrm{d}\tilde{x} = 0,\end{aligned} \tag{2.40a}$$

$$\begin{aligned}\omega\tau_n^\star\int_\Omega \hat{n}_{Re}^{(1)} m_{Im}\,\mathrm{d}\tilde{A} \;&+\; \int_\Omega \nabla\hat{n}_{Im}^{(1)}\cdot\nabla m_{Im}\,\mathrm{d}\tilde{A} - \int_{\Gamma_5}\tilde{A}_n\hat{n}_{Im}^{(1)} m_{Im}\,\mathrm{d}\tilde{x} \\ &+\; 4\frac{\bar{p}}{\bar{n}}\int_{\Gamma_4}\partial_{\tilde{y}}\hat{\phi}_{Im}^{(1)} m_{Im}\,\mathrm{d}\tilde{x} = 0,\end{aligned} \tag{2.40b}$$

$$\omega\tau_\phi^\star\int_\Omega \hat{n}_{Im}^{(1)}\psi_{Re}\,\mathrm{d}\tilde{A} - \int_\Omega \nabla\hat{\phi}_{Re}^{(1)}\cdot\nabla\psi_{Re}\,\mathrm{d}\tilde{A} + \int_{\Gamma_5}\tilde{A}_\phi\hat{n}_{Re}^{(1)}\psi_{Re}\,\mathrm{d}\tilde{x} = 0, \tag{2.40c}$$

$$\omega\tau_\phi^\star\int_\Omega \hat{n}_{Re}^{(1)}\psi_{Im}\,\mathrm{d}\tilde{A} + \int_\Omega \nabla\hat{\phi}_{Im}^{(1)}\cdot\nabla\psi_{Im}\,\mathrm{d}\tilde{A} - \int_{\Gamma_5}\tilde{A}_\phi\hat{n}_{Im}^{(1)}\psi_{Im}\,\mathrm{d}\tilde{x} = 0. \tag{2.40d}$$

with the additional condition that:

$$\hat{\phi}_{Re}^{(1)} = 0 \quad \& \quad \hat{\phi}_{Im}^{(1)} = 0 \quad \text{on} \quad \Gamma_1, \tag{2.41a}$$

$$\hat{n}_{Re}^{(1)} = 0 \quad \& \quad \hat{n}_{Im}^{(1)} = 0 \quad \text{on} \quad \Gamma_1, \tag{2.41b}$$

$$\hat{\phi}_{Re}^{(1)} = 1 \quad \& \quad \hat{\phi}_{Im}^{(1)} = 0 \quad \text{on} \quad \Gamma_4. \tag{2.41c}$$

It is easy to show that the sum of (2.40) is bounded and thus the bilinear form associated to the weak formulation of (2.38) with (2.39) is continuous. Further, the problem is weakly coercive hence it admits one unique solution [Agm65].

2.5.4 Numerical Solution Procedure for the Two-Dimensional Case

In order to solve numerically (2.40) with boundary conditions (2.41) we employ an h-adapted finite element method (FEM), implemented with FreeFem++ [HP07b]. The governing equations are discretized on a triangular unstructured mesh using quadratic continuous basis

functions with a centered third order bubble. We use a direct method to solve the linear system following integration of (2.40) in the discretized mesh. Then the mesh is adaptively refined nine times for each case. The *a posteriori* adaptation is performed the first six times against the 4 dimensional vector $\left(\nabla\Re\left[\hat{\mu}_{eon}^{(1)}\right], \nabla\Re\left[\hat{\mu}_{ion}^{(1)}\right]\right)$ and subsequently against η_ε (see appendix A). The h-adaptation ensures high regularity of the H^1 *a posteriori* estimator [BS00], locally below 10^{-5}, and it guarantees that the mesh is finer where sharper gradients occur. Independent of frequency, mesh adaptivity results in coarseness everywhere except in the vicinity of the interfaces, in particular the refinement increases towards the triple-phase boundary (the intersection of metal, oxide and gas phases, which is thought to be a particularly active site for electrochemical reactions [Tro01] [MST00]); this fact indicates strong non-linearities around that area. Finally we note that FreeFem++ execution time is comparable to custom-written C++ code and its speed is enhanced by the utilization of fast sparse linear solvers such as the multi-frontal package UMFPACK [Dav04]. Due to the sparsity of the problem we make extensive use of this last feature. We further note that the utilization of asymptotic expansion and Fourier transformation techniques, while guaranteeing linearity, has a great speed advantage over direct sinusoidal [Goo06] and step relaxation techniques [Bes07]. Further, this method can be directly used to examine chemical reactions within the cell and draw directly conclusions about fast and rate-limiting chemical reactions. Also, this procedure lends itself to direct error estimation and its implementation can be done automatically for a time-dependent problem [CG07].

2.5.5 One-Dimensional Case: Analytical Solution

Since we also aim at comparing the 1D and 2D solutions, it is beneficial to revisit the 1D solution of (2.38) [Mac73]. The solution $(\hat{n}^{(1)}, \hat{\phi}^{(1)})$ will satisfy (if $\omega \neq 0$):

$$\hat{n}^{(1)} = \sum_{\pm} a_{\pm} e^{\pm\sqrt{i}\sqrt{\tau_n^\star\omega}\tilde{y}}, \tag{2.42a}$$

$$\hat{\phi}^{(1)} = \hat{\phi}_0^{(1)} + (\hat{\phi}_0^{(1)})'\tilde{y} + \frac{\tau_\phi^\star}{\tau_n^\star}\hat{n}^{(1)}, \tag{2.42b}$$

where for simplicity we indicate $\sqrt{i} = e^{i\frac{\pi}{4}}$. The boundary conditions, as in the 2D case, at $\tilde{y} = 0$ (Γ_1) are

$$\hat{\phi}^{(1)} = 0 \quad \& \quad \hat{n}^{(1)} = 0. \tag{2.43}$$

The latter can help rewrite (2.42) as

$$\hat{n}^{(1)} = 2a_+ \sinh\left(\sqrt{i}\sqrt{\tau_n^\star\omega}\tilde{y}\right), \tag{2.44a}$$

$$\hat{\phi}^{(1)} = (\hat{\phi}_0^{(1)})'\tilde{y} + 2a_+\frac{\tau_\phi^\star}{\tau_n^\star}\sinh\left(\sqrt{i}\sqrt{\tau_n^\star\omega}\tilde{y}\right). \tag{2.44b}$$

If we set $\gamma_\phi = \frac{R_{ion}^\perp e l_c D_e c_{eon}^{(0)}}{U_T\left(1+\frac{1}{4}\frac{\bar{n}}{\bar{p}}\right)}$ and $\gamma_n = \frac{1}{4}\frac{\bar{n}}{\bar{p}}\gamma_\phi$, then at $\tilde{y} = l_2$ we have the following conditions [LH05]:

$$\hat{\phi}^{(1)} = 1 \quad \& \quad \hat{n}^{(1)} + \gamma_\phi\frac{d\hat{\phi}^{(1)}}{d\tilde{y}} + \gamma_n\frac{d\hat{n}^{(1)}}{d\tilde{y}} = 0. \tag{2.45}$$

The boundary conditions (2.45) will lead to the determination of a_+ and $(\hat{\phi}_0^{(1)})'$ in (2.44) and the 1D model leads to the impedance given in (3.23). We will expand on the 1D analytical solution in next chapter.

Chapter 3

One Dimensional Modeling

In this chapter we will discuss equivalent circuit representation of electrochemical systems and we will focus on the analytical derivation of the impedance response of the two systems in figure 1.5. This serves as a starting point for later multidimensional analysis and the new formula derived in Section 3.2.2 can be used as a starting point for the experimental analysis of blocking electrode conditions.

3.1 Equivalent Circuits

The most attractive aspect of IS as a tool for understanding electrochemical properties of materials is the direct link between the behavior of the system and that of model circuits, consisting of discrete electric circuits. Experimentalists typically fit impedance data to physically plausible equivalent circuits, which represent the basic physical-chemical phenomena taking place in the system under study. Hence, there exist some map between the experimental results and the physics of the system via equivalent circuits. This makes the utilization of one-dimensional models interesting and useful. The impedance mapping to an equivalent circuit is unique as proved by Bott and Duffin in 1949 [BD49] and [BIG03]*

*A passive 1-port is a box filled with various resistors, capacitors and inductors, with two wires sticking out. If one applies a current $I(t) = \exp(i\omega t)$, the response voltage across the port will be $V(t) = Z(\omega)\exp(i\omega t)$, where $Z(\omega)$ is called the impedance of the circuit. It is fairly easy to see that Z is a rational function with real coefficients, mapping the right half-plane to itself. Such functions are called

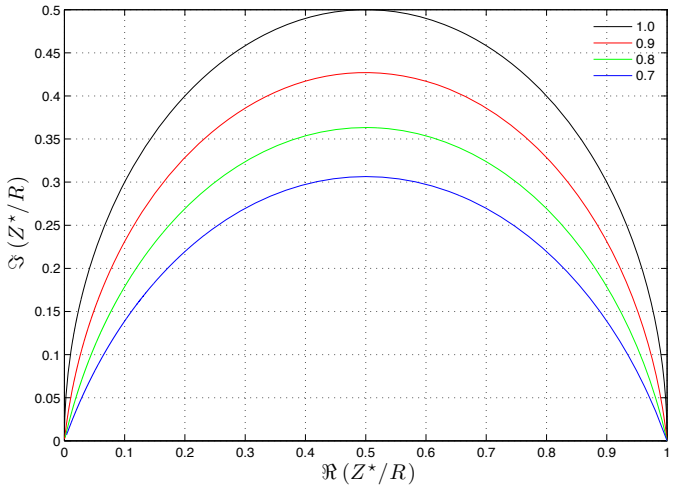

Figure 3.1: The Nyquist plot of the impedance of a ZARC circuit normalized versus R and parametrized as a function of α.

however the interpretation of the underlying physical phenomena may not be unique, may not be one-dimensional, may not be rational (with the presence of disordered systems) and furthermore, sufficient scattering of the data can result in non unique deconvolution of the equivalent circuit.

We shall start with a brief review on a few elementary circuit elements: the resistors, the capacitor and the inductor. Each one represents a different physical phenomena, the resistor indicates the "resistance" to conduction of ions or electrons, the capacitor can indicate double layer build up (a common phenomenon at interfaces), and the inductor indicates the coupling between magnetic and electric field. In SOFCs we can easily assume that magnetization is not present, thus it is apparent that resistors and capacitors and their combinations will be the only elements. We report the impedance of these elementary circuit elements in table 3.1.

Another common element is the Constant Phase Element (CPE) whose Fourier response

prfs in the literature. The fundamental result of circuit theory, proved by Bott and Duffin, asserts that every prf is the impedance of some 1-port. This is really a result in complex analysis.

Table 3.1: Elementary circuit elements and their Fourier transform $\Delta V(t)$ is the potential drop at the element's ends, $I(t)$ the current passing through the circuit and the symbol $\hat{(\cdot)}$ indicates the Fourier transform.

Name	Time Dependence	Fourier Transform	Impedance
Resistor	$\Delta V(t) = RI(t)$	$\Delta\hat{V} = R\hat{I}$	R
Capacitor	$Q = C\Delta V$	$\hat{I} = i\omega C\Delta\hat{V}$	$\frac{1}{i\omega C}$
Inductor	$\Delta V = L\dot{I}$	$\Delta\hat{V} = i\omega L\hat{I}$	$i\omega L$

is a generalization of the capacitance and it is defined as

$$Z_\alpha(\omega) = \frac{1}{(i\omega)^\alpha C_\alpha}, \tag{3.1}$$

Incidentally we note that $Z_{\alpha=1}$ is the impedance response of the capacitance. Solving anomalous diffusion equations with absorbing boundaries, see for example Bisquert's work [Bis02] or the more general fractional calculus monograph [KST06], gives the so-called Generalized Finite-Length Warburg Element (GFLW)

$$Z_{GFLW}(\omega) = R_{GFLW}\frac{\tanh\left((i\omega C_{GFLW})^{\alpha_{GFLW}}\right)}{(i\omega C_{GFLW})^{\alpha_{GFLW}}}, \tag{3.2}$$

with parameters R_{GFLW}, C_{GFLW} and α_{GFLW}.

We notice that $|\omega C_{GFLW}|^{\alpha_{GFLW}} \gg 1$ one recovers the CPE element. If $\alpha_{GFLW} = \frac{1}{2}$ one gets the Finite-Length Warburg Element (FLW) which will be instrumental for understanding the equivalent circuit representation of the system in figure 1.5. In the Nyquist plot, the GFLW gives a half-tear-drop arc called a Warburg arc. Such arcs are commonly retrieved when analyzing thick mixed conductors with absorbing boundaries and will be treated in more detail in the following section. Other relevant circuits for our analysis, in particular in reference with the figure 1.5(b) or thin film interfaces, is the RC circuit (a resistor and a capacitor in parallel) and its generalization, the ZARC circuit (a CPE and a resistor in

parallel). The ZARC impedance is

$$Z = \frac{1}{\dfrac{1}{R} + i\,(\omega)^{\alpha}\, C_{\alpha}}. \tag{3.3}$$

A visual Nyquist plot representation of its impedance is given in figure 3.1. As α decreases from the base value of one the perfect semicircular arc of the RC circuit becomes increasingly depressed, where the minumum of the function $-\Im(Z_{ZARC})$ occurs always for $\omega = \dfrac{1}{RC}$ and it decreases with α[†].

3.2 Linear One-Dimensional Modeling

As we have shown in Section 2.1, electroneutrality is a fair assumption for doped SOFC materials. The only equations we need to solve are the continuity equations for the migrating species along with the condition that electroneutrality is satisfied. In the general setting of N migrating species, the concentration of a species m $(m = 1, \ldots, N)$ satisfies

$$\partial_t c_m + \nabla \cdot \left(-D_m c_m \nabla \frac{\tilde{\mu}_m}{k_B T} \right) = 0. \tag{3.4}$$

If we multiply the previous equation by $z_m e$ and call $\rho_m = e z_m c_m$ the charge associated with species m, we will get

$$\partial_t \rho_m + \nabla \cdot \left(-\frac{D_m c_m z_m^2 e^2}{kBT} \nabla \mu_m^{\star} \right) = 0, \tag{3.5}$$

where $\sigma_m = \frac{D_m c_m z_m^2 e^2}{kBT}$ is the conductivity and $\mu_m^{\star} = \frac{\tilde{\mu}_m}{z_m e}$ is the star potential (or $\star-$potential).

[†]It is trivial to see that the minimum of $\Im(Z_{ZARC})$ occurs for $\Re\left(\frac{i^{-1+\alpha}}{(1+(iCRx)^{\alpha})^2}\right) = 0$ which has one solution for $\alpha \in \mathbb{R}^+$ which is $\omega = \frac{1}{RC}$ so the ZARC peak frequency is the same as the RC circuit peak frequency. The minimum of $\Im(Z_{ZARC})$ is strictly increasing with α because $|1+i| > |1+i^{\alpha}|$. It is straightforward to deduce that the depression is given by $\Im\left(i^{\alpha}\right) = \sin\left(\alpha \frac{\pi}{2}\right)$.

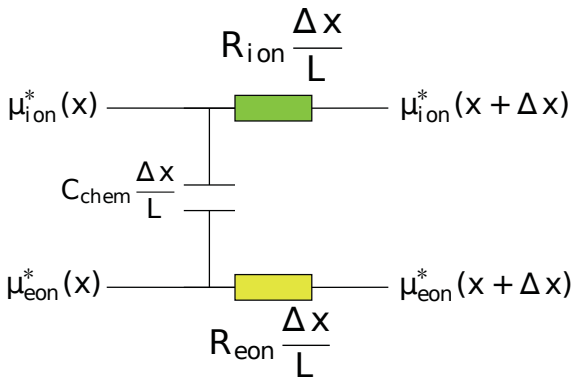

Figure 3.2: The system of equations describing mixed conductivity under the electroneutrality condition can be approximated locally as an equivalent circuit featuring one ionic and one electronic resistive rail connected by a capacitor.

If we expand the dilute electrochemical potential of species m with respect to its concentration c_m around equilibrium $c_m^{(0)}$ we will obtain that

$$\mu_m^\star = \phi + \frac{k_B T}{z_m e} \log \frac{c_m}{c_m^{(0)}} = \phi + \frac{k_B T}{z_m e} \frac{c_m - c_m^{(0)}}{c_m^{(0)}} + \frac{k_B T}{z_m e} \times o\left(\frac{c_m - c_m^{(0)}}{c_m^{(0)}} \right). \tag{3.6}$$

We now use the formulas above in the special case where the majority carriers are vacancies (ion) and electrons (eon), if we subtract the $\star$-potentials of electrons and vacancies, we will obtain

$$\mu_{eon}^\star - \mu_{ion}^\star \approx \frac{k_B T}{z_{eon} e} \frac{c_{eon}^{(1)}}{c_{eon}^{(0)}} - \frac{k_B T}{z_{ion} e} \frac{c_{ion}^{(1)}}{c_{ion}^{(0)}}, \tag{3.7}$$

where we indicated $c_m^{(1)} = c_m - c_m^{(0)}$. We can now use the electroneutrality condition, $z_{eon} c_{eon}^{(1)} + z_{ion} c_{ion}^{(1)} = 0$ to deduce that

$$\mu_{eon}^\star - \mu_{ion}^\star = \frac{k_B T}{e} \left(\frac{1}{z_{eon} c_{eon}^{(0)}} + \frac{z_{eon}}{z_{ion}^2 c_{ion}^{(0)}} \right) c_{eon}^{(1)} = \left(\frac{1}{z_{eon}^2 c_{eon}^{(0)}} + \frac{1}{z_{ion}^2 c_{ion}^{(0)}} \right) \frac{k_B T}{e} z_{eon} c_{eon}^{(1)}. \tag{3.8}$$

The latter will give that

$$\frac{e^2}{k_BT}\frac{1}{\frac{1}{z_{eon}^2c_{eon}^{(0)}}+\frac{1}{z_{ion}^2c_{ion}^{(0)}}}\left(\mu_{eon}^{\star}-\mu_{ion}^{\star}\right)=\rho_{eon}^{(1)}=z_{eon}ec_{eon}^{(1)}. \tag{3.9}$$

If we conveniently define the $\chi_{chem}=\frac{e^2}{k_BT}\frac{1}{\frac{1}{z_{eon}^2c_{eon}^{(0)}}+\frac{1}{z_{ion}^2c_{ion}^{(0)}}}$ and if we Fourier-transform with respect to time the (3.5) with $m=ion,eon$, we will get

$$\begin{aligned} i\chi_{chem}\omega\left(\hat{\mu}_{eon}^{\star}-\hat{\mu}_{ion}^{\star}\right)+\nabla\cdot\left(-\sigma_{eon}\nabla\hat{\mu}_{eon}^{\star}\right) &= 0, & (3.10a)\\ i\chi_{chem}\omega\left(\hat{\mu}_{ion}^{\star}-\hat{\mu}_{eon}^{\star}\right)+\nabla\cdot\left(-\sigma_{ion}\nabla\hat{\mu}_{ion}^{\star}\right) &= 0. & (3.10b)\end{aligned}$$

We note that the current densities are given by

$$\begin{aligned} \hat{\mathbf{j}}_{eon} &= -\sigma_{eon}\nabla\hat{\mu}_{eon}^{\star}, & (3.11a)\\ \hat{\mathbf{j}}_{ion} &= -\sigma_{ion}\nabla\hat{\mu}_{ion}^{\star}. & (3.11b)\end{aligned}$$

We now constrain our study to one spatial dimension, thus we can drop the vector notation and define the total ionic and electronic currents as the product of the respective current densities and the cross sectional area

$$\begin{aligned} \hat{I}_{eon} &= A\hat{j}_{eon}, & (3.12a)\\ \hat{I}_{ion} &= A\hat{j}_{eon}. & (3.12b)\end{aligned}$$

We will also define the resistances $R_{(\cdot)}$ and the chemical capacitance C_{chem} as follows:

$$
\begin{aligned}
R_{eon} &= \frac{L}{\sigma_{eon} A}, && (3.13a)\\
R_{ion} &= \frac{L}{\sigma_{ion} A}, && (3.13b)\\
C_{chem} &= L \chi_{chem} A. && (3.13c)
\end{aligned}
$$

In one dimension the (3.10b) can be conveniently rearranged in the following system of autonomous linear ordinary equations in $\mathbb{C}^4$:

$$
\begin{aligned}
\frac{d}{dx}\hat{\mu}^{\star}_{eon} &= -\frac{R_{eon}}{L}\hat{I}_{eon}, && (3.14a)\\
\frac{d}{dx}\hat{\mu}^{\star}_{ion} &= -\frac{R_{ion}}{L}\hat{I}_{ion}, && (3.14b)\\
\frac{d}{dx}\hat{I}^{\star}_{eon} &= i\omega\frac{C_{chem}}{L}\left(\hat{\mu}^{\star}_{ion} - \hat{\mu}^{\star}_{eon}\right), && (3.14c)\\
\frac{d}{dx}\hat{I}^{\star}_{ion} &= i\omega\frac{C_{chem}}{L}\left(\hat{\mu}^{\star}_{eon} - \hat{\mu}^{\star}_{ion}\right). && (3.14d)
\end{aligned}
$$

The equations (3.14) admit an analytical solution of the following form:

$$
\begin{aligned}
\hat{I}_{ion}(x) &= \frac{R_{eon}}{R_{ion}+R_{eon}} I_{tot} + C_1 e^{kx} + C_2 e^{-kx}, && (3.15a)\\
\hat{I}_{eon}(x) &= \hat{I}_{tot} - \hat{I}_{ion}(x), && (3.15b)\\
\hat{\mu}^{\star}_{ion}(x) &= -\frac{R_{eon}R_{ion}}{R_{ion}+R_{eon}}\frac{x}{L} I_{tot} - C_1\left(e^{kx}-1\right) + C_2\left(e^{-kx}-1\right) + \left(\mu^{\star}_{ion}\right)_0, && (3.15c)\\
\hat{\mu}^{\star}_{eon}(x) &= -\frac{R_{eon}R_{ion}}{R_{ion}+R_{eon}}\frac{x}{L} I_{tot} + C_1\left(e^{kx}-1\right) - C_2\left(e^{-kx}-1\right) + \left(\mu^{\star}_{ion}\right)_0, && (3.15d)
\end{aligned}
$$

where $k = \frac{1}{L}\sqrt{i\omega C_{chem}\,(R_{ion} + R_{eon})}$. In the remainder of this chapter we will suppose that

- the sample is the segment $[-L, L]$;
- the electrochemical potential of electrons in the sample is set at the boundaries and it is harmonically varying according as $\exp(i\omega t)$;
- the ionic rail is electrically connected to the current collector via a certain resistance.

It follows immediately from the assumptions above that the equations (3.14) satisfy the following boundary conditions:

$$\hat{\mu}^{\star}_{ion}(x = 0) = 0, \tag{3.16a}$$

$$\hat{\mu}^{\star}_{eon}(x = L) = 1, \tag{3.16b}$$

$$\hat{\mu}^{\star}_{eon}(x = L) = \hat{\mu}^{\star}_{ion}(x = L) - Z^{\perp}_{ion}\hat{I}_{ion}(x = L). \tag{3.16c}$$

Incidentally, plugging in (3.16) into (3.15) gives that

$$(\hat{\mu}^{\star}_{eon})_0 = (\hat{\mu}^{\star}_{ion})_0 + (C_1 - C_2)\frac{R_{eon} + R_{ion}}{kL}, \tag{3.17a}$$

$$(\hat{\mu}^{\star}_{ion})_0 = 0; \tag{3.17b}$$

hence, we can safely drop the boundary condition (3.16a).

The equations (3.14) have the characteristic that they can be mapped easily into an equivalent circuit with "infinitesimal" elements. From elementary calculus, we recall that

the derivative of a continuosly differentiable function can be approximated by a forward finite difference, with constant step $\Delta x \to 0$, i.e., $\frac{df}{dx} \approx \frac{\Delta f}{\Delta x}$, then

$$\hat{\mu}^{\star}_{eon}(x+\Delta x) - \hat{\mu}^{\star}_{eon}(x) = -\frac{R_{eon}}{L}\hat{I}_{eon}(x)\Delta x, \tag{3.18a}$$

$$\hat{\mu}^{\star}_{ion}(x+\Delta x) - \hat{\mu}^{\star}_{ion}(x) = -\frac{R_{ion}}{L}\hat{I}_{ion}(x)\Delta x, \tag{3.18b}$$

$$\hat{I}^{\star}_{eon}(x+\Delta x) - \hat{I}^{\star}_{eon}(x) = i\omega\frac{C_{chem}}{L}\left(\hat{\mu}^{\star}_{ion}(x) - \hat{\mu}^{\star}_{eon}(x)\right)\Delta x, \tag{3.18c}$$

$$\hat{I}^{\star}_{ion}(x+\Delta x) - \hat{I}^{\star}_{ion}(x) = i\omega\frac{C_{chem}}{L}\left(\hat{\mu}^{\star}_{eon}(x) - \hat{\mu}^{\star}_{ion}(x)\right)\Delta x. \tag{3.18d}$$

Using Kirchhoff's laws, one deduces that the (3.18) have locally the same Fourier transform of the equivalent circuit in figure 3.2; a derivation of the latter property can be found in the works of Lai [Lai07] or Jamnick and Maier [JM01].

We will now study in more detail two very relevant analytical solutions of (3.14). The first expression we will derive corresponds to the single slab case, figure 1.5(a), while the second corresponds to the blocking electrode case, figure 1.5(b). These analytical expressions will pave the way for the two dimensional results.

3.2.1 Single Slab Case

The single slab case, 1.5(a), can be conveniently mapped into an equivalent circuit featuring an ionic and an electronic rail connected to one another by an infinite number of capacitors. At the two ends of the circuit the ionic rail merges into the electronic rail and the current is drawn out via a metal current collector giving rise to a polarization resistance or an area specific resistance denoted by $Z^{\perp}_{ion}$. From the circuit we can note that the system is mirror

Table 3.2: Definitions of the key terms in the 1D model of the single-slab system of figure 1.5(a)

$R_{ion}^{\perp}$	Measured
R_{eon}	$2L/\sigma_{eon}$
R_{ion}	$2L/\sigma_{ion}$
R_0	$1/\left(1/R_{eon} + 1/\left(R_{ion} + 2Z_{ion}^{\perp}\right)\right)$
R_∞	$1/\left(1/R_{eon} + 1/R_{ion}\right)$
C_{chem}	$\frac{e^2}{k_b T} 2l_2 / \left(1/(z_{eon}^2 c_{eon}^{(0)}) + 1/(z_{ion}^2 c_{ion}^{(0)})\right)$
$\tilde{D}$	$4L^2/\left(\left(R_{ion} + R_{eon}\right) C_{chem}\right)$
s	$\sqrt{i\omega L^2/(\tilde{D})}$

symmetric and, as a consequence, that

$$\hat{\mu}_{eon}^{\star}(x = 0) = 0, \tag{3.19}$$

which in turn gives that

$$(\hat{\mu}_{eon}^{\star})_0 = 0, \tag{3.20a}$$

$$C_1 = C_2. \tag{3.20b}$$

A few algebraic manipulations of (3.18) will lead to the determination of C_1 and I_{tot}, where I_{tot} denotes the total current out of the system

$$C_1 = \frac{kLZ_{ion}^{\perp}}{2kLZ_{ion}^{\perp}R_{ion}\cosh(kL) + 2\left(R_{ion}^2 + R_{eon}(Z_{ion}^{\perp} + R_{ion})\right)\sinh(kL)}, \tag{3.21}$$

$$I_{tot} = \frac{(R_{eon} + R_{ion})(-kLZ_{ion}^{\perp}\cosh(kL) - (R_{eon} + R_{ion})\sinh(kL))}{kLR_{eon}Z_{ion}^{\perp}R_{ion}\cosh(kL) + R_{eon}\left(R_{ion}^2 + R_{eon}(Z_{ion}^{\perp} + R_{ion})\right)\sinh(kL)}. \tag{3.22}$$

The total impedance of the sample is $Z = -\dfrac{2}{I_{tot}}$ and can be rearranged in the following

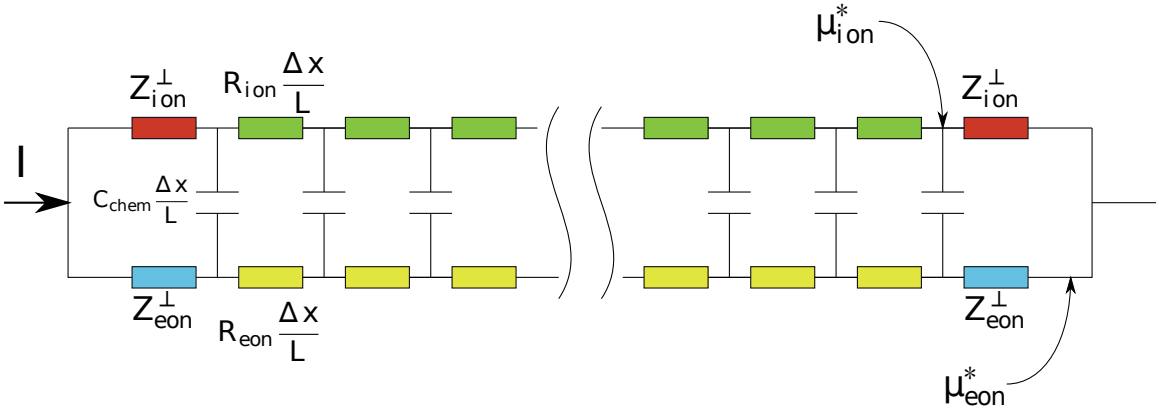

Figure 3.3: One dimensional equivalent circuit representation of the single slab problem of figure 1.5(a).

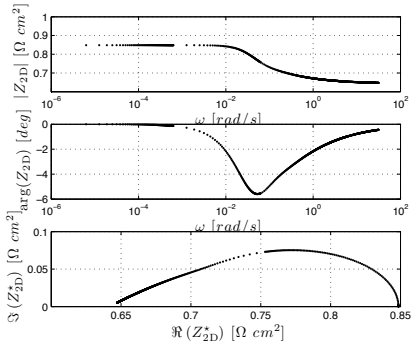

Figure 3.4: One dimensional equivalent circuit representation of the thin film system of figure 1.5(b). The electronic rail has zero net current at the YSZ | MIEC interface.

way:

$$Z = R_\infty + (R_0 - R_\infty)\left(1 + \frac{R_{ion} + R_{eon}}{2R_{ion}}\right)\frac{\tanh s}{s + \dfrac{R_{ion} + R_{eon}}{2Z^{\perp}_{ion}}\tanh s} \tag{3.23}$$

where the key parameters are reported in table 3.2. The impedance response has been extensively studied numerically and experimentally in the case of Ceria by Lai and Haile [LH05]. We report here the graph of the expression (3.23) in figure 3.4, it is clear that a Warbürg type of response is recovered (a tear drop shape in the Nyquist plot).

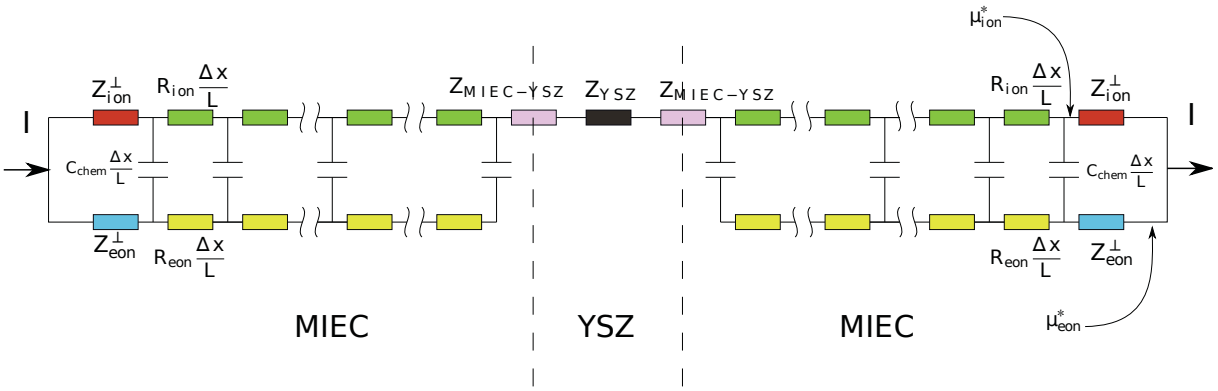

Figure 3.5: One dimensional equivalent circuit representation of the thin film system of figure 1.5(b). The electronic rail has zero net current at the YSZ | MIEC interface.

3.2.2 Blocking Electrode Case

The blocking electrode of figure 1.5(b) has an equivalent circuit representation given in figure 3.5. The electronic current is blocked at the interface between the ionic conductor and the mixed conductor. Physically this is equivalent to the assumption that the ionic conductor has infinite electronic resistivity. In this case we can assume

$$I_{eon}(x=0) = 0. \tag{3.24}$$

From the latter condition it will follow that

$$I_{tot} = \frac{R_{eon} + R_{ion}}{R_{ion}} \left(C_1 + C_2\right), \tag{3.25}$$

which leaves only the boudary conditions at $x = L$

$$C_1 = \frac{\left(e^{-kL} kL \left(e^{kL} kL R_{eon} Z_{ion}^{\perp} - R_{ion}\left(R_{eon} - kL Z_{ion}^{\perp} + R_{ion}\right)\right)\right)}{\text{denominator}}, \tag{3.26}$$

$$C_2 = \frac{\left(kL \left(-kL R_{eon} Z_{ion}^{\perp} - e^{kL} R_{ion}\left(R_{eon} + kL Z_{ion}^{\perp} + R_{ion}\right)\right)\right)}{\text{denominator}}, \tag{3.27}$$

Table 3.3: Definitions of the key terms in the 1D model of the thin-film system of figure 1.5(b)

R_0	$R_{ion} + Z_{ion}^{\perp}$
R_∞	$\dfrac{1}{\dfrac{1}{R_{eon}} + \dfrac{1}{R_{ion}}}$
N_0	$-kL\gamma_0$
N_{ch}	$kL(\gamma_0 + \gamma_1)$
N_{sh}	$k^2L^2 - \gamma_1$
D_{ch}	$\dfrac{kL(R_{eon} + R_{ion})}{Z_{ion}^{\perp}}$
D_{sh}	k^2L^2
γ_0	$\dfrac{2R_\infty}{Z_{ion}^{\perp} + \frac{R_{ion}}{R_{eon}}R_\infty}$
γ_1	$\dfrac{R_{ion}^2}{Z_{ion}^{\perp}\left(Z_{ion}^{\perp} + \frac{R_{ion}}{R_{eon}}R_\infty\right)}$

where

$$\begin{aligned} \text{denominator} &= 4kLR_{eon}Z_{ion}^{\perp}R_{ion} \\ &+ 2kL\left(R_{eon}R_{ion}^2 + Z_{ion}^{\perp}R_{ion}^2 + R_{eon}^2(Z_{ion}^{\perp} + R_{ion})\right)\cosh(kL) \\ &+ 2R_{ion}\left(k^2L^2R_{eon}Z_{ion}^{\perp} + R_{ion}(R_{eon} + R_{ion})\right)\sinh(kL). \end{aligned} \tag{3.28}$$

This allows us to compute the impedance of the circuit Z, which is given by

$$\begin{aligned} Z &= -\frac{1}{I_{tot}} \\ &= R_0 + (R_\infty - R_0)\,\frac{N_0 + N_{ch}\cosh(kL) + N_{sh}\sinh(kL)}{D_{ch}\cosh(kL) + D_{sh}\sinh(kL)}, \end{aligned} \tag{3.29}$$

where $\lim_{\omega\to 0} Z(\omega) = R_0$ and $\lim_{\omega\to\infty} Z(\omega) = R_\infty$, all the parameters in (3.29) are given explicitely in table 3.3.

We report the graph of the expression (3.29) in the limiting cases that the thickness l_2 is small, $1\mu m$, and large, $1000\mu m$. In the case $l_2 = 1\mu m$, figure 3.6, the resistance to

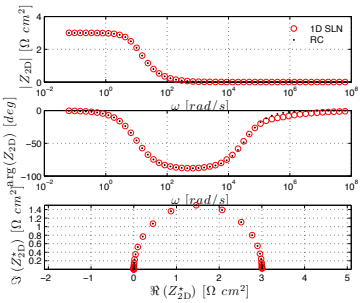

Figure 3.6: Impedance response of a one-dimensional equivalent circuit thin film figure 3.3, with $l_2 = 1\mu m$, where the electronic rail has zero net current at the YSZ | MIEC interface and the area specific polarization resistance is $3\Omega cm^2$and other conditions are derived from table 2.1 at 650^oC. An RC circuit behavior is recovered which is indicated with black dots.

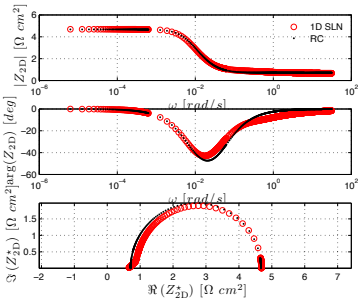

Figure 3.7: Impedance response of a one-dimensional equivalent circuit thin film figure 3.3, with $l_2 = 1000\mu m$. All other conditions are the same as in figure 3.6. For completeness the closest RC circuit is plotted with black dots.

ionic conduction is negligible and the response of the sample is very close to that of an RC circuit where R is the resistance to the chemical reactions at the mixed conductor | gas interface and C is the chemical capacitance, defined in table 3.2. In the case$l_2 = 1000\mu m$, see figure 3.7, deviations from the RC behavior are apparent at high frequency where a shoulder appears in the Nyquist plot. This feature emerges for blocking mixed conductors whenever the resistance of the ionic rail and of the polarization have the same order of magnitude [FBB$^+$06].

Chapter 4

Two-Dimensional Steady State Modeling

A two-dimensional small bias model has been developed for a patterned metal current collector | mixed oxygen ion and electronic conductor (MIEC) | patterned metal current collector electrochemical cell in a symmetric gas environment figure 2.1. Specifically, we compute the electrochemical potential distributions of oxygen vacancies and electrons in the bulk and near the surface for Pt | $Sm_{0.15}Ce_{0.85}O_{1.925}$ | Pt symmetric cell in a $H_2 - H_2O - Ar$ (reducing) atmosphere from 500 to 650^oC. Using a two-dimensional finite-element model, we show that two types of electronic current exist within the cell: an in-plane drift-diffusion current that flows between the gas | ceria chemical reaction site and the metal current collector, and a cross-plane current that flows between the two metal electrodes on the opposite side of the cell. By fitting the surface reaction constant $\tilde{k}_f^0$ to experimental electrode resistance values while fixing material properties such as bulk ionic and electronic equilibrium defect concentrations and mobilities, we are able to separate the electrode polarization into the surface reaction component and the in-plane electron drift-diffusion component. We show that for mixed conductors with a low electronic conductivity (a function of oxygen partial pressure) or a high surface reaction rate constant, the in-plane electron drift-diffusion resistance can become rate limiting in the electrode reaction.

4.1 Introduction

Mixed ionic and electronic conductors have received significant attention for their potential as fuel cell components, permeation membranes, oxygen storage capacitors, electrochemical sensors, etc. Electrical DC and AC conductivity measurements of the bulk focused mostly on separating the ionic and electronic contributions to the electrical conductivity as well as determining the dielectric and chemical capacitances. Physically derived one-dimensional models have aided in the interpretation of electrical conductivity data in the bulk and materials defect chemistry. On the other hand, investigations of interfaces in mixed conductors, specifically the gas | mixed conductor and the metal | mixed conductor interface, require a two-dimensional model to adequately describe the interplay of various physical phenomena due to their inherent spatial multidimensionality. For example, the electrochemical potential lines near the interface are expected to have a strong non-linear behavior. However, the majority of the work in the community employs the one-dimensional treatment [JM01], [JMP99] and only a handful of works attempted to scale up to two-dimensional models, [MLL07], [Fle04] and [AHW$^+$00]. In this chapter we develop a two-dimensional small bias model for a symmetric metal current collector | mixed conductor | metal current collector cell. In particular, we focus on the numerical analysis of the cross-plane electronic current that flows through the mixed conductor between patterned metal stripes on both side of the cell, and the in-plane electronic current that flows between the gas | mixed conductor interface and the metal. In order for an electrochemical reaction to occur on the gas | mixed conductor interface, electrons need to diffuse from the reaction site to the external circuit and viceversa. Such a step, termed in-plane electron drift-diffusion, could play a significant role in the interfacial behavior of mixed conductors, particularly for exhibiting a low bulk

Table 4.1: Data for the domain geometry and background doping

W_1	$1.5\ \mu m$
W_2	$2.5\ \mu m$
l_2	$500\ \mu m$
l_c	$10\ \mu m$
B	$3.47 \times 10^{+27} \frac{\#\text{particles}}{m^3}$

electronic conductivity.

For this study, we selected Pt | $Sm_{0.15}Ce_{0.85}O_{1.925}(SDC)$ | Pt as mixed oxygen ion and electron conductor model system. High oxygen ion conductivity of acceptor-doped ceria at intermediate temperatures $(500 - 700^oC)$ has attracted a great deal of interest in the SOFC community. In addition, under mildly reducing condition, doped ceria exhibits moderate electronic conductivity ($\approx 0.1 S/cm$ at 650^oC, $p_{O_2} = 10^{-25} atm$ [LH05]), making it attractive for fuel cell anode applications. Recent studies have also shown that when operating SOFCs on hydrocarbon gases a ceria-based anode is significantly less susceptible to carbon coking [PVG00].

Finally, insight into the in-plane electron diffusion path in ceria (the diffusion due to electrons injected at the gas | Ceria interface) could lead to improved designs of anode geometries and reduced interfacial resistance.

4.2 Background

The physical model, depicted in figure 2.1 (top), consists of a mixed oxygen ion and electron conductor (ceria) with patterned metal current collectors (Pt) on both sides placed in a uniform gas environment ($H_2 - H_2O -$ Ar mixture). The patterned metal current collectors permit the system to be reduced to a repeating cell (figure 2.1(bottom)) using mirror symmetry lines (Γ_1, Γ_2, Γ_3). The thickness of the cell is given by $2l_2 = 1mm$, while

the surface dimensions are $2W_1 \approx 3\mu m$, the width of the metal | ceria interface (Γ_4), and $2W_2 \approx 5\mu m$, the width of the gas | ceria interface (Γ_5) (figure 4.1 and Tab. 4.1). Two charge carriers species are considered: oxygen vacancies, denoted by the subscript "ion, and electrons, denoted by "eon. We solve the electrochemical potential and current of both charge carriers using a linear and time-independent model.

We assume that the gas | ceria interface is the prevailing surface active site facilitating the reaction between electrons and oxygen vacancies in the oxide and the gas phase species. In other words, the gas | metal | ceria triple-phase boundary interface is nonreacting. As we conjectured in chapter 2, mixed conductivity coupled with sufficient electrocatalytic activity allows electrochemical reactions to take place away from the triple-phase boundary. As a result, in the general 3D setting, the metal | gas | ceria interface, a 1D line, has substantially less area for reaction compared to the gas | ceria interface, a 2D area. We further treat the surface chemistry as one global reaction, and do not consider diffusion of adsorbed species on the surface. Combined with the final assumption that the metal | ceria interface is reversible to electrons, we are only considering two steps in the electrode reaction pathway: the surface reaction, and the electron drift-diffusion from the electroactive site to the metal current collector.

4.2.1 Value of the Polarization Resistance

To compute the electrode polarization resistance, let us first consider the relevant electrochemical currents that take place within our system. Due to the mixed conducting nature of ceria, there will be an inherent cross-plane electronic current, termed I_e^{CP}, that flows between the metal current collectors located on the opposite side of ceria (Figure 4.1). The surface reaction taking place on Γ_5 will simultaneously inject one oxygen vacancy and two

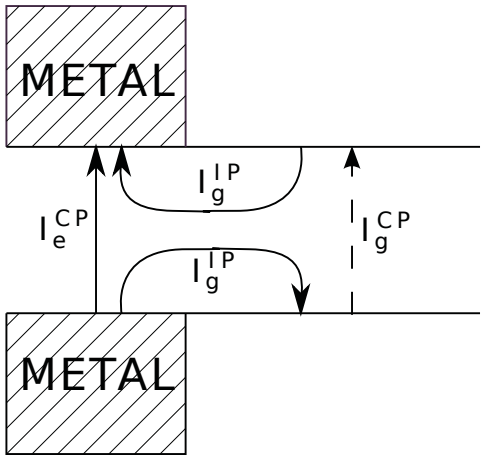

Figure 4.1: Various electronic and ionic current within the cell. The solid line indicates the electronic current and dashed line indicates the oxygen vacancy (ionic) current. The superscript IP refers to the in-plane current that flows between the gas | ceria chemical reaction site and the metal current collector, while "CP refers to the cross-plane current that flows between the metal current collectors located on the opposite side of ceria. The subscript g indicates that the current originates from the gas, while the subscript 'e indicates that it comes from the electrodes.

electrons into ceria. Two distinct currents result: the cross-plane ionic current I_g^{CP} that flows between the two sides of the cell, and the in-plane electron drift-diffusion current I_g^{IP} that flows between gas | ceria interface and the metal | ceria interface. By electroneutrality, $I_g^{CP} = I_g^{IP}$. We formally define these currents as follows:

$$I_e^{CP} = \int_{\Gamma_1} \mathbf{j}_{eon} \cdot \mathbf{n} \, \mathrm{d}x = \int_{\Gamma_4} \mathbf{j}_{eon} \cdot \mathbf{n} \, \mathrm{d}x, \tag{4.1a}$$

$$I_g^{IP} = \int_{\Gamma_5} \mathbf{j}_{eon} \cdot \mathbf{n} \, \mathrm{d}x = \int_{\varphi_e^S(\Gamma_5)} \mathbf{j}_{eon} \cdot \mathbf{n} \, \mathrm{d}x. \tag{4.1b}$$

Note that to obtain I_g^{IP}, we could integrate the current density either over Γ_5 or over $\varphi_e^S(\Gamma_5)$, which, as depicted figure 4.4, represents some fraction of Γ_4 accessed by the current injected from the gas | ceria interface. Direct comparison with the work of Jamnik and Maier [JM01] and Lai and Haile [LH05] leads to the following definitions of the bulk electronic resistance

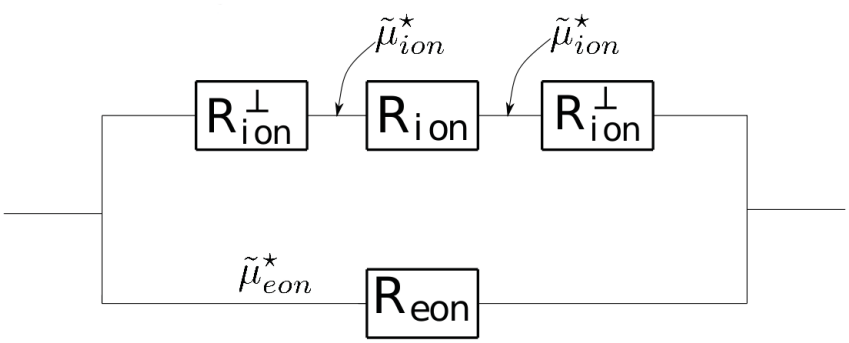

Figure 4.2: Simplified one-dimensional equivalents circuit employed by Lai and Haile [LH05], and Jamnik and Maier [JM01], where R_{eon} is the bulk electronic resistance, R_{ion} is the bulk ionic (oxygen vacancy) resistance, and $R^{\perp}_{ion}$ is the electrode polarization resistance normalized by the cell area. $\tilde{\mu}^{\star}_{ion}$ and $\tilde{\mu}^{\star}_{eon}$ are the electrochemical potential of oxygen vacancies and electrons, respectively.

R_{eon}, bulk ionic resistance R_{ion}, and the electrode polarization resistance normalized by the sample area $R^{\perp}_{ion}$:

$$R_{eon} = 2\frac{<\tilde{\mu}^{\star}_{eon}>_{\Gamma_4} - <\tilde{\mu}^{\star}_{eon}>_{\Gamma_1}}{j_e} = 2\frac{<\tilde{\mu}^{\star}_{eon}>_{\Gamma_4}}{j_e}, \tag{4.2a}$$

$$R_{ion} = 2\frac{<\tilde{\mu}^{\star}_{eon}>_{\Gamma_5} - <\tilde{\mu}^{\star}_{eon}>_{\Gamma_1}}{j_g} = 2\frac{<\tilde{\mu}^{\star}_{eon}>_{\Gamma_5}}{j_g}, \tag{4.2b}$$

$$R^{\perp}_{ion} = \frac{<\tilde{\mu}^{\star}_{eon}>_{\Gamma_4} - <\tilde{\mu}^{\star}_{ion}>_{\Gamma_5}}{j_g}, \tag{4.2c}$$

where $j_e = \dfrac{I^{CP}_e}{W_1 + W_2}$ and $j_g = \dfrac{I^{IP}_g}{W_1 + W_2}$ are the current densities averaged over the total sample area and where the $\star-$potentials, defined in chapter 2, are the electrochemical potentials divided by the elementary charge of the species under study. Our two-dimensional model allows us to distinguish among various contributions of $R^{\perp}_{ion}$. Two of them are particularly relevant. It is possible to separate $R^{\perp}_{ion}$ into a surface reaction resistance term

R_{surf} and in-plane electron drift-diffusion term R_{eon-DD}:

$$R_{surf} = \frac{< \tilde{\mu}^{\star}_{eon} >_{\Gamma_5} - < \tilde{\mu}^{\star}_{ion} >_{\Gamma_5}}{I_g} = \left(1 + \frac{\bar{n}}{4\bar{p}}\right) \frac{< n^{(1)} >_{\Gamma_5}}{j_g}, \tag{4.3a}$$

$$R_{eon-DD} = R^{\perp}_{ion} - R_{surf}, \tag{4.3b}$$

where R_{surf} corresponds to the electron-vacancy electrochemical potential difference at the gas | ceria interface, and R_{eon-DD} corresponds to the electron potential difference at the gas | ceria interface and at the metal | ceria interface. The resistance R_{surf} represents the resistance associated with the chemical transformation of electrons to vacancy at the gas | ceria chemical reaction site. Specifically, R_{surf} is due to the migration of oxygen vacancies from the bulk to the surface, and the subsequent chemical reactions that give rise to the electronic current. Finally, the drift-diffusion of the injected electrons from the reaction site to the metal current collector results in R_{eon-DD}.

Alternatively, we could also separate $R^{\perp}_{ion}$ into a "true" polarization term, R_{pol}, and a "deviation" term, R_{avg}, that results from averaging:

$$R_{pol} = \frac{< \tilde{\mu}^{\star}_{eon} >_{\varphi^S_e(\Gamma_5)} - < \tilde{\mu}^{\star}_{ion} >_{\Gamma_5}}{j_g}, \tag{4.4a}$$

$$R_{avg} = R^{\perp}_{ion} - R_{pol}. \tag{4.4b}$$

In (4.2) $R^{\perp}_{ion}$ is proportional to the difference of the electronic electrochemical potential averaged over the metal | ceria and averaged over gas | ceria interface. In (4.4), we define the R_{pol} by averaging only some portion of Γ_4 (rather than over the entire interface) by

considering the interface mapped by current lines injected from gas | ceria interface. R_{avg}, defined as the difference between the electrode polarization resistance and the true electrode polarization, is simply a spurious contribution due to averaging.

Knowledge of $n^{(1)}$ and $\tilde{\phi}^{(1)}$ is interesting, but appropriate integrals of $n^{(1)}$ and $\tilde{\phi}^{(1)}$ are worth more attention because they directly relate to measurable quantities. If we note that

$$\begin{aligned} j_g &= \frac{1}{(W_1+W_2)} D_{eon} e c_{eon}^{(0)} \int_{\Gamma_5} \left(\partial_{\tilde{y}} \tilde{\phi}^1 - \partial_{\tilde{y}} n^{(1)} \right) \mathrm{d}\tilde{x} \\ &= \frac{2W_2}{(W_1+W_2)} k_f \left(1 + \frac{c_{eon}^{(0)}}{4c_{ion}^{(0)}} \right) \tilde{p}_{H_2} < n^{(1)} >_{\Gamma_5}, \end{aligned} \tag{4.5}$$

then:

$$R_{ion}^{\perp} = \frac{W_1+W_2}{W_2} \frac{1}{2k_f \left(1 + \frac{c_{eon}^{(0)}}{4c_{ion}^{(0)}} \right)} \frac{< \tilde{\mu}_{eon}^{\star} >_{\Gamma_4} - < \tilde{\mu}_{ion}^{\star} >_{\Gamma_5}}{< n^{(1)} >_{\Gamma_5}}, \tag{4.6}$$

$$R_{pol} = \frac{W_1+W_2}{W_2} \frac{1}{2k_f \left(1 + \frac{c_{eon}^{(0)}}{4c_{ion}^{(0)}} \right)} \frac{< \tilde{\mu}_{eon}^{\star} >_{\varphi_e^S(\Gamma_5)} - < \tilde{\mu}_{ion}^{\star} >_{\Gamma_5}}{< n^{(1)} >_{\Gamma_5}}, \tag{4.7}$$

$$R_{surf} = \frac{W_1+W_2}{W_2} \frac{1}{2k_f}, \tag{4.8}$$

From the latter we can immediately notice that $R_{ion}^{\perp}$, R_{pol} and R_{surf} depend semi-linearly upon $\dfrac{W_1+W_2}{W_2} \dfrac{1}{D_{eon} e c_{eon}^{(0)}}$. Their ratios will be

$$f_{eon-DD} = \frac{< \tilde{\mu}_{eon}^{\star} >_{\varphi_e^S(\Gamma_5)} - < \tilde{\mu}_{ion}^{\star} >_{\Gamma_5}}{< \tilde{\mu}_{eon}^{\star} >_{\Gamma_4} - < \tilde{\mu}_{ion}^{\star} >_{\Gamma_5}}, \tag{4.9}$$

$$f_{surf} = \left(1 + \frac{\bar{n}}{4\bar{p}} \right) \frac{< n^{(1)} >_{\Gamma_5}}{< \tilde{\mu}_{eon}^{\star} >_{\Gamma_4} - < \tilde{\mu}_{ion}^{\star} >_{\Gamma_5}}. \tag{4.10}$$

4.3 Results

4.3.1 Potential Distributions and Surface Regions

Electrochemical equipotential lines for oxygen vacancies (figure 4.3, right) calculated using various values for the surface reaction rate constant, $\tilde{k}_f^0$ reveal that the potential and current distribution exhibit a relatively weak dependence on $\tilde{k}_f^0$. In general, oxygen vacancy equipotential lines bend as they approach the oxygen vacancy blocking metal | ceria interface Γ_4 from the bulk. On the other hand, equipotential lines for electrons (figure 4.3, left), display substantial deviations from those for oxygen vacancies, due to the presence of two current sources: cross-plane electronic current that flows between the current collectors on opposite side of the cell, and the in-plane electronic current injected by the surface reaction that flows between the metal | ceria (Γ_4) and the gas | ceria (Γ_5) interface. The electron potential distributions also depend strongly on the magnitude of $\tilde{k}_f^0$, indicating that electronic current injected from the surface reaction taking place at (Γ_5) strongly influence the electron penetration depth of the so-called "surface region."

The boundary of the surface region, given by the "trajectory" of electrons injected from the surface reaction site furthest from the metal current collector (the intersection of Γ_3 and Γ_5 in figure 2.1) is shown in figure 4.5. Physically, the surface zone can be viewed as a region where electronic current is entirely the in-plane electronic current (I_g^{IP}), rather than the cross-plane current I_e^{CP}. The surface region dimensions (figures 4.4, 4.5, 4.6) are specified by the largest length l, largest depth d, and the area A. All dimensions increases as a function of $\tilde{k}_f^0$. As the penetration area increases, the in-plane electrons will flow through a larger cross section of ceria, thereby reducing the diffusion resistance. It is interesting to note that the surface region approaches an asymptote for large $\tilde{k}_f^0$, suggesting that when

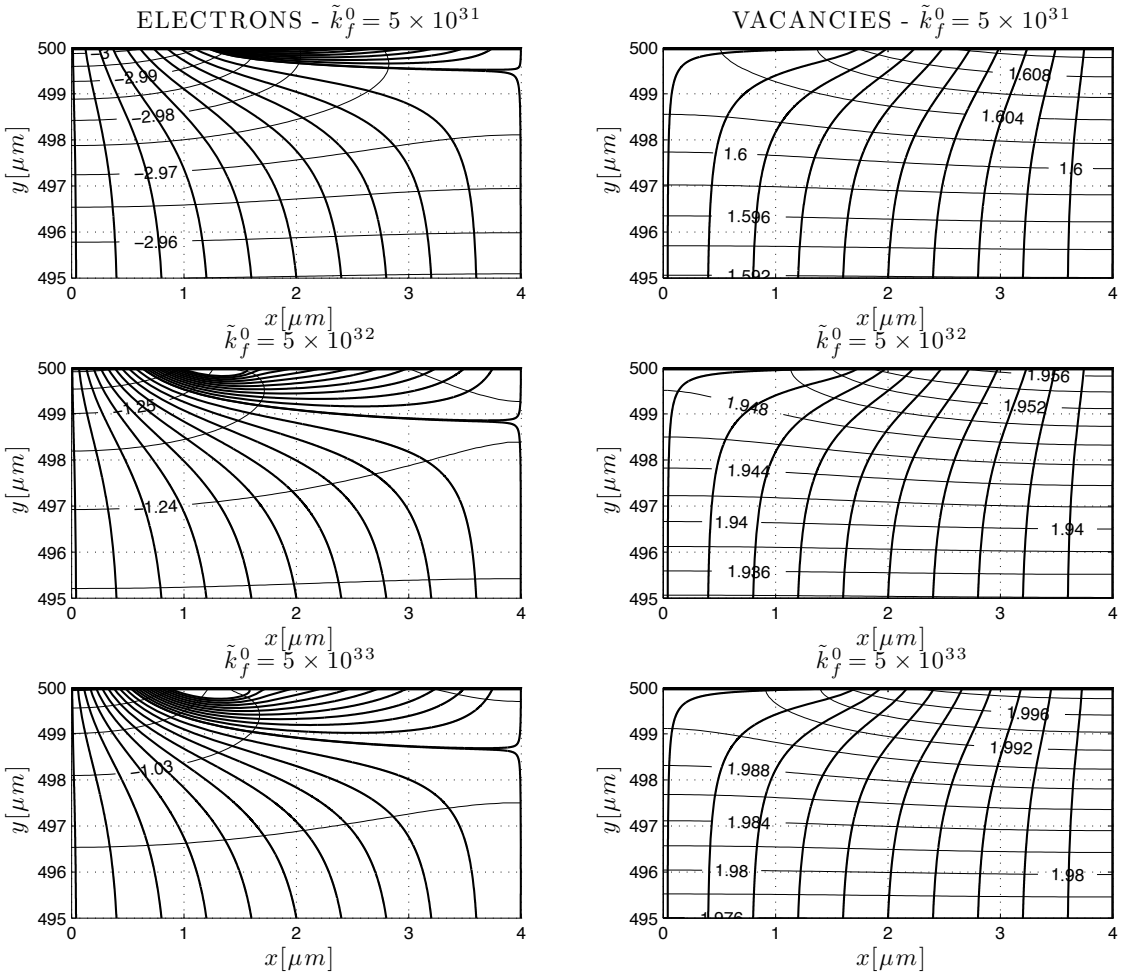

Figure 4.3: Electrochemical equipotential lines (left) and the corresponding current flow lines (right) computed for various surface reaction rate constants $\tilde{k}_f^0$ at 650^oC, $\tilde{p}_{O_2} = 4.1 \times 10^{-26}$. Only the portion of the domain close to the metal current collector is shown.

surface reactions are sufficiently fast, i.e., when they are in electrochemical equilibrium, the total electron injection current will be dominated by the in-plane electron diffusion resistance.

The surface region dimensions also grow with increasing $\tilde{p}_{O_2}$, though it is more pronounced for higher $\tilde{k}_f^0$. At lower $\tilde{k}_f^0$ values, the penetration area is virtually independent of $\tilde{p}_{O_2}$. The penetration depth is a function of the relative magnitude of I_e^{IP} to I_e^{CP}. As the

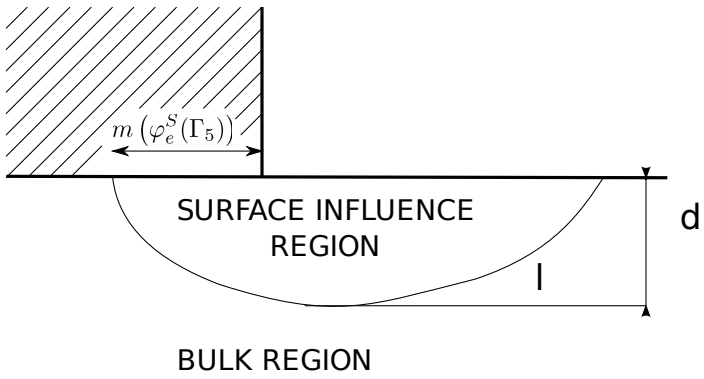

Figure 4.4: Illustration of the surface region, where the in-plane electronic drift-diffusion current prevails. The dimension of the region is indicated by the length l and depth d.The fraction of the metal | ceria interface mapped by the electronic current injected from gas | ceria interface is $\varphi_e^S(\Gamma_5)$.

ratio I_e^{IP}/I_e^{CP} grows, for instance, as a function of $\tilde{p}_{O_2}$, the penetration depth is expected to increase. In figure 4.6, we see that an increase in the penetration dimensions is indeed accompanied by an increase in I_e^{IP}/I_e^{CP}. We note that this relationship is counterintuitive, as the $\tilde{p}_{O_2}$ increases, the conductivity of electrons increases and, on the basis of mere common sense, one would expect that I_e^{IP}/I_e^{CP} decreases as well.

However, the tools developed so far, lead to a straightforward explanation of this behavior. We refer back to figures 4.1 and 4.2 and we shall analyze two cases, corresponding to high and low injection rate k_f:

1. For high k_f the resistivity of the bulk dominates over the polarization resistance, i.e., $R_ion \gg R_{ion}^{\perp}$, hence for high k_f the cross-plane gas current I_g^{CP} is set by R_ion and it is constant, independent of $\tilde{p}_{O_2}$. Yet I_e^{CP} is dependent on $\tilde{p}_{O_2}$, specifically, I_e^{CP} decreases with p_{O_2} because the electronic resistivity increases with p_{O_2}. Hence, the ratio $I_g^{CP}/I_e^{CP} = I_g^{IP}/I_e^{CP}$ increases with p_{O_2} with a 1/4 slope.

2. At low k_f, the polarization resistance dominates over the bulk resistance, i.e., $R_ion \gg$

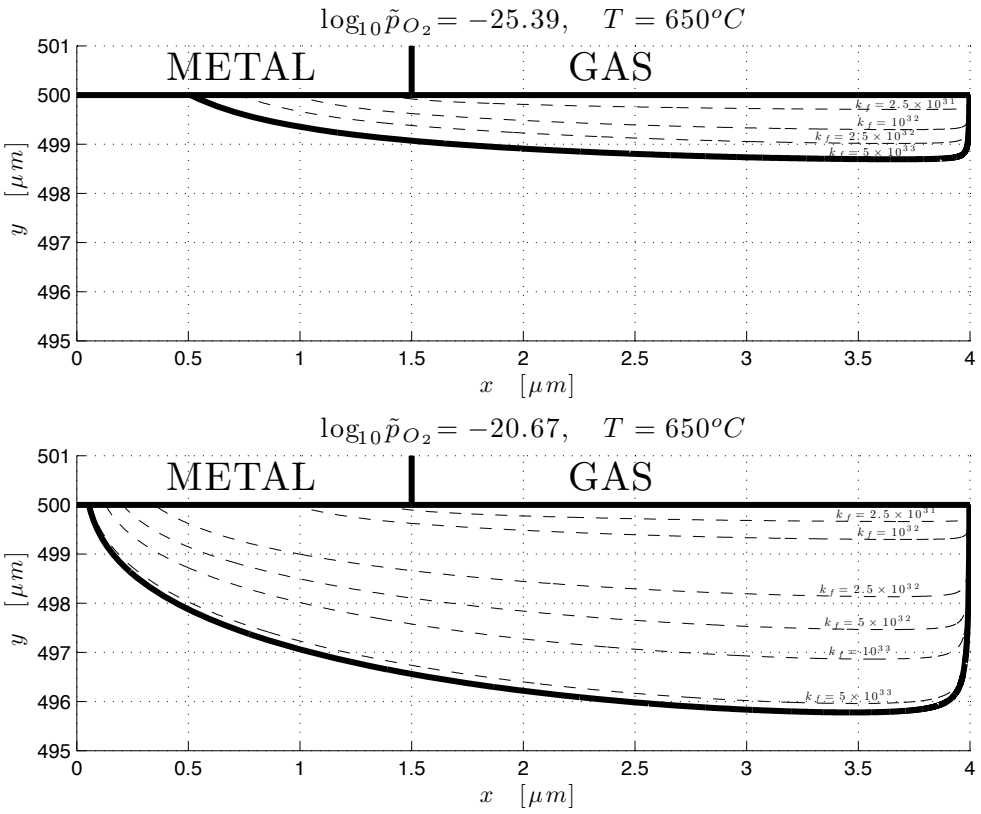

Figure 4.5: The boundary of the surface region, where electrons undergo in-plane drift-diffusion between the gas | ceria inteface and the metal current collectors, computed for various surface reaction rate constants $\tilde{k}_f^0$ at 650^oC, $\tilde{p}_{O_2} = 4.1 \times 10^{-26}$ (top) and $\tilde{p}_{O_2} = 2.1 \times 10^{-21}$ (bottom).

$R_{ion}^{\perp}$, and it is dependent upon $\tilde{p}_{O_2}$ to the 1/4. The same $\tilde{p}_{O_2}$ dependence occurs also for the electronic resistivity of the bulk, hence for very low k_f the I_g^{IP}/I_e^{CP} is $\tilde{p}_{O_2}$ independent.

4.3.2 Electrode Polarization Resistance

It is clearly shown in (4.4) that the electrode polarization resistance, $R_{ion}^{\perp}$, can be expressed as a sum of the true polarization term R_{pol} and a deviation term R_{avg} that results from averaging the electrochemical potential of electrons across the entire metal | ceria interface Γ_4 rather than just the region accessed by the in-plane electronic current $\varphi_e^S(\Gamma_5)$ (figure 4.4).

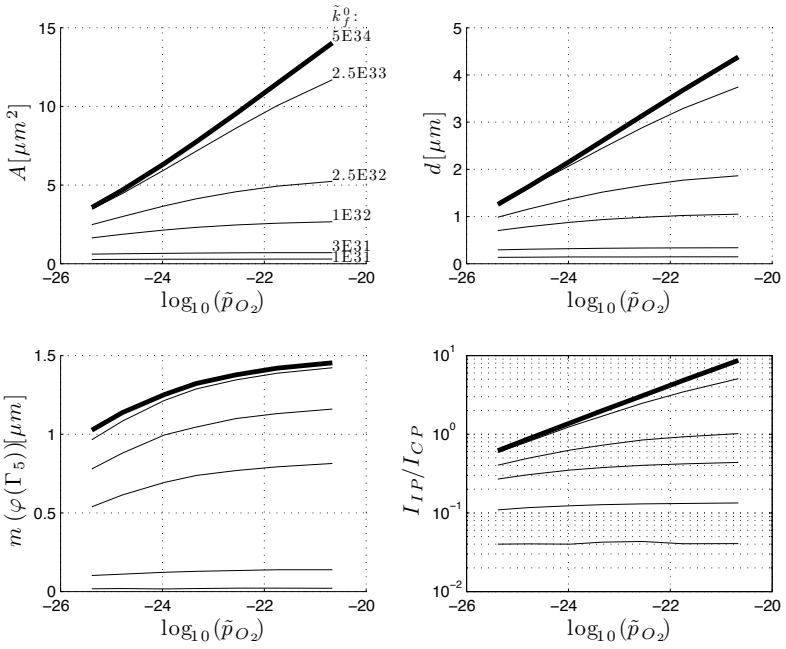

Figure 4.6: Dimensions of the surface region as a function of $\tilde{p}_{O_2}$ and $\tilde{k}_f^{(0)}$ at 650^oC.

We examine the extent of deviation of the $R_{ion}^{\perp}$ from R_{pol} by computing:

$$f_{pol} = \frac{R_{pol}}{R_{ion}^{\perp}} \tag{4.11}$$

Under a variety of conditions, f_{pol} is very close to unity (figure 4.8, top), indicating that the deviation term is quite small compared to the true polarization resistance. For the remainder of the thesis we will approximate $R_{pol} = R_{ion}^{\perp}$.

4.3.3 Electron Diffusion Resistance

In equation (4.8), the total electrode polarization resistance, $R_{ion}^{\perp}$, is expressed as a sum of a surface reaction resistance term, R_{surf}, and an in-plane electron diffusion resistance term, R_{eon-DD}. Under the moderately reducing $\tilde{p}_{O_2}$ regime where the electron carrier

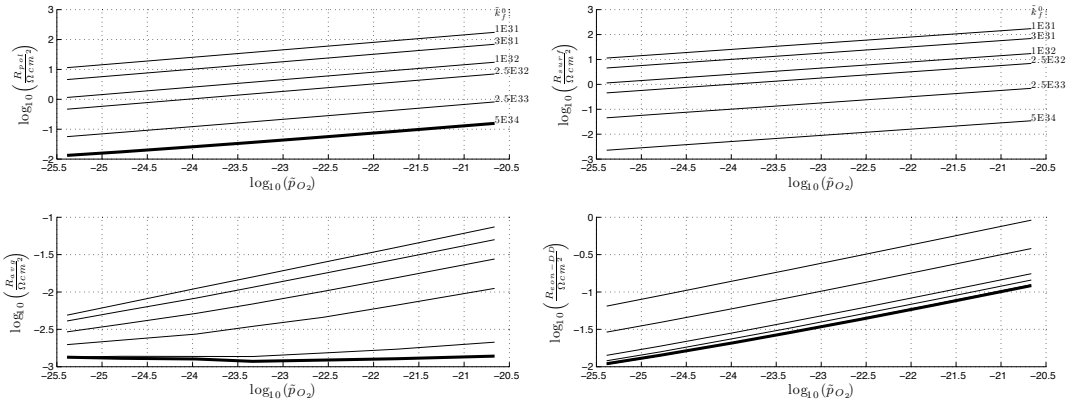

(a) Absolute value of the true polarization resistance R_{pol} (top) and the deviation term R_{avg} (bottom) as a function of p_{O_2} and $\tilde{k}_f^{(0)}$ at 650^oC.

(b) Absolute value of the surface reaction resistance R_{surf} (top) and the electron drift-diffusion resistance R_{eon-DD} as a function of p_{O_2} and $\tilde{k}_f^{(0)}$ at 650^oC.

Figure 4.7: The values of the various contributions of the polarization resistance as a function of partial pressure of oxygen and injection rate.

concentration is negligible compared to the extrinsic oxygen vacancies formed by acceptor doping, R_{eon-DD} is proportional to approximately $\tilde{p}_{O_2}^{1/4}$ (figure 4.7(b), bottom), following the same $\tilde{p}_{O_2}$ dependence as bulk electronic resistivity. As for R_{surf}, it is also proportional to $\tilde{p}_{O_2}^{1/4}$ as a result of our choice of β (figure 4.7(b), top). Turning to the dependence on $\tilde{k}_f^0$, we observe that both R_{surf} and R_{eon-DD} decrease with increasing $\tilde{k}_f^0$. However, a significant difference between R_{eon-DD} and R_{surf} is that, in a log-log plot the former approaches an asymptotic value as a function of $\tilde{k}_f^0$, whereas the latter does not. This interesting behavior of R_{eon-DD} is directly related with the asymptotic behavior of the the penetration depth of electrons injected from Γ_5 to Γ_4 (and vice versa) as a function of $\tilde{k}_f^0$ (figure 4.5). To help us examine I_g^{IP}, we further define fractional surface reaction resistance and fractional electron drift-diffusion as:

$$f_{surf} = \frac{R_{surf}}{R_{ion}^{\perp}} \tag{4.12a}$$

$$f_{eon-DD} = 1 - f_{surf} \tag{4.12b}$$

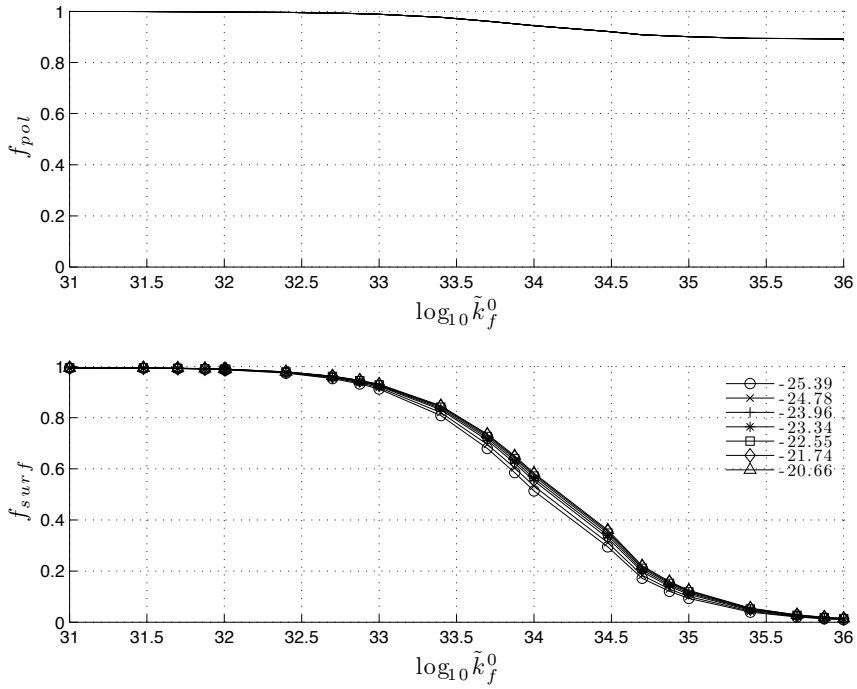

Figure 4.8: Fractional true polarization resistance (top) and fractional surface reaction resistance (bottom) as a function of $\tilde{k}_f^{(0)}$ at 650^oC, parametrized with respect to $\log_{10}\tilde{p}_{O_2}$.

Plotting f_{surf} as a function of $\tilde{k}_f^0$ (figure 4.8, bottom) reveals that when the surface reaction is very fast, or conversely when $\tilde{k}_f^0$ is large, f_{surf} approaches zero and the polarization resistance $R_{ion}^{\perp}$ is dominated by drift-diffusion R_{eon-DD}. On the other hand, when the surface reaction is slow, f_{surf} approaches unity and $R_{ion}^{\perp}$ is dominated by R_{surf}, as we would expect. When considering only material property dependencies (i.e., neglecting $\tilde{p}_{O_2}$, T, and sample geometry), R_{surf} is only a function of $\tilde{k}_f^0$ whereas R_{eon-DD} is a function of both $\tilde{k}_f^0$ and σ_{eon}. As $\tilde{k}_f^0$ tends toward infinity, R_{surf} approaches zero and R_{eon-DD} approaches an asymptotic limit that is a function of only σ_{eon}. In other words, as the surface reaction resistance term becomes negligible, electron carrier concentration and mobility alone determines the penetration dimensions and therefore $R_{ion}^{\perp}$. The condition under which f_{surf} approaches zero corresponds to the physical case where the electrode reaction

is limited by the rate in which the electrons migrate from the gas | ceria reaction site to the metal rather than the rate of surface reaction. Generally speaking, for a wide-bandgap mixed conductor exhibiting a low or moderate electronic conductivity and high $\tilde{k}_f^0$, such as ceria, in-plane electron drift-diffusion cannot be neglected. Accordingly, the electron diffusion length (the separation between the metal stripes in figure 2.1 top) needs to be tuned in order to minimize the electrode polarization resistance.

4.3.4 Topological Considerations

There are two degrees of freedom in the metal current collector topology: the metal stripe width ($2W_1$) and the intermetal distance ($2W_2$). Figure 4.9 shows parametric plots of the the fractional surface resistance (top row) and the total electrode polarization resistance (normalized for the total sample area) (middle row) and as a function of $W_1, \frac{W_2}{W_1}$, and $\tilde{k}_f^0$ at select temperatures and $\tilde{p}_{O_2}$. We observe the general trend that increasing $\frac{W_2}{W_1}$ (gas | ceria interface to metal | ceria interface ratio) leads to a reduction in the polarization resistance. Specifically, under the conditions that the fractional surface reaction resistance is greater than 0.99, we observe a linear decrease in the polarization resistance with increasing $\frac{W_2}{W_1}$. When the electron drift-diffusion resistance is negligible, the current density of electrons injected from Γ_5 is essentially uniform as a function of the position (and distance to the metal), and thus the fraction of area available for electrochemical surface reaction, given by $f = \frac{W_2}{W_1 + W_2}$, determines the polarization resistance. Figure 4.9 (bottom row) shows the polarization resistance normalized by the gas | ceria interface area and confirms that the normalized resistance remains relatively constant as long as the electron diffusion fractional resistance is negligible. However, as the fractional surface resistance decreases (due to an increase in $\tilde{k}_f^0$, for instance), electrochemical surface reactions taking place closer to

the metal will inject a larger current into the oxide. For example, at $\tilde{k}_f^0 = 7.5 \times 10^{33}$, $\tilde{p}_{O_2} = 4.1 \times 10^{-26}$ and $T = 650^oC$, a significant nonlinearity as well as a distinct minima in the polarization resistance as a function of W_1 and W_2 (figure 4.9 is observed (top right)). Furthermore, figure 4.9 (lower right) shows the polarization resistance normalized for the gas | ceria interface area begins to deviate from the constant values, confirming that parts of the interface are becoming less active due to increased electron diffusion resistance at spatial positions further away from the metal current collector.

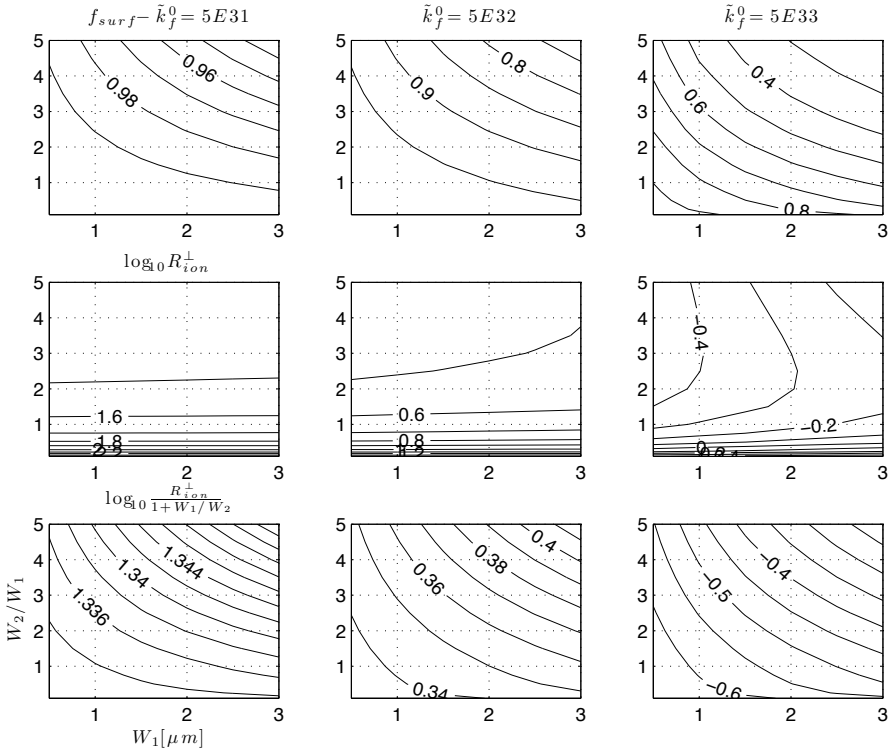

Figure 4.9: Parametric plots of the fractional surface reaction resistance (top row), the electrode polarization resistance $R_{ion}^{\perp}$ normalized for the sum of the metal | ceria and gas | ceria interfacial area (middle row), and normalized for the gas | ceria interfacial area (bottom row), as a function of W_2/W_1 and W_1.

In general, when the surface reaction rate constant is small or when the bulk electronic conductivity is large, one should increase f in order to increase the area available for surface reactions, as long as the electron diffusion fractional resistance is kept low. On the other

hand, when the surface rate constant is large or when the bulk electronic conductivity is small, one needs to find an intermediate f in order to balance the area available for surface reaction and the in-plane electron diffusion distance.

4.3.5 Comparison to Experimental Results

We fit the polarization resistance data obtained by Lai and Haile [LH05] using AC impedance spectroscopy on a cell geometry consistent with our model description. The experimental result was based on a (porous Pt) | SDC | (porous Pt) cell in an atmosphere consisting of H_2, H_2O and Ar. We approximated the porous Pt electrode as line patterns by estimating W_1 and W_2 based on the actual pore size and interpore distance. We fit the polarization resistance using $\tilde{k}_f^0$ as the only parameter and fixed dopant and equilibrium carrier concentration according to the values obtained in the experiment. It should be noted that all parameters were obtained from the same electrochemical cell by Lai and Haile and are highly self-consistent. The fitting (figure 4.10) shows computed $\tilde{k}_f^0$ corresponding to the polarization resistance obtained experimentally. Because we phenomenologically set the $\tilde{p}_{O_2}$ dependence of R_{surf} to 1/4 so that $R_{ion}^{\perp}$ would exhibit the same $\tilde{p}_{O_2}$ as the experimental data (and the other component of the polarization resistance, R_{eon-DD}, is also proportional to $\tilde{p}_{O_2}^{1/4}$ in the same way as the bulk electronic conductivity), obtaining the same dependence in $\tilde{p}_{O_2}$ for the experimental and fitted value is automatic.

Taking the fitted $\tilde{k}_f^0$ values, we can further separate the polarization resistance into the surface reaction and the electron drift-diffusion contributions. At the temperatures and $\tilde{p}_{O_2}$ examined, the computed f_{surf} (figure 4.12) is close to unity (for $W_1 \approx 1.5\mu m$ and $W_2/W_1 \approx 1.67$), implying that the surface reaction step is the rate-limiting step. To examine the dependence of f_{surf} on the geometric parameter (which directly influences the

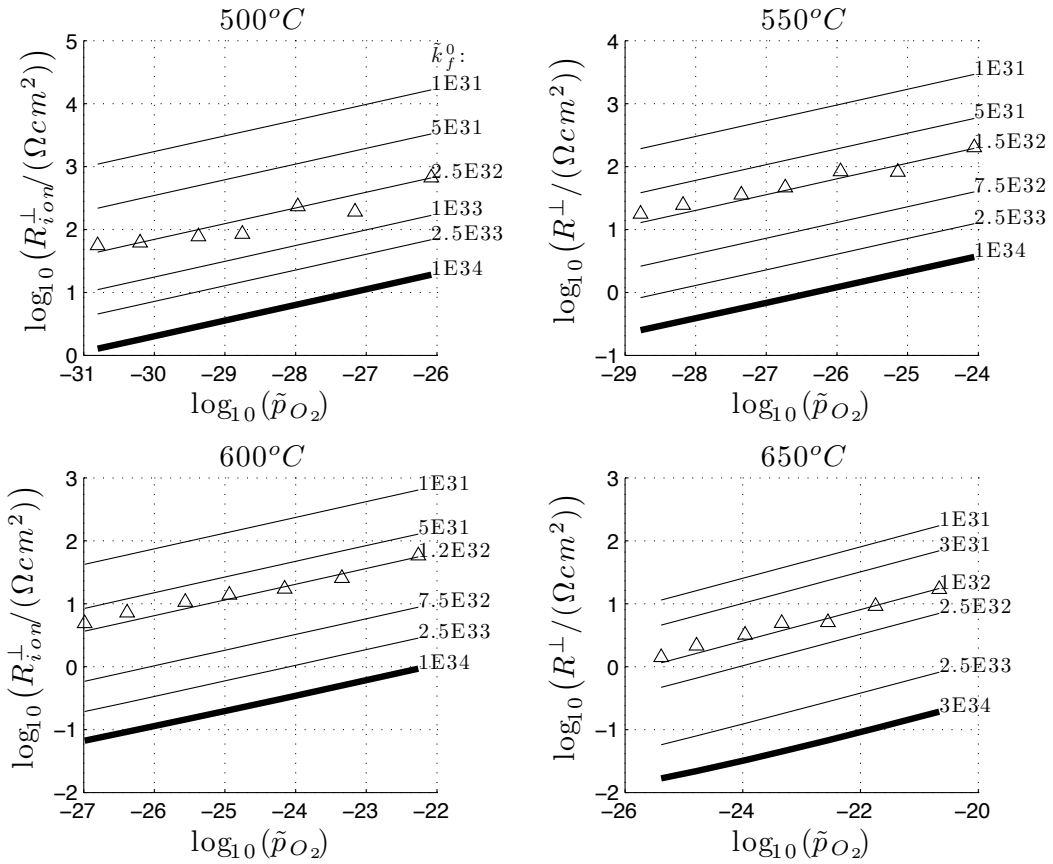

Figure 4.10: Electrode polarization resistance , $R_{ion}^{\perp}$, plotted as a function of $\tilde{p}_{O_2}$ and $\tilde{k}_f^{(0)}$ at 500^oC, 550^oC, 600^oC and 650^oC. The open triangles show the experimental data obtained in ref [LH08].

electron diffusion length and area of the gas | ceria interface), we fit $\tilde{k}_f^0$ to the polarization resistances while varying W_1 and W_2 . The parametric plot (figure 4.12) again shows that f_{surf} is close to unity for a wide range of W_1, W_2, T and $\tilde{p}_{O_2}$. However, we do observe the general trend that f_{surf} decreases slightly with increasing W_1 and decreasing W_2/W_1. Decreasing W_2/W_1 (at a fixed W_1) reduces the electron diffusion length and reduces the area of the gas | ceria interface, and $\tilde{k}_f^0$ needs to be increased in order to fit to the observed polarization resistance (figure 4.11). For the same reason discussed in Section 4.3, this leads to a decrease in f_{surf}. On the other hand, increasing W_1 (at a fixed W_2/W_1) increases the electron diffusion length without affecting the available reaction area. As a result, increased

R_{eon-DD} leads to an decrease in f_{surf}.

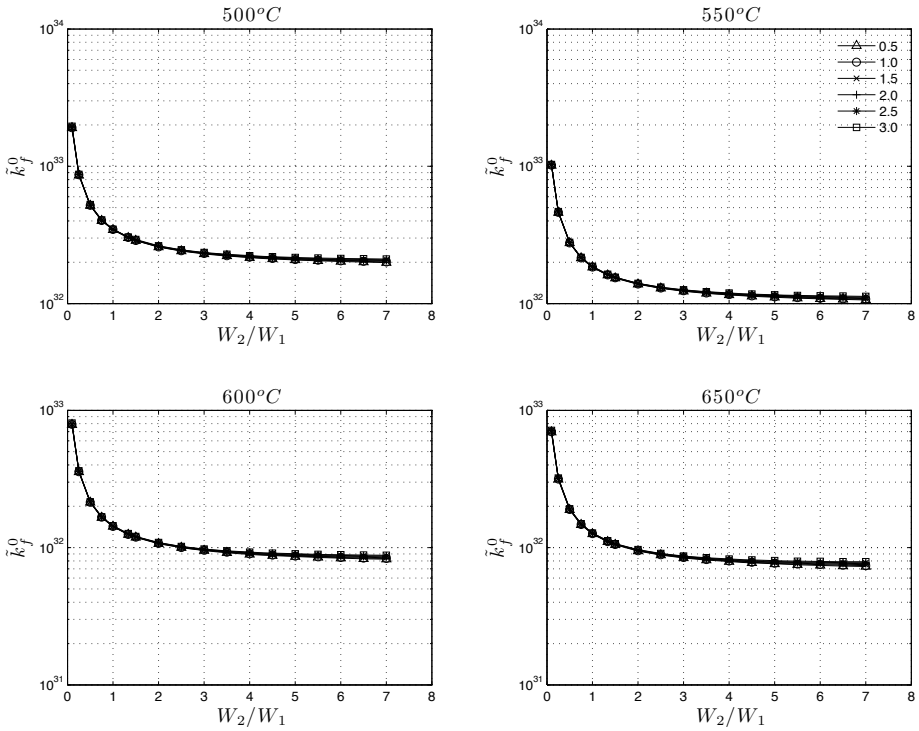

Figure 4.11: If we assume that that our initial choice of W_1 and W_2 is not the correct one, it is legitimate to ask the following question: "which $\tilde{k}_f^0$ fit the ASRP data best?". We find that the fitting depends only on the ratio $\frac{W_2}{W_1}$ and not on the chosen value of W_1, the label indicates that $W_1 = 0.5, 1.0, 1.5, \ldots, 3.0\mu m$.

Approximating a gridlike porous metal on ceria as line patterns could lead to some errors, such as overestimating the fraction of gas | ceria interface and the electron diffusion length. However, given that the computed f_{surf} is far from 0.5 (the case where surface reaction and electron drift-diffusion are equally colimiting) for a wide range of W_1 and W_2, these errors will not change the f_{surf} significantly and will only rescale the magnitude of the resistances slightly. Therefore, based on the numerical analysis in this work, the electrode reaction in (porous Pt) | SDC | (porous Pt) cell in H_2, H_2O and Ar is likely to be surface reaction limited.

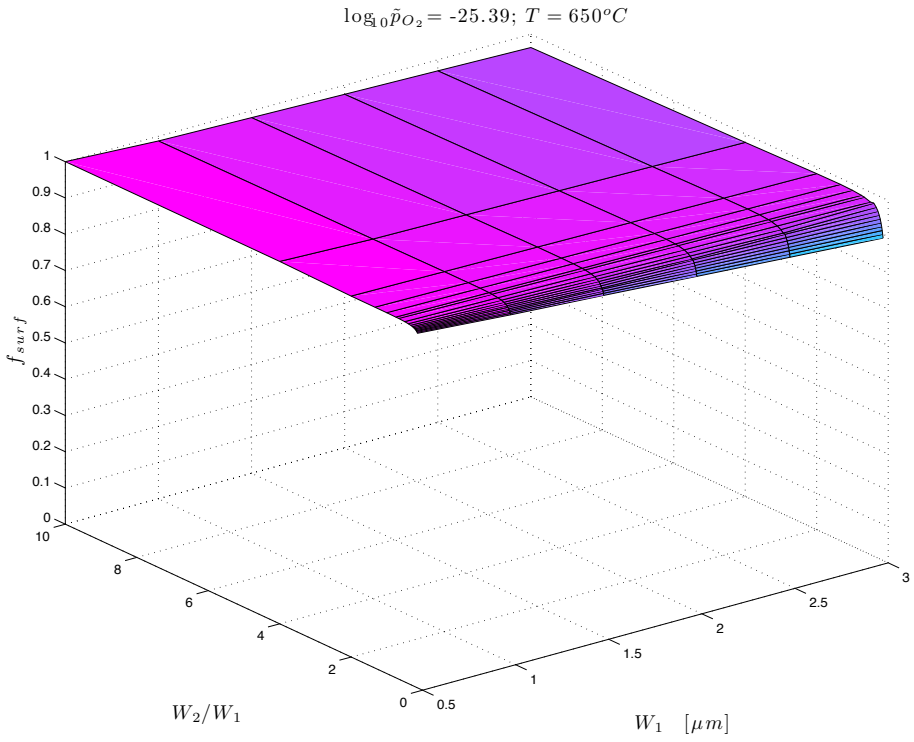

Figure 4.12: Fractional surface reaction resistance, obtained after fitting $\tilde{k}_f^{(0)}$ to the experimental data in the paper of Lai and Haile [LH05], and plotted as a function of p_{O_2}, $\tilde{k}_f^0$ at 650^oC. It is noticeable that all fittings give $f_{surf} \approx 1$.

Finally, it should be noted that our assumption that the electron mobility and equilibrium carrier concentration is the same in the near-surface region and in the bulk directly determines the contribution of the in-plane electron drift-diffusion resistance to the electrode polarization resistance. Since electron penetration depth is predicted to be on the order of $1\mu m$, dopant segregation and presence of blocking grain boundaries near the surface could, in principle, affect the local electron mobility and concentration.

4.4 Conclusions

A two-dimensional electrochemical model has been developed for mixed conductors with patterned metal current collectors. Numerical simulation for a Pt | SDC | Pt in reducing atmosphere revealed a strong nonlinearity in the electronic potential and current distributions near the surface. In particular, we show that the in-plane electron drift-diffusion current plays a crucial role in determining the surface electrochemical behavior. Under certain conditions, the in-plane electron drift-diffusion resistance could dominate the electrode resistance.

Chapter 5

Computation of Impedance Spectra in Two-Dimensional Mixed Conductors

5.1 Introduction

The study of the alternate current properties of Mixed Ionic and Electronic Conductors (MIEC) aides in understanding many of the physical chemical phenomena related to the behavior of defects, electrochemistry and interfaces. As we have shown in Chapter 1, a technique frequently used to probe the interplay between these processes is impedance spectroscopy (IS). IS consists in injecting a "small" sinusoidal current into an electrochemical sample, a fuel cell for example, which is initially under steady-state conditions. This perturbation in turn induces a small sinusoidal and dephased perturbation of the voltage. From the measurements of voltage and current over a wide set of frequencies, one can compute the complex impedance of the system. When an IS experiment is compared against a suitable model, impedance spectroscopy helps understand the linear physics of electro-active system.

The tools used to deconvolute impedance spectra and relate them to physical-chemical quantities are usually limited to one-dimensional equivalent circuits [JM01] [Jam03]. Even

though the 1D approach is very useful because it enables the comparison of different processes, it sometimes fails to help satisfactorily interpret physical chemical phenomena that extend to several dimensions. Only a handful of works attempted to scale up to two dimensions, and they generally have been constrained to the steady-state setting [MLL07] [Fle04] [AHW$^+$00].

In this chapter of the thesis we develop a method for the computation of impedance spectra for highly doped mixed conductors in a 2D setting under geometrically symmetric conditions. Here we will consider essentially the same system of Chapter 4. The system studied was chosen so that it is not too cumbersome algebraically and readily relatable to well defined experiments. However the methodology is very general and it can be easily extended to 3D, to dissymmetric systems under non-zero bias and to complex chemical boundary conditions.

The chapter proceeds as follows: we first develop a model for impedance spectroscopy and determine the impedance equations [Mac73], then we compare our results to experimental data, finally we study the influence of parameter variation on the IS: the thickness of the sample, the rates of the chemical reactions at the exposed MIEC surface and the diffusivity profiles.

As shown in chapter 2, after non-dimensionalization of the full drift-diffusion equations, we find that the ratio between the Debye length and the characteristic length scale of the material is remarkably large, hence we singularly perturb the governing equations and we deduce that electroneutrality is satisfied for a large portion of the sample. Then we apply a small sinusoidal perturbation to the potential, which mathematically translates into a regular perturbation of the equations; after formal algebraic manipulations we collect first-order terms and deduce two complex and linear partial differential equations in 2D space

and time. Thanks to linearity, the Fourier transformation of these equations and their boundary conditions leads to the determination of the complex impedance spectroscopy equations which we solve in 2D space for the frequencies of interest.

We verify our numerical results against experiments that are relevant for fuel cell applications. In particular, we study the case of a Samarium Doped Ceria (SDC) sample, immersed in a uniform atmosphere of argon, hydrogen and water vapor. The sample is symmetric and reversible and has been the subject of extensive research [CLH08], [LH08], [LH05]. We find excellent agreement between the computed impedance spectra and experimental data. This shows that this framework could help address a number of important fundamental physical/chemical issues in mixed conductors.

5.2 System under Study

The physical system under study is a two-dimensional assembly which consists of a mixed oxygen ion and electron conductor slab of thickness $2l_2$ sandwiched between two identical patterned metal current collectors, figure 2.1. The patterned collectors are repeated and symmetrical with respect to the centerline Γ_1. Hence the system can be reduced to a repeating cell using the mirror symmetry lines Γ_1, Γ_2 and Γ_3. All sides of the sample are placed in a uniform gas environment. Two charge-carrying species are considered: oxygen vacancies, denoted by the subscript ion, and electrons, denoted by "eon".

The framework we propose is very broad in scope, however we specialize our study to Samarium Doped Ceria (SDC). We chose to to analyze SCP because doped ceria is a class of materials that has recently gained prominent relevance in fuel cell technology [PVG00] [Tro01]. We suppose that the uniform gas environment consists of a mixture of hydrogen and water vapor and we solve the electrochemical potential and current of both charge

carriers using a linear and time-independent model developed via perturbation techniques and Fourier transformation. We mainly compare our computational work to the data of Lai et al. [LH08] but we also leverage on some results of Chueh et al. [CLH08] to justify the boundary conditions. We focus on studying SDC-15 (15% samarium doping), where the background dopant particles per unit volume, B, is well defined and reported in Tab. 4.1.

The surface dimensions are kept constant: the width of the metal | ceria interface (Γ_4) is $2W_1 = 3\mu m$ and the width of the gas | ceria interface (Γ_5) is $2W_2 = 5\mu m$. The thickness of the MIEC is set to be $2l_2 = 1mm$, unless otherwise specified. Due to high electronic mobility in the metal, the thickness of the metal stripe does not affect the calculation, and thus the thickness of the electrolyte is, in effect, the thickness of the cell. Hence we assume that the characteristic length scale of the sample under study is $l_c = 10\mu m$. The data mentioned above is summarized in Tab. 4.1.

The assumptions of the model are rather standard for MIEC. We set that the gas | metal | ceria interface, or triple-phase boundary, has a negligible contribution compared to surface reactions [ALS96]. We further treat the surface chemistry as one global reaction, and do not consider diffusion of adsorbed species on the surface [KZG05]. Combined with the final assumption that the metal | ceria interface is reversible to electrons, i.e., an Ohmic condition [MLL07], as in Chapter 4 we are considering only two steps in the electrode reaction pathway: surface reactions at the active site of the SDC | Gas interface and electron drift-diffusion from the active site to the metal current collector both along the SDC | gas interface and through the SDC bulk.

We indicate the equilibrium quantities, such as electron and oxygen vacancy concentration, with the superscript (0). The equilibrium concentrations of vacancies and electrons are given respectively by $c_{ion}^{(0)} \approx B/2$ and $c_{eon}^{(0)} \approx B\frac{\sqrt{2Kr}}{[Sm'_{Ce}]^{1.5}\tilde{p}_{O_2}^{0.25}}$. Finally we assume that the

mobilities u of all species are given in Tab. 2.1, where the values are derived from Lai et al. [LH08].

5.3 Results

5.3.1 Comparison with Experiments

The electron electrochemical potential drop across the sample, i.e., the electron electrochemical potential difference between the top and bottom electrodes (Γ_4 and its symmetric reflection), is given by the following expression:

$$\hat{V}^{(1)} = 2U_T \left[< \left(\hat{\mu}_e^{(1)}\right)^\star >_{\Gamma_4} - < \left(\hat{\mu}_e^{(1)}\right)^\star >_{\Gamma_1} \right] \tag{5.1}$$

where $< a >_\Lambda$ indicates the average of the quantity a over the set Λ. At first order the $\star$-electrochemical potential is given by $\left(\hat{\mu}_e^{(1)}\right)^\star = \hat{\phi}^{(1)} - \hat{n}^{(1)}$. The electric current density at the two ends of the circuit is:

$$\hat{j}^{(1)} = \frac{D_{eon} e c_{eon}^{(0)} \displaystyle\int_{\Gamma_4} \nabla_{\tilde{x}} \frac{\tilde{\mu}_{eon}^{(1)}}{k_b T} \cdot \mathbf{e}_y \, \mathrm{d}\tilde{x}}{(W_1 + W_2)\, l_c} \tag{5.2}$$

Hence, the 2D impedance is given by the expression:

$$Z_{2D}(\omega, \tilde{p}_{O_2}, T) = \hat{V}^{(1)} / \hat{j}^{(1)}. \tag{5.3}$$

We define the error of the 2D impedance Z_{2D} with respect to experimental impedance Z_{1D}

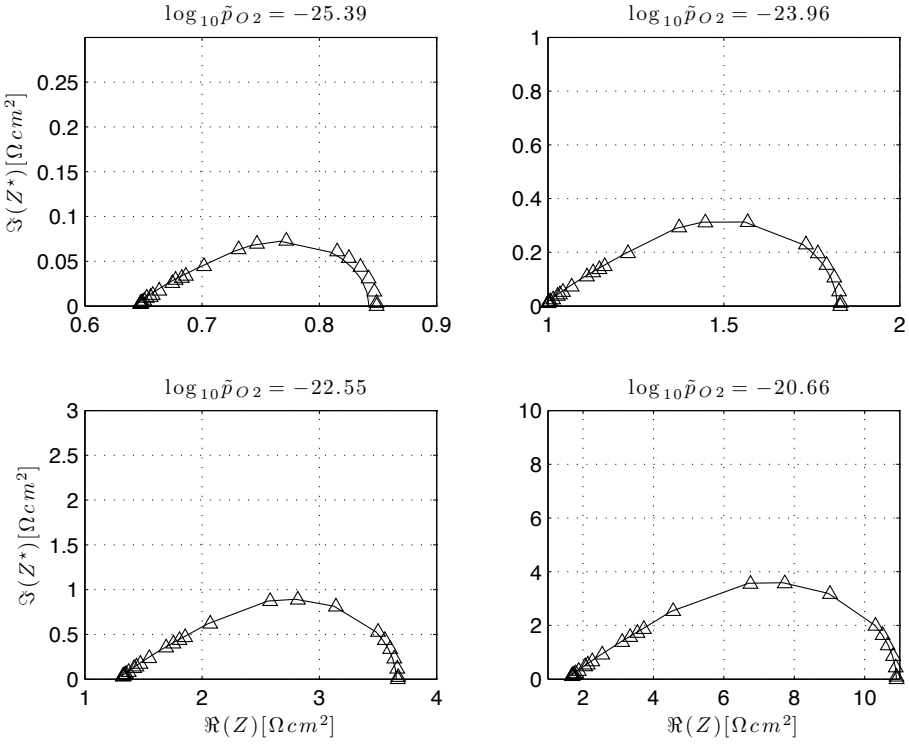

Figure 5.1: The triangle indicates fitted computations while the solid line is the experimental value. The results are presented at 650^oC varying the $\tilde{p}_{O_2}$ partial pressure from [LH05].

Table 5.1: Fitted values of $\tilde{k}_f^0 = A\tilde{p}_{O_2}^{\alpha}$, 95% confidence interval

$T\ [^oC]$	$\log_{10}\bar{A}$	$\log_{10}\varepsilon_A$	$\bar{\alpha}$	ε_α	R^2	σ
500	32.48	0.150	0.05349	0.1655	-0.0439	0.1577
550	32.10	0.045	0.04160	0.0482	0.7622	0.04589
600	32.02	0.055	0.06674	0.0637	0.5378	0.06067
650	31.95	0.055	0.05596	0.0623	0.4981	0.05938

spectra (3.23) as follows:

$$\varepsilon_F(\omega, \hat{p}_{O_2}, T) = \left| 1 - \frac{Z_{2D}(\omega, \tilde{p}_{O_2}, T)}{Z_{1D}(\omega, \tilde{p}_{O_2}, T)} \right|. \tag{5.4}$$

For every data point, uniquely defined by the couple $(\tilde{p}_{O_2}, T)$, we fit the 2D data against the measured 1D equivalent circuit data in [LH05] by minimizing $\varepsilon_F(\omega, \tilde{p}_{O_2}, T)$ with respect to the surface reaction constant $\tilde{k}_f^0 = A\tilde{p}_{O_2}^{\alpha}$, which is a function of both O_2 partial pressure and temperature. We remark that $\tilde{k}_f^0$ is the sole parameter we allow to vary in this procedure and all necessary data are obtained from the literature and presented in Tab. 5.1. With only one parameter variation, we obtained excellent agreement between experimental results and 2D calculations, i.e., $\varepsilon_F(\omega, \hat{p}_{O_2}, T) < 2\%$. As an example, 2D results at four different oxygen partial pressures and at 650°C are shown in figure 5.1. We computed the $\tilde{k}_f^0$ by minimizing the ε_F for a total of 28 cases (7 pressures times 4 temperature). We report in Tab. 5.1 the results of linear regression of these minimizing values (each line is derived by keeping the temperature fixed and varying $\tilde{p}_{O_2}$). We also write in Tab. 5.1, the 95% confidence intervals for the fitting of A, i.e., $A \approx \bar{A} \pm \varepsilon_A$, and α, i.e., $\alpha = \bar{\alpha} \pm \varepsilon_\alpha$; we finally report the root mean square error σ and the adjusted R-squared [DS98] (regarding the latter, a value close to unity indicates a perfect fit while negative values indicate poor data correlation). Directly from analysis of Tab. 5.1 we deduce that $\tilde{k}_f^0$ fitting to a straight line is reasonable for "high" temperatures ($T \geq 550^o C$). We note that $\tilde{k}_f^0$ is temperature dependent via $\bar{A}$ ($\bar{A}$ decreases with T). Furthermore $\tilde{k}_f^0$ is slightly pressure dependent via the coefficient α; the average value of $\bar{\alpha} \approx 0.05 \geq 0$. However, the error is of the same order of the slope. Hence, the total rate of reaction is very likely to be $\dot{\omega}_{eon,S} \propto \tilde{p}_{O_2}^{-1/4+\beta}$ where β is somewhere in the set

$[0, 0.1]$, most likely equal to 0.05.

5.3.2 The Polarization Resistance in Frequency Space

One of the goals of fuel cell science is to understand and possibly reduce the polarization resistance, i.e., that portion of the resistance due to electric field effects at interfaces. For that purpose it is key to identify and understand the main processes that intervene in the definition of this quantity. Specifically, the area specific polarization resistance for our system is defined as [CWHG09]

$$Z_{ion}^{\perp} = U_T \frac{< \hat{\mu}_{ion}^{\star} >_{\Gamma_5} - < \hat{\mu}_{eon}^{\star} >_{\Gamma_4}}{\hat{j}_{IP}^{(1)}}, \tag{5.5}$$

where $\hat{j}_{IP}^{(1)} = \dfrac{1}{W_1 + W_2} \displaystyle\int_{\Gamma_5} \dot{\omega}_{eon,S} \, \mathrm{d}x$ is the ionic contribution to the area specific current. The $Z_{ion}^{\perp}$ can be understood as the sum of a surface Z_{surf} and a bulk polarization resistance, $Z_{bulk} = Z_{ion}^{\perp} - Z_{surf}$, where the Z_{surf} is the portion of the area-specific resistance due to effects of the exposed boundary Γ_5 and it is given by

$$Z_{surf} = U_T \frac{< \hat{\mu}_{ion}^{\star} >_{\Gamma_5} - < \hat{\mu}_{eon}^{\star} >_{\Gamma_5}}{\hat{j}_{IP}^{(1)}}. \tag{5.6}$$

In our model, by definition, the $Z_{surf} \in \mathbb{R}^+$ is proportional to $(1 + W_1/W_2)$ and inversely proportional to both $\tilde{p}_{H_2}$ and k_f

$$Z_{surf} = \frac{1}{2} \left(1 + \frac{W_1}{W_2} \right) \frac{U_T}{e k_f \tilde{p}_{H_2}}. \tag{5.7}$$

The fraction $f_{surf} = \dfrac{Z_{surf}}{Z_{ion}^{\perp}}$ indicates what portion of the polarization impedance is due to surface effects. From figure 5.2 we note two fundamental facts: first, as we expect, at

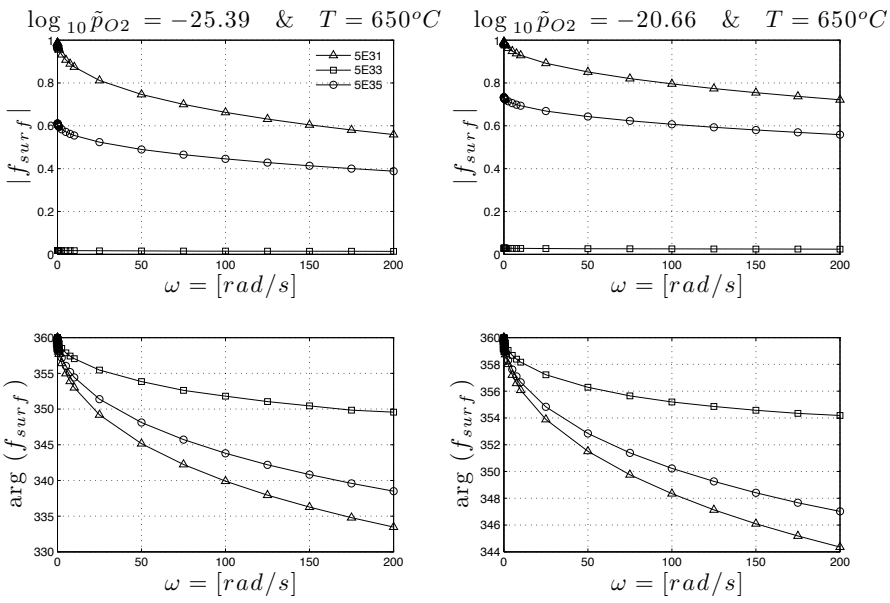

Figure 5.2: Plot of $f_{surf} = \frac{R_{surf}}{R_{ion}^{\perp}}$ as a complex function of ω. We present two cases, both at 650^oC, the one to the left at very reducing conditions $\tilde{p}_{O_2} = 10^{-25.32}$ and the one to the right at $\tilde{p}_{O_2} = 10^{-20.66}$, parametrized versus $\tilde{k}_f^{(0)}$.

"lower" injection rates the f_{surf} increases, physically this means that if the chemistry is sufficiently slow it will dominate the polarization resistance leading to an f_{surf} of approximately unity. Second, we notice frequency dependent behavior of $R_{ion}^{\perp}$. Our computations show that f_{surf} decreases with ω, while the dephasing between Z_{surf} and $Z_{\text{ion}}^{\perp}$, described by $\arg(f_{\text{surf}})$, increases with $\tilde{k}_f^0$ and decreases with ω. The behavior of f_{surf} in phase space clearly shows that Z_{surf} includes two interrelated processes:

1. reactions on the surface exposed to the gas;

2. transport of charged species in MIEC.

Within this framework, as ω increases, the losses in the polarization due to drift diffusion increase and surpass the (constant) reaction or surface losses.

5.3.3 Analysis of the 2D Solution

5.3.3.1 Qualitative Considerations

We can then use the framework to study the two complex electrochemical potentials $\hat{\mu}_{\text{eon}} = \hat{n}^{(1)} - \hat{\phi}^{(1)}$ and $\hat{\mu}_{\text{ion}} = \hat{\phi}^{(1)} + \frac{\bar{n}}{2\bar{p}}\hat{n}^{(1)}$ as functions of frequency. In figures 5.3 and 5.4 we plot the 2D distributions of the latter in the computational domain at $T = 650°\text{C}$, $\tilde{p}_{O_2} = 10^{-25}$ and $\tilde{k}_f^0 = 10^{32}$ with frequency ω increasing from 10^{-3} to 10^5 rad/s. Thanks to the figures 5.3 and 5.4, we can address the qualitative behavior of the solution. We first analyze the qualitative distribution of fluxes using the gradient of $|\hat{\mu}_{eon}|$, which gives an idea of electron flux, that electrons flow from the gas|ceria interface Γ_5 onto the ceria|metal interface Γ_4 through a cross-plane current $\hat{I}_g^{CP}$, and concurrently electrons flow onto the ceria|metal interface Γ_5 from its mirror symmetric counterpart. Similarly, the MIEC|metal interface is vacancy blocking, hereby the vacancies correctly flow from the bottom to the top ceria|gas interface Γ_5. It is also clear that the complex potential of the electrons $\hat{\mu}_{\text{eon}}$ changes significantly as ω increases, while $\hat{\mu}_{\text{ion}}$ is relatively unaffected. The penetration depth, which is defined as the vertical displacement from Γ_4 where surface electrons can penetrate into the bulk, decreases with ω as the 1D model hints (in (2.44) the solution decays exponentially with $1/\sqrt{\tau_n^\star \omega}$). As ω increases, the dephasing of $\hat{\mu}_{\text{eon}}$ first increases and then decreases and it is weakly dependent on the distance from Γ_4, or conversely, the penetration depth into the MIEC. We notice that the same dephasing increases and then decreases for $\hat{\mu}_{ion}$. However, while for the vacancies, the behavior of $|\hat{\mu}_{ion}|$ and $\arg(\hat{\mu}_{ion})$ is qualitatively the same, this is not the case for the electrons, where through a wide array of ω's, the qualitative behavior of $|\hat{\mu}_{eon}|$ and $\arg(\hat{\mu}_{eon})$ is distinctly different.

Deriving the electronic and ionic currents from the computations requires some care and

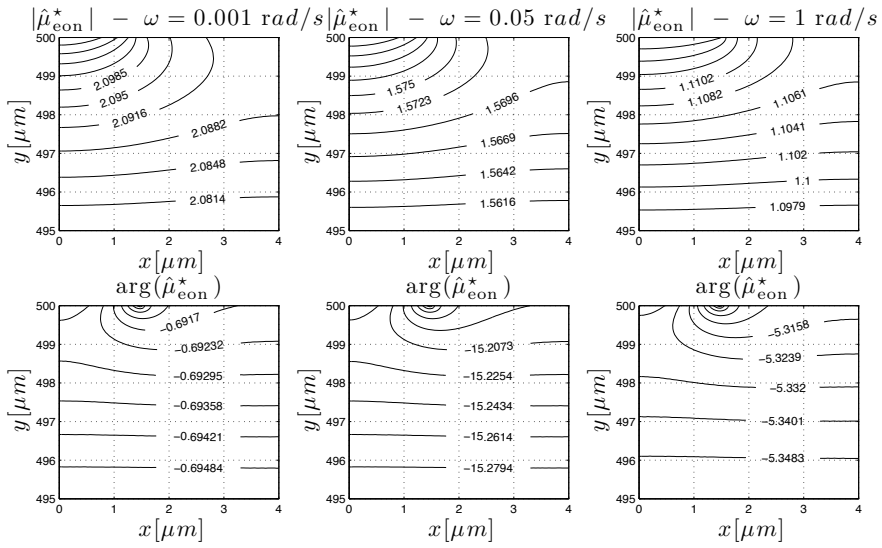

Figure 5.3: Plots of the complex electrochemical potential of electrons $\hat{\mu}_{eon}(x, y, \omega)$ as a function of x and y in the case where $T = 650^o C$ and $\tilde{p}_{O_2} = 10^{-25}$. In the top panels we depict its absolute value $|\hat{\mu}_{eon}|$ while at the bottom we show its argument $\arg(\hat{\mu}_{eon})$. The applied frequency is increased from left to right, going from 0.001 rad/s to 1 rad/s.

it will not simply be $\nabla|\hat{\mu}_m|$. For example, for electrons, we note that:

$$\tilde{\mu}^{(1)}_{eon} = \left(n^{(1)} - \phi^{(1)}\right) e^{i\omega t}. \tag{5.8}$$

We will call the complex current $\mathbf{j}^{\mathbb{C}}_{eon}$:

$$\mathbf{j}^{\mathbb{C}}_{eon} = c^{(0)}_{eon} D_{eon} \mathcal{F}^{-1}[\nabla \hat{\mu}^{(1)}_{eon}], \tag{5.9}$$

the physical current will be*:

$$\mathbf{j}_{eon} \;\; = \;\; \Re\left(\mathbf{j}^{\mathbb{C}}_{eon}\right). \tag{5.10}$$

In order to compare the 1D and 2D solutions qualitatively, we first focus on the case

*We remark that for complex valued function μ in general we have $\text{abs}(\nabla\tilde{\mu}) \neq \nabla\left(\text{abs}\left(\mu\right)\right)$.

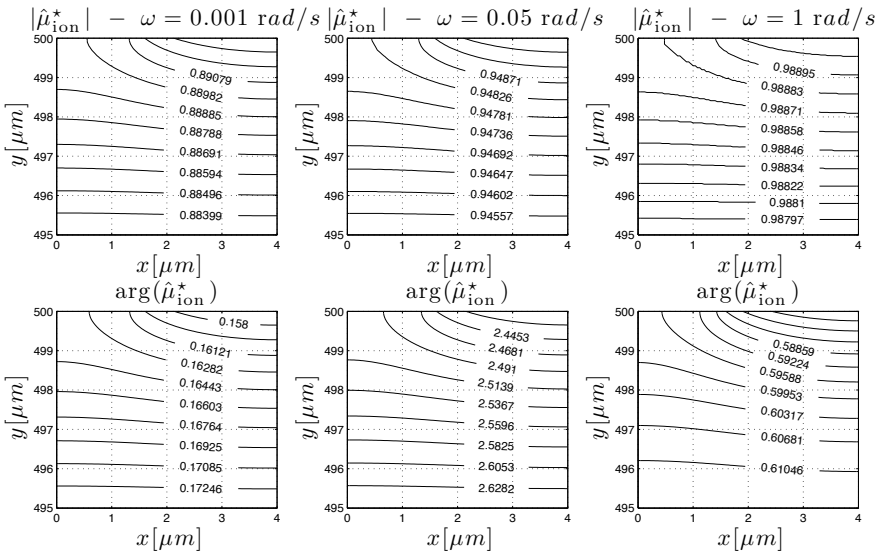

Figure 5.4: Similar to figure 5.3, we depict the complex electrochemical potential of ions $\hat{\mu}_{ion}(x, y, \omega)$ where at the top we show $|\hat{\mu}_{ion}|$ and at the bottom $\arg(\hat{\mu}_{ion})$. The conditions are the same as figure 5.3 and so is the frequency range.

$\omega = 0$ where $\tilde{k}_f^{(0)} = 10^{32}$, and we shrink the size of the slab while keeping the same framework and model parameters. This corresponds to a decrease of the aspect ratio of the sample defined as $AR = \dfrac{l_2}{W_1 + W_2}$. We show in figure 5.6 the results of the computations in the case where the conditions are very reducing. We depict what happens to R_{ion}, R_{eon}, $R^{\perp}_{ion}$ and f_{surf} as AR changes. We notice that decreasing AR corresponds to an increase in effective electronic and ionic resistance compared to the ideal case computed using the definitions of Tab. 3.2 which in turn corresponds to $AR \to \infty$. Deviations from ideality occur already for $AR \approx 25$, hence even for reasonably large AR the ionic and electronic resistances deviate from the ideal 1D case, this is clearly shown in figures 5.6 a and b. The same applies to the polarization resistance $R^{\perp}_{ion}$, figure 5.6c, which is flat above $AR \approx 25$, below this value $R^{\perp}_{ion}$ sharply increases due to bulk polarization effects. As the deviation from the 1D setting starts, not only ionic and electronic resistivities change, but so does the relative importance of surface and drift diffusion effects. Hence the polarization resistance is

thickness-dependent, and the dependence is due to the emergence of two-dimensional effects. The increase in drift diffusion resistance due to the motion of electrons from Γ_5 to Γ_4 is also shown in the f_{surf} which increases with the AR reaching unity for $AR \to \infty$. This effect is even clearer if we plot the electrochemical potentials of electrons and vacancies at $\omega = 0$, we note a shrinking of the affected area as the sample thickness decreases corresponding to an increase of polarization resistance. This effect is purely 2D and cannot be studied using a 1D model.

5.3.3.2 Quantitative Analysis

In order to compare the 1D and 2D solution quantitatively we define the following two functionals:

$$\nu\left[\hat{\mu}_{1D}, \hat{\mu}_{2D}, \tilde{y}, \omega\right] = \frac{1}{W_1 + W_2} \frac{\int_{y'=\tilde{y}} \left|\hat{\mu}_{1D}(y', \omega) - \hat{\mu}_{2D}(\tilde{x}, y', \omega)\right| \, \mathrm{d}\tilde{x}}{|\hat{\mu}_{1D}(l_2, \omega)|}, \tag{5.11a}$$

$$\zeta\left[\hat{\mu}_{1D}, \hat{\mu}_{2D}, \tilde{y}, \omega\right] = \frac{1}{W_1 + W_2} \frac{\left|\int_{y'=\tilde{y}} \left(\hat{\mu}_{1D}(y', \omega) - \hat{\mu}_{2D}(\tilde{x}, y', \omega)\right) \, \mathrm{d}\tilde{x}\right|}{|\hat{\mu}_{1D}(l_2, \omega)|}. \tag{5.11b}$$

The functional ν describes the "pointwise" distance between 1D and 2D solutions of $\hat{\mu}$ at a section $\tilde{y}$ and the functional ζ describes the "average" distance between 1D and 2D descriptions. Physically ν indicates how far apart the 1D and 2D electrochemical potential are, while ζ '"measures" the soundness of fitting a 1D case with the 2D model. We can examine the applicability of the 1D approximation for data fitting via ζ.

In order to further compare the 2D model and 1D model and demonstrate the importance of 2D effects adjacent to the injection sites, the pointwise distance ν and the average distance ζ defined by (5.11b) are computed at the same conditions (T, $\tilde{p}_{O_2}$, $\tilde{k}_f^0$) in the frequency range of $10^{-3} \leq \omega \leq 10^5$ rad/s along the symmetry axis Γ_2, figure 5.7. In the first line we plot the

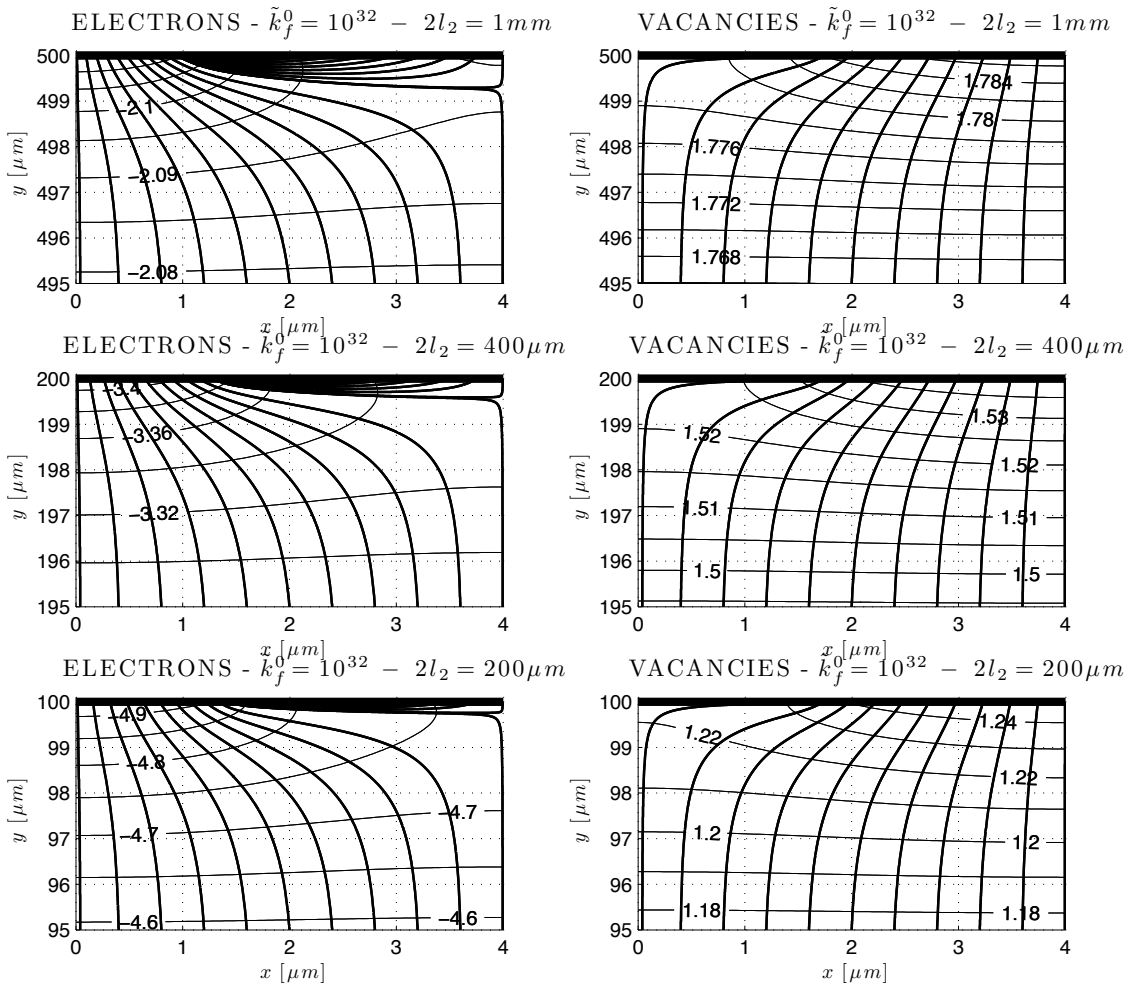

Figure 5.5: Potentials and current lines under small bias excitation, i.e. impedance at $\omega = 0$, at $T = 650^oC$ and $\tilde{p}_{O_2} = 10^{-25.33}$. The $\hat{\mu}_{eon}$ (left column) and $\hat{\mu}_{ion}$ (right column) along with their current lines are plotted. Each row corresponds to a different thickness. As l_2 decreases (from top to bottom row) the area affected by surface reactions thins out; this phenomenon relates to an increase of the polarization resistance. Note that only a small portion of the domain is shown.

case where the sample is very thick with respect to the horizontal dimension ($AR = 125$), both the $\nu_{eon}(\tilde{y}, \omega) = \nu\left[\mu_{eon,1D}, \mu_{eon,2D}, \tilde{y}\right]$ and the $\zeta_{ion}(\tilde{y}, \omega) = \zeta\left[\mu_{ion,1D}, \mu_{ion,2D}, \tilde{y}\right]$ are extremely small and the adjacency between 1D and 2D impedance is near perfect. If we decrease AR to 12.5, then the 1D and 2D solutions tend to be further apart with $\nu_e \approx 25\%$ and ζ_e up to 20%. The difference between the two further increases at $AR = 5$ where the difference between impedance spectra is significant.

5.4 The Effect of Diffusivity Gradients

5.4.1 Extension of the Model

Interface effects are one of the biggest sources of uncertainty in doped ionics because impurities in doped materials tend to segregate near interfaces and affect electro-catalytic processes, absorption and diffusivities near the affected interfaces. Many studies [HJBSM07] [SFK$^+$05] [WHB03] have attempted to address these issues. However, to the authors' knowledge, no continuum model has addressed the relationship of these changes to polarization resistance nor to impedance spectra. In this part of the paper we intend to address the effects of nonuniform diffusivities, which are localized near the interfaces, and which we imagine are due to impurity segregation at the exposed surface (Γ_5 in figure 2.1) and to the MIEC|metal interface (Γ_4)

We shall assume that diffusivities near the MIEC | Gas interface and MIEC | Metal interfaces have non-zero derivatives only along the y direction. We further assume that diffusive effects are symmetric on both ends of the sample $y = \pm l_2$, hence do not affect our initial symmetry assumptions. Lastly we suppose that the functional form of the diffusivities

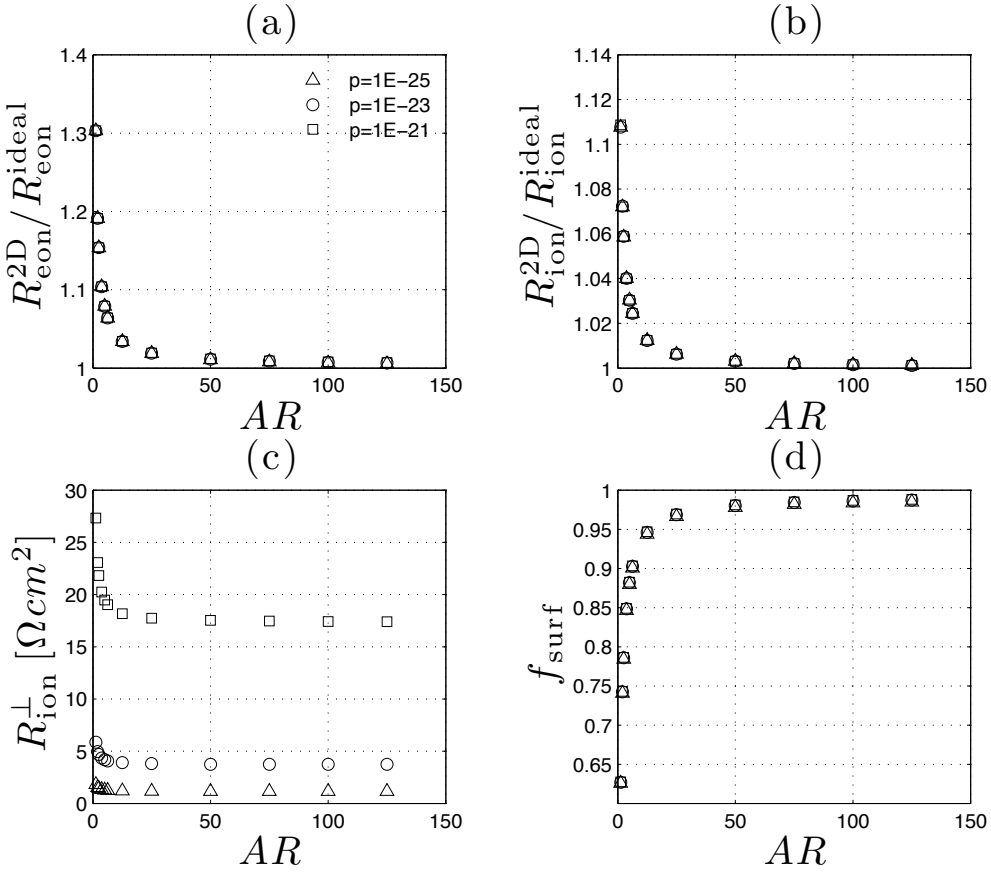

Figure 5.6: Deviation of the 2D model from 1D behavior as a function of the aspect ratio $AR = (W_1 + W_2)/l_2$. We consider the case where $\tilde{k}_f^{(0)} = 10^{32}$, $T = 650^oC$ and we set $\tilde{p}_{O_2} = 10^{-25.32}$ (p = low), $\tilde{p}_{O_2} = 10^{-23.34}$ (p = med), $\tilde{p}_{O_2} = 10^{-20.66}$ (p = high). The R^{2D}_{eon} and the R^{2D}_{ion} monotonically approach their 1D (ideal) value if AR is sufficiently large. $R^{\perp}_{ion}$ increases with decreasing the AR while the f_{surf} decreases, which indicates that if the thickness is reduced enough, the $R^{\perp}_{ion}$ is not just surface dominated.

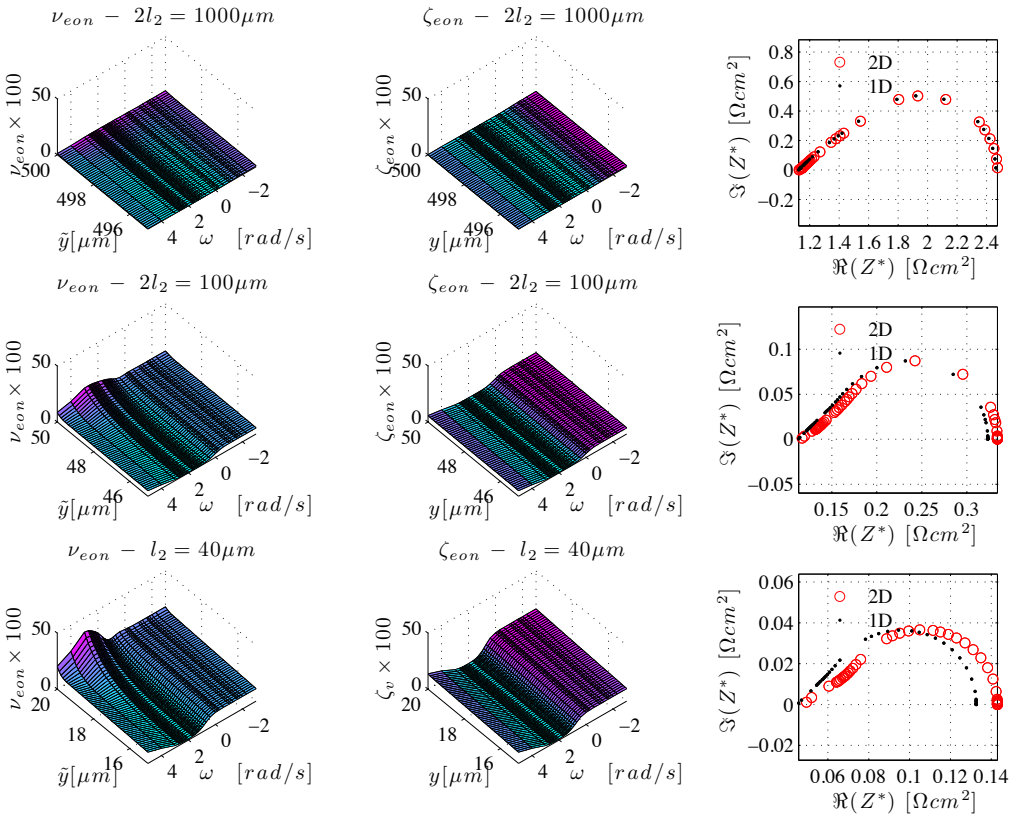

Figure 5.7: Plots of the ν's and ζ's of the electrochemical potential of electrons (plots are shown up to $5\mu m$ from Γ_4 and Γ_5) as function of y and ω and of the impedance spectra as the aspect ratio changes (each line corresponds to a different aspect ratio, $2l_2 = 1000\mu m$, $2l_2 = 100\mu m$ and $2l_2 = 40\mu m$ correspond respectively to $AR = 125$, $AR = 12.5$ and $AR = 5$). A decrease of the aspect ratio corresponds to an increase of both ν and ζ and an increase between the (ideal) 1D impedance and the 2D impedance spectra.

are known in the MIEC and are given by:

$$D_m^\star = 1 + \left(\frac{D_m^{SURF}}{D_m^{BULK}} - 1 \right) e^{-\frac{|l_c \tilde{y} \pm l_2|}{\lambda_m}} \tag{5.12}$$

where m can be either *eon* or *ion*, and λ_m, the length scale of diffusive changes, is much smaller than l_c, the characteristic length scale of the sample ($\lambda_m \ll l_c$). We stress again that the main assumptions are that the diffusivity gradients parallel to the interfaces are null and that the diffusivity gradients do not affect bulk properties of the material or the defect chemistry. In other words, near-interface effects involve only diffusivities.

Under the same small perturbation assumptions we used above we can deduce that the equations that describe the impedance spectra behavior of ions and electrons are given by[†]:

$$n^{(1)} = \frac{\bar{n}}{\bar{p}} p^{(1)} \tag{5.13a}$$

$$\frac{\tau_n}{\tau} \partial_{\tilde{t}} n^{(1)} + \nabla_{\tilde{x}} \cdot \left(-D_{eon}^\star \left(\nabla_{\tilde{x}} n^{(1)} - \nabla_{\tilde{x}} \tilde{\phi}^{(1)} \right) \right) = 0 \tag{5.13b}$$

$$\frac{\tau_p}{\tau} \partial_{\tilde{t}} p^{(1)} + \nabla_{\tilde{x}} \cdot \left(-D_{ion}^\star \left(\nabla_{\tilde{x}} p^{(1)} + 2 \nabla_{\tilde{x}} \tilde{\phi}^{(1)} \right) \right) = 0 \tag{5.13c}$$

The sum of the (5.13) and their weighted difference lead to (see appendix B):

$$\frac{\tau_n^\star}{\tau} \partial_{\tilde{t}} n^{(1)} + \nabla_{\tilde{x}} \cdot \left(-a_{11} \nabla_{\tilde{x}} n^{(1)} - a_{12} \nabla_{\tilde{x}} \tilde{\phi}^{(1)} \right) = 0 \tag{5.14a}$$

$$\frac{\tau_\phi^\star}{\tau} \partial_{\tilde{t}} n^{(1)} + \nabla_{\tilde{x}} \cdot \left(-a_{21} \nabla_{\tilde{x}} n^{(1)} - a_{22} \nabla_{\tilde{x}} \tilde{\phi}^{(1)} \right) = 0 \tag{5.14b}$$

[†]In order to ensure linearity, we assume that $\left| D_k n^{(1)} \nabla \tilde{\phi}^{(1)} \right| \ll \left| D_k \nabla n^{(1)} \right| \approx \left| D_k \nabla \tilde{\phi} \right|$

where:

$$a_{11} = \frac{D^\star_{eon} + \frac{\bar{n}}{4\bar{p}} D^\star_{ion}}{1 + \frac{\bar{n}}{4\bar{p}}} \; ; \; a_{12} = \frac{D^\star_{ion} - D^\star_{eon}}{1 + \frac{\bar{n}}{4\bar{p}}} \tag{5.15a}$$

$$a_{21} = \frac{D^\star_{ion} - D^\star_{eon}}{1 + \frac{4\bar{p}}{\bar{n}}} \; ; \; a_{22} = \frac{D^\star_{eon} + \frac{4\bar{p}}{\bar{n}} D^\star_{ion}}{1 + \frac{4\bar{p}}{\bar{n}}} \tag{5.15b}$$

The (5.14) with appropriate boundary conditions, (2.39), are quasilinear and hence can be Fourier transformed. In short they can be recast in weak form as in (2.40):

$$\begin{aligned} \omega\tau^\star_n \int_\Omega \hat{n}^{(1)}_{Im} m_{Re} \, \mathrm{d}\tilde{A} \; &- \; \int_\Omega a_{11} \nabla \hat{n}^{(1)}_{Re} \cdot \nabla m_{Re} \, \mathrm{d}\tilde{A} - \int_\Omega a_{12} \nabla \hat{\phi}^{(1)}_{Re} \cdot \nabla m_{Re} \, \mathrm{d}\tilde{A} \\ &+ \; \int_{\Gamma_5} \tilde{A}_{n,2} \hat{n}^{(1)}_{Re} m_{Re} \, \mathrm{d}\tilde{x} - 4\frac{\bar{p}}{\bar{n}} \int_{\Gamma_4} \partial_{\tilde{y}} \hat{\phi}^{(1)}_{Re} m_{Re} \, \mathrm{d}\tilde{x} = 0 \end{aligned} \tag{5.16a}$$

$$\begin{aligned} \omega\tau^\star_n \int_\Omega \hat{n}^{(1)}_{Re} m_{Im} \, \mathrm{d}\tilde{A} \; &+ \; \int_\Omega a_{11} \nabla \hat{n}^{(1)}_{Im} \cdot \nabla m_{Im} \, \mathrm{d}\tilde{A} + \int_\Omega a_{12} \nabla \hat{\phi}^{(1)}_{Im} \cdot \nabla m_{Im} \, \mathrm{d}\tilde{A} \\ &- \; \int_{\Gamma_5} \tilde{A}_{n,2} \hat{n}^{(1)}_{Im} m_{Im} \, \mathrm{d}\tilde{x} + 4\frac{\bar{p}}{\bar{n}} \int_{\Gamma_4} \partial_{\tilde{y}} \hat{\phi}^{(1)}_{Im} m_{Im} \, \mathrm{d}\tilde{x} = 0 \end{aligned} \tag{5.16b}$$

$$\begin{aligned} \omega\tau^\star_\phi \int_\Omega \hat{n}^{(1)}_{Im} \psi_{Re} \, \mathrm{d}\tilde{A} \; &- \; \textstyle\int_\Omega a_{21} \nabla \hat{n}^{(1)}_{Re} \cdot \nabla \psi_{Re} \, \mathrm{d}\tilde{A} - \int_\Omega a_{22} \nabla \hat{\phi}^{(1)}_{Re} \cdot \nabla \psi_{Re} \, \mathrm{d}\tilde{A} \\ &+ \; \int_{\Gamma_5} \tilde{A}_{\phi,2} \hat{n}^{(1)}_{Re} \psi_{Re} \, \mathrm{d}\tilde{x} = 0 \end{aligned} \tag{5.16c}$$

$$\begin{aligned} \omega\tau^\star_\phi \int_\Omega \hat{n}^{(1)}_{Re} \psi_{Im} \, \mathrm{d}\tilde{A} \; &+ \; \textstyle\int_\Omega a_{21} \nabla \hat{n}^{(1)}_{Im} \cdot \nabla \psi_{Im} \, \mathrm{d}\tilde{A} + \int_\Omega a_{22} \nabla \hat{\phi}^{(1)}_{Im} \cdot \nabla \psi_{Im} \, \mathrm{d}\tilde{A} \\ &- \; \int_{\Gamma_5} \tilde{A}_{\phi,2} \hat{n}^{(1)}_{Im} \psi_{Im} \, \mathrm{d}\tilde{x} = 0 \end{aligned} \tag{5.16d}$$

where:

$$\tilde{A}_{n,2} = a_{11}\tilde{A}_n + a_{12}\tilde{A}_\phi \tag{5.17}$$

$$\tilde{A}_{\phi,2} = a_{21}\tilde{A}_n + a_{12}\tilde{A}_\phi \tag{5.18}$$

$$\tag{5.19}$$

If we change the diffusivity of vacancies at the gas | ceria (Γ_5) and metal | ceria (Γ_4) interface by changing α_{ion}, we need to adjust the $\tilde{k}_f^0$ as follows, in order to keep the same rate of injection $\dot{\omega}_{eon}^S$, (2.24):

$$\tilde{k}_f^{(0)}\left(\alpha_{ion}\right) = \frac{\left(\alpha_{ion}\right)_{\text{ref}}}{\alpha_{ion}} \left(\tilde{k}_f^0\right)_{ref} \tag{5.20}$$

Numerically we use the same approach described for the linear case but we need the error estimator to account for off-diagonal and space dependent parameters, (5.15) (in the linear case $a_{11} = a_{22} = 1$, $a_{12} = a_{21} = 0$).

Finally we note that we assume that the model holds for length-scales just one order of magnitude greater that the lattice parameter [ZWTL01]. This approximation can be justified heuristically using the work of Armstrong [AH97] [HA99], which shows that deviations of the continuum drift-diffusion approach from atomistic models are usually small, even in cases where field effects are big.

5.4.2 Results of the Model

We first ran the model at steady state ($\omega = 0$) with the objective to analyze the $f_{surf} = \frac{R_{surf}}{R_{ion}^{\perp}}$ for a wide array of parameters $\alpha_{eon} = D_{eon}^{SURF}/D_{eon}^{BULK}$ and $\alpha_{ion} = D_{ion}^{SURF}/D_{ion}^{BULK}$, where $\alpha_{eon} = \alpha_{ion}$ and $\lambda_{eon} = \lambda_{ion}$ at varying $\tilde{k}_f^{(0)}$. For reasonable fitted values (Tab. 5.1) and for a wide parameter set, we show that the polarization resistance is surface dominated making $f_{surf} \approx 1$ robustly.

If chemical reaction rates are "sufficiently" slow (e.g., $\tilde{k}_f^0 \approx 10^{32}$) and if the sample is sufficiently thick, then the polarization resistance is dominated by surface effects in the linear case ($\alpha_{ion} = 1$), corresponding to an absence of diffusive gradients at the exposed surface. If impurities are present at the exposed surface, diffusivities of charged species may

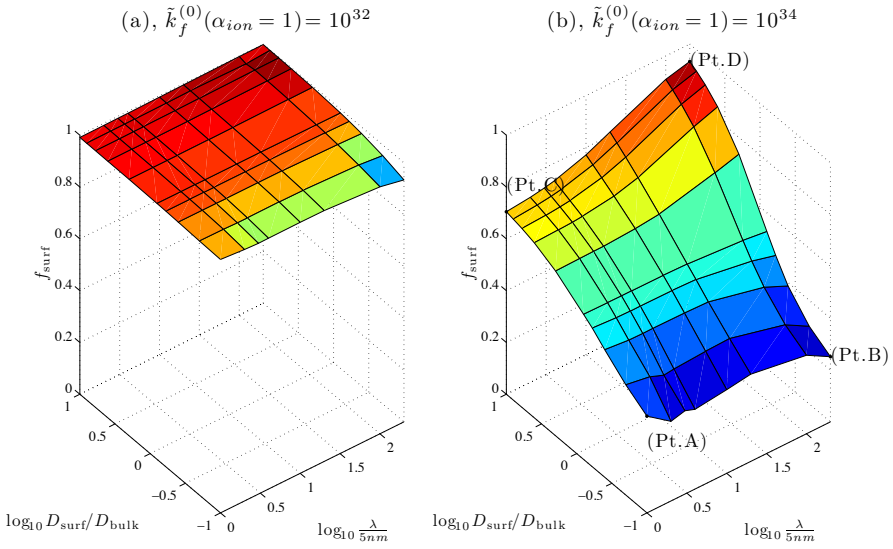

Figure 5.8: Depiction of f_{surf} in the case $T = 650^oC$ and $\tilde{p}_{O_2} = 10^{-25.32}$ as a function of the ratio between near interface and bulk diffusivity, $\alpha_{ion} = D_{ion}^{SURF}/D_{ion}^{BULK}$ and $\alpha_{eon} = D_{eon}^{SURF}/D_{eon}^{BULK}$ ($\alpha_{ion} = \alpha_{eon}$), and length scale of the diffusive gradient $\lambda_{ion} = \lambda_{eon}$, for $k_f^{(0)} = 10^{32}$ (left panel) and $k_f^{(0)} = 10^{34}$ (right panel).

change and hence one could argue that the polarization resistance is not surface dominated. In order to address this point, we ran two limiting cases, one featuring "slow" chemistry ($\tilde{k}_f^0(\alpha_{ion} = 1) \approx 10^{32}$) and the other one at "fast" chemistry ($\tilde{k}_f^0(\alpha_{ion} = 1) \approx 10^{34}$). We present the results of these calculations in figure 5.8 where we plot f_{surf} as a function of both $\alpha_{ion} = \alpha_{eon}$ and the diffusive gradients $\lambda_{ion} = \lambda_{eon}$. We notice from figure 5.8a that f_{surf} is very close to unity for two order of variation of surface-to-bulk diffusivity ratio $0.1 \leq \alpha_{ion} \leq 10$ and for a wide span of diffusivity length-scales $5nm \leq \lambda_{ion} \leq 1\mu m$. This indicates that if we perturb the surface diffusivity up to one order of magnitude with respect to its bulk value its impact on polarization resistance is minimal. The qualitative effect on the impedance is also small as shown for a variety of cases in figure 5.9.

If we choose a "fast" chemistry condition instead, e.g. $\tilde{k}_f^0 \approx 10^{34}$, the situation changes significantly from the base case ($\alpha_{ion} = 1$), figure 5.8b. In this figure we focus on points A through D. (Pt. A), having $\alpha_{ion} = 0.1$ and $\lambda_{ion} = 5nm$, indicates that near surface

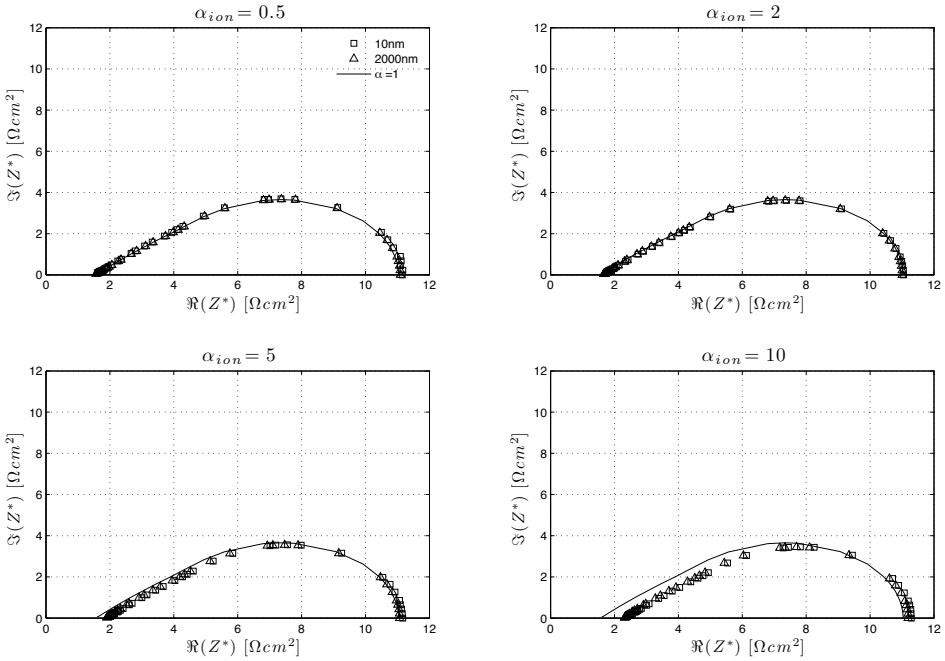

Figure 5.9: Impedance of the sample under the conditions: $\tilde{k}_f^{(0)} = 10^{32}$, $\tilde{p}_{O_2} = 10^{-25.33}$ and $T = 650^oC$, where $\alpha_{eon} = \alpha_{ion}$ ($\alpha_m = D_m^{\mathrm{SURF}}/D_m^{\mathrm{BULK}}$) and $\lambda_{ion} = \lambda_{eon}$. The solid line represents the case where $\alpha_{ion} = 1$, the triangles and the squares indicate respectively $\lambda_{ion} = 5nm$ and $\lambda_{ion} = 1\mu m$. Each panel corresponds to a different value of α_{ion}. Only small deviations occur from the case $\alpha_{ion} = 1$

diffusivities are an order of magnitude lower than their bulk value and this deviation is concentrated near the surface: in this case the polarization resistance is drift-diffusion dominated. If the diffusive length scale is increased to $\lambda_{ion} = 1\mu m$, while keeping $\alpha_{ion} = 0.1$, (Pt. B), the f_{surf} will not decrease much further. Starting from (Pt. A) we can move to (Pt. C), where diffusivity gradients are sharp ($\lambda_{ion} = 5nm$) but the diffusivities at the surface are an order of magnitude greater than its bulk value. In this case, the f_{surf} increases because of the increase in the bulk diffusivity. Going from (Pt. C) to (Pt. D) increases the length-scale of the diffusive effects leading in turn to bigger increase of f_{surf}.

We can summarize our findings as follows:

1. if the rate of injection of electrons is sufficiently "small" (slow chemistry) and of the order of the fitted values reported in Tab. 5.1, then the diffusivity grandients localized at interfaces will affect little the polarization resistance and the impedance spectra;

2. if the chemistry is sufficiently fast, sharp changes in diffusivity can strongly affect not only the impedance behavior but also the polarization. In particular, if the diffusivities increase sufficiently, strictly near the interfaces, the polarization effects will shift to be surface dominated, while a decrease is associated to drift-diffusion dominated polarization resistance.

5.5 Concluding Remarks

In this chapter we developed a general two-dimensional numerical framework for the coupled surface chemistry, electrochemistry and transport processes in mixed conductors based on the finite element method. As a specialized application of the framework, a time dependent model was formulated based on first principles for the AC impedance spectra (IS) of a

samaria doped ceria (SDC) electrolyte with symmetric metal patterns on both sides, and the IS was simulated for typical fuel cell operation conditions in a uniform gas atmosphere (H_2, H_2O, Ar) at thermodynamic equilibrium using the small perturbation technique.

The validity of the model is demonstrated by fitting to experimental (1D) impedance spectra data of an SDC cell in literature, varying only the reaction rate at the SDC | gas interface. Excellent agreement ($\leq$ 2% error) was obtained. We then numericallly investigated the influence of the variation of several parameters on the polarization resistance and the impedance spectra, especially within regimes not probable for the 1D studies. Our calculation shows that the 2D effect of cell thickness variation on the spectra becomes pronounced as the aspect ratio goes below a certain threshold (25 for this work); surface reaction dominates the polarization resistance when the injection rate at the SDC surface exposed to gas is sufficiently slow; sharp gradients in diffusion coefficient strongly influence both impedance behavior and polarization when surface chemistry is sufficiently fast.

The discussions in this work provide useful insights into the correlation between materials properties of SDC and its applications in fuel cells, intensely studied by the solid oxide fuel cell researchers. In addition, the geometric capability (up to 3D) and high computation efficiency makes this numerical framework an ideal tool for the general study of mixed conductors.

Chapter 6

Fast Impedance Spectra for Thin Film Mixed Conductors

6.1 Background

In this chapter we study the impedance of thin film mixed conductors. We utilize the same impedance spectra calculation method of chapters 2 and 5. We shall consider a symmetric cell, reported in figures 1.5(b) and 6.1, where a thin single crystal doped Ceria layer is deposited on top of a thick single crystal YSZ slab and a current collecting pattern of metal is present on top of the Ceria. Typically the Ceria layer thickness ranges from 0.1 to 10 μm. The YSZ is much thicker, of the order of 1 mm.

Due to its thickness, the YSZ slab is approximated as one-dimensional; similarly, due to its high electronic conductivity, the behavior of the metal is one-dimensional. Hence, we suppose that the only two-dimensional effects will arise from drift diffusion and surface reactions in the thin mixed conducting layer.

The tools used to solve this problem are very similar to the ones used in the thick MIEC case. However. in the thin film case we cannot assume that the net capacitance of interfaces is negligible. In particular, we will need to analyze the interfaces Ceria | Metal, Ceria | YSZ

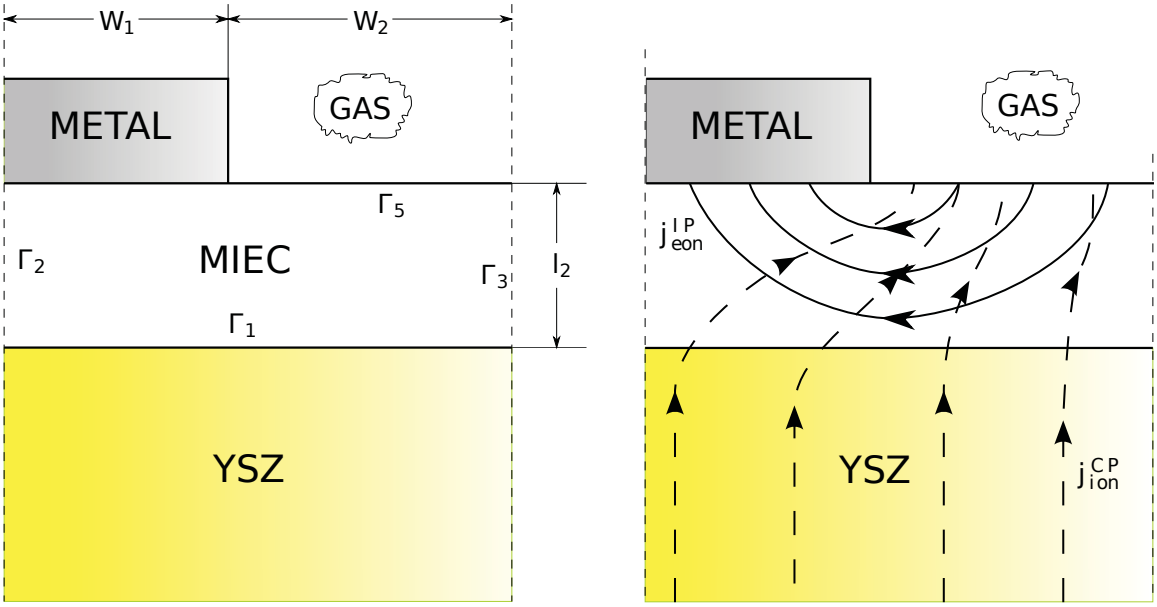

Figure 6.1: (right) Schematic depiction of the thin film assembly, a thin film of mixed conductor is deposited on top of the ionic conductor (YSZ) and a electronic current collector (metal) is deposited on top the MIEC. (left) Depiction of the ionic and electronic fluxes in this system.

and Gas | Ceria* in more detail. In order to understand qualitatively the impact of these interfaces on the impedance, it is useful to refer back to the equivalent circuit description of this system, figure 6.2. It is straightforward to deduce that since electrons are minority carriers the effects of Ceria | Metal and Ceria | YSZ will act in series, with respect to the MIEC. If the relevant time scales are significantly different, then their contribution can be directly subtracted from the impedance spectra data. It is important to stress also that the resistance of the Ceria | Metal and Ceria | YSZ interfaces can be assumed to be significantly smaller than the polarization resistance. On the other hand, the contribution of the Gas | Ceria interface will act in parallel with the MIEC drift-diffusion and with the subsequent transport of electrons onto the current collector.

This justifies choosing a model satisfying the following hypotheses:

*The chemical capacitance, defined in Tab. 3.2, and the interface capacitances have the same order of magnitude: $C \approx 10^{-3} F/cm^2$.

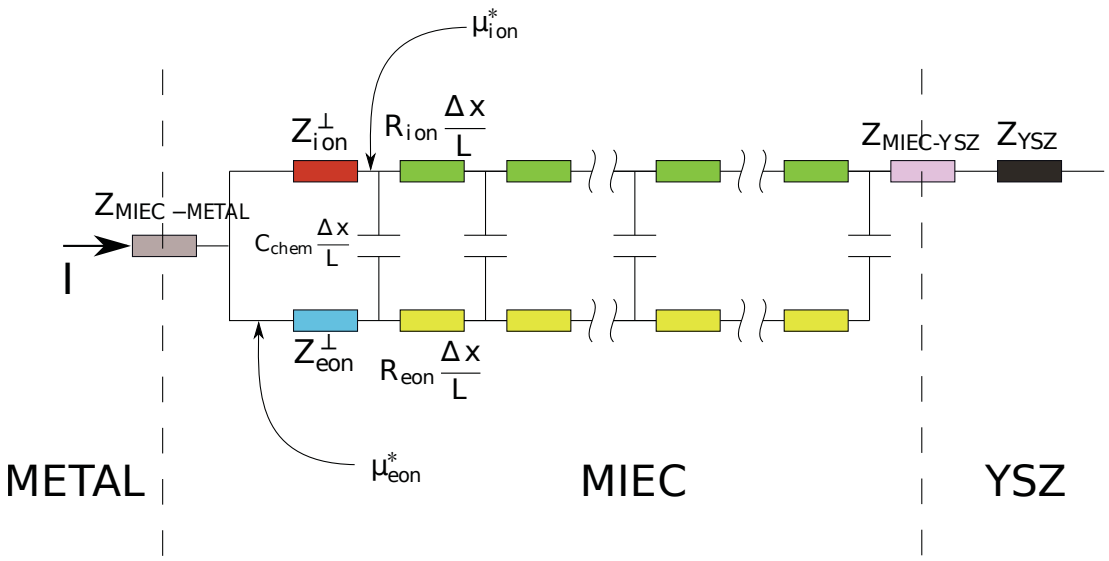

Figure 6.2: Equivalent circuit representation of the the thin film system of figure 6.1

1. the YSZ slab behavior can be approximated as one-dimensional and the interface between YSZ and the MIEC under small bias conditions is reversible, hence we can fix its potential to a constant at the Ceria | YSZ interface;

2. The Metal can be approximated as one-dimensional and the interface Metal | Ceria can be assumed reversible and having constant electric potential;

3. At Gas | Ceria interface gaseous species are adsorbed, leading to a charged layer, which in turn generates a capacitive effect. The adsorbed species react with electrons and ions in the bulk of Ceria leading to net fluxes of electrons and ions injected onto the MIEC. This process, when linearized, gives rise to a local impedance response. Here we assume that such response is ideal, i.e., the same response of an ideal capacitor and a resistor in parallel.

6.1.1 Impedance Spectra Equations

The Impedance Spectroscopy (IS) equations have been derived in chapter 2 and they can be rewritten here in Fourier Space as follows:

$$i\omega\tau_n^\star \hat{n}_{\mathrm{EN}}^{(1)} - \triangle_{\tilde{x}} \hat{n}_{\mathrm{EN}}^{(1)} = 0, \tag{6.1a}$$

$$i\omega\tau_\phi^\star \hat{n}_{\mathrm{EN}}^{(1)} - \triangle_{\tilde{x}} \hat{\phi}_{\mathrm{EN}}^{(1)} = 0, \tag{6.1b}$$

where the usual notation for $\hat{n}_{\mathrm{EN}}^{(1)}$ and $\hat{\phi}_{\mathrm{EN}}^{(1)}$ is used, see the Section 2.5, and the subscript *EN* is added in order to emphasize that the solution of (6.1) supposes electroneutrality. We recall also that by definition

$$\tau_n^\star = \frac{\tau_n + \frac{\bar{n}}{4\bar{p}}\tau_p}{1 + \frac{\bar{n}}{4\bar{p}}}, \tag{6.2a}$$

$$\tau_\phi^\star = \frac{\tau_p - \tau_n}{1 + \frac{4\bar{p}}{\bar{n}}}, \tag{6.2b}$$

where $\tau_n = l_c^2/D_{eon}$ and $\tau_p = l_c^2/D_{eon}$.

6.1.2 Boundary Layer Correction

The derivation of the (6.1) came from singular expansion and subsequent linearization of the drift diffusion (the two operations commute since small external forcing can be chosen arbitrarily small). In the previous chapters, since the sample under study was sufficiently thick it was not paramount to solve the double layer near the exposed surface. Because our

current focus is on the study of thin films, we will need to correct the (6.1). In other words, we will need to add to the electroneutral equations a simplified boundary layer solution for the MIEC | Gas interface. Again, the starting point of this analysis is the following set of linearized drift-diffusion equations in Fourier space, (2.14):

$$\triangle_{\tilde{x}}\hat{\phi}^{(1)} = \lambda^2\left(\bar{n}\hat{n}^{(1)} - \bar{p}\hat{p}^{(1)}\right), \tag{6.3a}$$

$$i\omega\tau_n\hat{n}^{(1)} + \triangle_{\tilde{x}}\hat{\phi}^{(1)} - \triangle_{\tilde{x}}\hat{n}^{(1)} = 0, \tag{6.3b}$$

$$i\omega\tau_p\hat{p}^{(1)} - 2\triangle_{\tilde{x}}\hat{\phi}^{(1)} - \triangle_{\tilde{x}}\hat{p}^{(1)} = 0. \tag{6.3c}$$

For only highly doped oxides at high temperatures the condition $\lambda \gg 1$ is common,(in the case SDC at $T \approx 600^oC$ and if $l_c = 10\ \mu m$, we will have $\lambda \approx 10^{10}$). The solution of the full problem $\left(\hat{\phi}^{(1)}_{\text{FULL}},\ \hat{n}^{(1)}_{\text{FULL}},\ \hat{p}^{(1)}_{\text{FULL}}\right)$ can be thought as the sum of the electroneutral solution (subscript EN) plus a double layer correction (subscript DL):

$$\hat{\phi}^{(1)}_{\text{FULL}}(\tilde{\mathbf{x}}) = \hat{\phi}^{(1)}_{\text{EN}}(\tilde{\mathbf{x}}) + \hat{\phi}^{(1)}_{\text{DL}}(\tilde{\mathbf{x}}), \tag{6.4a}$$

$$\hat{n}^{(1)}_{\text{FULL}}(\tilde{\mathbf{x}}) = \hat{n}^{(1)}_{\text{EN}}(\tilde{\mathbf{x}}) + \hat{n}^{(1)}_{\text{DL}}(\tilde{\mathbf{x}}), \tag{6.4b}$$

$$\hat{p}^{(1)}_{\text{FULL}}(\tilde{\mathbf{x}}) = \hat{p}^{(1)}_{\text{EN}}(\tilde{\mathbf{x}}) + \hat{p}^{(1)}_{\text{DL}}(\tilde{\mathbf{x}}), \tag{6.4c}$$

where the scale of variation of the correction $\left(\hat{\phi}^{(1)}_{\text{DL}},\ \hat{n}^{(1)}_{\text{DL}},\ \hat{p}^{(1)}_{\text{DL}}\right)$ is much smaller than the scale of variation of the electroneutral solution $\left(\hat{\phi}^{(1)}_{\text{EN}},\ \hat{n}^{(1)}_{\text{EN}},\ \hat{p}^{(1)}_{\text{EN}}\right)$ and where, as shown previously, $p^{(1)}_{\text{EN}} = \dfrac{\bar{n}}{2\bar{p}}n^{(1)}_{\text{EN}}$. If we plug the definitions (6.4) into the equations (6.3) we will obtain that

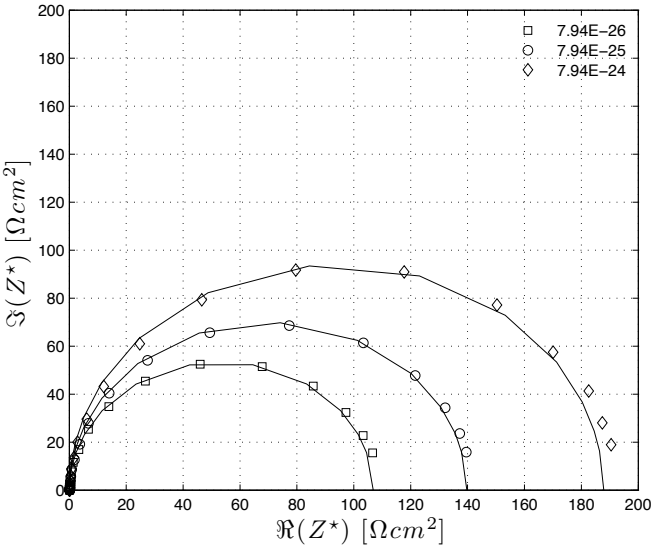

Figure 6.3: Fitted electrochemical impedance, solid line, versus the experimental impedance of a Ceria thin film [CH09] for $l_2 = 380nm$, $T = 650^oC$ and $\tilde{p}_{O_2} = 7.94 \times 10^{-26},\ 7.94 \times 10^{-25},\ 7.94 \times 10^{-25}$. The fitted $\tilde{k}_f^0$ are respectively $2.5 \times 10^{30},\ 3.4 \times 10^{30},\ 4.5 \times 10^{30}$.

$$\triangle_{\tilde{x}} \left(\hat{\phi}_{\mathrm{EN}}^{(1)} + \hat{\phi}_{\mathrm{DL}}^{(1)} \right) = \lambda^2 \left(\bar{n} \left(\hat{n}_{\mathrm{EN}}^{(1)} + \hat{n}_{\mathrm{DL}}^{(1)} \right) - \bar{p} \left(\hat{p}_{\mathrm{EN}}^{(1)} + \hat{p}_{\mathrm{DL}}^{(1)} \right) \right), \tag{6.5a}$$

$$i\omega\tau_n \left(\hat{n}_{\mathrm{EN}}^{(1)} + \hat{n}_{\mathrm{DL}}^{(1)} \right) + \triangle_{\tilde{x}} \left(\hat{\phi}_{\mathrm{EN}}^{(1)} + \hat{\phi}_{\mathrm{DL}}^{(1)} \right) - \triangle_{\tilde{x}} \left(\hat{n}_{\mathrm{EN}}^{(1)} + \hat{n}_{\mathrm{DL}}^{(1)} \right) = 0, \tag{6.5b}$$

$$i\omega\tau_p \left(\hat{p}_{\mathrm{EN}}^{(1)} + \hat{p}_{\mathrm{DL}}^{(1)} \left(\tilde{\mathbf{x}}/\lambda \right) \right) - 2\triangle_{\tilde{x}} \left(\hat{\phi}_{\mathrm{EN}}^{(1)} + \hat{\phi}_{\mathrm{DL}}^{(1)} \right) - \triangle_{\tilde{x}} \left(\hat{p}_{\mathrm{EN}}^{(1)} + \hat{p}_{\mathrm{DL}}^{(1)} \right) = 0. \tag{6.5c}$$

Using (6.1) and the electroneutrality condition in (6.5), it follows that

$$\triangle_{\tilde{x}} \hat{\phi}_{\mathrm{DL}}^{(1)} \quad + \quad i\omega\tau_n^\star \hat{n}_{\mathrm{EN}}^{(1)} = \lambda^2 \left(\bar{n} \hat{n}_{\mathrm{DL}}^{(1)} - 2\bar{p} \hat{p}_{\mathrm{DL}}^{(1)} \right), \tag{6.6a}$$

$$i\omega\tau_n \hat{n}_{\mathrm{DL}}^{(1)} \quad + \quad \triangle_{\tilde{x}} \hat{\phi}_{\mathrm{DL}}^{(1)} - \triangle_{\tilde{x}} \hat{n}_{\mathrm{DL}}^{(1)} = 0, \tag{6.6b}$$

$$i\omega\tau_p \hat{p}_{\mathrm{DL}}^{(1)} \quad - \quad 2\triangle_{\tilde{x}} \hat{\phi}_{\mathrm{DL}}^{(1)} - \triangle_{\tilde{x}} \hat{p}_{\mathrm{DL}}^{(1)} = 0. \tag{6.6c}$$

We now transform the coordinates from $\tilde{\mathbf{x}}$ to $\mathbf{x}_+$ as follows $\tilde{\mathbf{x}} \to \mathbf{x}_+ : \ \mathbf{x}_+ = (x_+, y_+) = (\tilde{x}, \tilde{y}/\lambda)$ and the equations above become

$$\left(\frac{1}{\lambda^2}\frac{\partial^2}{\partial x_+^2} + \frac{\partial^2}{\partial y_+^2}\right)\hat{\phi}_{\mathrm{DL}}^{(1)} + i\frac{\omega\tau_n^\star}{\lambda^2}\hat{n}_{\mathrm{EN}}^{(1)} = \bar{n}\hat{n}_{\mathrm{DL}}^{(1)} - 2\bar{p}\hat{p}_{\mathrm{DL}}^{(1)}, \tag{6.7a}$$

$$i\frac{\omega\tau_n}{\lambda^2}\hat{n}_{\mathrm{DL}}^{(1)} + \left(\frac{1}{\lambda^2}\frac{\partial^2}{\partial x_+^2} + \frac{\partial^2}{\partial y_+^2}\right)\hat{\phi}_{\mathrm{DL}}^{(1)}\left(\frac{1}{\lambda^2}\frac{\partial^2}{\partial x_+^2} + \frac{\partial^2}{\partial y_+^2}\right)\hat{n}_{\mathrm{DL}}^{(1)} = 0, \tag{6.7b}$$

$$i\frac{\omega\tau_p}{\lambda^2}\hat{p}_{\mathrm{DL}}^{(1)} - 2\left(\frac{1}{\lambda^2}\frac{\partial^2}{\partial x_+^2} + \frac{\partial^2}{\partial y_+^2}\right)\hat{\phi}_{\mathrm{DL}}^{(1)} - \left(\frac{1}{\lambda^2}\frac{\partial^2}{\partial x_+^2} + \frac{\partial^2}{\partial y_+^2}\right)\hat{p}_{\mathrm{DL}}^{(1)} = 0. \tag{6.7c}$$

We assume that $\frac{\omega\tau_n}{\lambda^2},\ \frac{\omega\tau_p}{\lambda^2} \ll 1$[†] and we note that from the latter it also follows that $\frac{\omega\tau_n^\star}{\lambda^2} \ll 1$. Hence, we will be able to neglect the terms of order $O\left(\frac{1}{\lambda^2}\right)$ and rewrite the layer equations (6.7) in a small neighborhood of the point $(\tilde{x}, \tilde{y})$ on Γ_4 as a one-dimensional time independent drift-diffusion system:

$$\frac{\partial^2\hat{\phi}_{\mathrm{DL}}^{(1)}}{\partial y_+^2} = \bar{n}\hat{n}_{\mathrm{DL}}^{(1)} - 2\bar{p}\hat{p}_{\mathrm{DL}}^{(1)}, \tag{6.8a}$$

$$\frac{\partial^2\hat{\phi}_{\mathrm{DL}}^{(1)}}{\partial y_+^2} - \frac{\partial^2\hat{n}_{\mathrm{DL}}^{(1)}}{\partial y_+^2} = 0, \tag{6.8b}$$

$$2\frac{\partial^2\hat{\phi}_{\mathrm{DL}}^{(1)}}{\partial y_+^2} + \frac{\partial^2\hat{p}_{\mathrm{DL}}^{(1)}}{\partial y_+^2} = 0. \tag{6.8c}$$

If we indicate the non-dimensional charge close to Γ_4 as $\tilde{\rho}_{DL}(\tilde{x}, y_+) = 2\bar{p}\hat{p}_{\mathrm{DL}}^{(1)} - \bar{n}\hat{n}_{\mathrm{DL}}^{(1)}$, then we can further simplify the (6.8) as

[†]For SDC $\omega < 10^5$, $\tau_n, \tau_p \approx 1$ and $\lambda \approx 10^{10}$ which makes $\frac{\omega\tau_{n\cdot}}{\lambda^2},\ \frac{\omega\tau_p}{\lambda^2} \approx 10^{-10} \ll 1$

$$\frac{\partial^2 \hat{\phi}^{(1)}_{\rm DL}}{\partial y_+^2} = -\tilde{\rho}_{DL}, \tag{6.9a}$$

$$\tilde{\rho}_{DL} + \frac{\partial^2 \hat{n}^{(1)}_{\rm DL}}{\partial y_+^2} = 0, \tag{6.9b}$$

$$-2\tilde{\rho}_{DL} + \frac{\partial^2 \hat{p}^{(1)}_{\rm DL}}{\partial y_+^2} = 0. \tag{6.9c}$$

If we multiply the (6.9b) by $-\bar{n}$ and the (6.9c) by $2\bar{p}$ and if we sum the latter two, we will get

$$\frac{\partial^2 \tilde{\rho}_{DL}}{\partial y_+^2} = (4\bar{p} + \bar{n})\tilde{\rho}_{DL}. \tag{6.10}$$

The (6.10) admits one unique non-diverging solution of the form

$$\tilde{\rho}_{DL} = A \exp\left(-\sqrt{4\bar{p} + \bar{n}} y^+\right) = A \exp\left(-\frac{\sqrt{4\bar{p} + \bar{n}}}{\lambda}\tilde{y}\right). \tag{6.11}$$

The total charge $\hat{q}$ per unit of surface area of the layer is then given by

$$\begin{aligned} \hat{q} &= eB \int_0^\infty \rho_{DL} = AeBl_c\lambda \int_0^\infty \exp\left(-\sqrt{4\bar{p} + \bar{n}} y_+\right) \mathrm{d}y_+, \\ &= A\frac{eBl_c}{\sqrt{4\bar{p} + \bar{n}}}. \end{aligned} \tag{6.12}$$

Using the appropriate conditions at infinity $\partial_{y_+}\hat{n}^{(1)}_{DL} = \partial_{y_+}\hat{p}^{(1)}_{DL} = 0$ and $\hat{n}^{(1)}_{DL} = \hat{p}^{(1)}_{DL} = 0$, we obtain that

$$\hat{n}^{(1)}_{DL} = -\frac{q\lambda^2}{eBl_c\sqrt{4\bar{p} + \bar{n}}} \exp\left(-\frac{\sqrt{4\bar{p} + \bar{n}}}{\lambda}\tilde{y}\right), \tag{6.13a}$$

$$\hat{p}^{(1)}_{DL} = 2\frac{q\lambda^2}{eBl_c\sqrt{4\bar{p} + \bar{n}}} \exp\left(-\frac{\sqrt{4\bar{p} + \bar{n}}}{\lambda}\tilde{y}\right). \tag{6.13b}$$

If we suppose that $\hat{q} = C_q \hat{n}_{\mathrm{EN}}^{(1)}$, then we are left with

$$\hat{n}_{DL}^{(1)} = -\frac{q\lambda^2}{eBl_c\sqrt{4\bar{p}+\bar{n}}} \exp\left(-\frac{\sqrt{4\bar{p}+\bar{n}}}{\lambda}\tilde{y}\right), \tag{6.14a}$$

$$\hat{p}_{DL}^{(1)} = 2\frac{q\lambda^2}{eBl_c\sqrt{4\bar{p}+\bar{n}}} \exp\left(-\frac{\sqrt{4\bar{p}+\bar{n}}}{\lambda}\tilde{y}\right). \tag{6.14b}$$

Under the assumptions above, the behavior of the double layer is then purely capacitive, where the capacitance is constant with frequency. Species conservation of the full solution requires that

$$i\omega C_q \hat{n}_{\mathrm{EN}}^{(1)} + \underbrace{\hat{j}_{eon}^{P}\Big|_{\mathrm{SURF}\to\mathrm{DL}}}_{\dot{\omega}_{eon}^{S} \propto k_f \hat{n}_{\mathrm{EN}}^{(1)}} - \hat{j}_{eon}\Big|_{\mathrm{DL}\to\mathrm{BULK}} = 0, \tag{6.15}$$

where $\hat{j}_{eon}^{P}\Big|_{\mathrm{SURF}\to\mathrm{DL}}$ is the Fourier transform of the rate of injection of electrons at the surface due to the chemical reactions into the material (from the surface into the double layer), and $\hat{j}_{eon}\Big|_{\mathrm{DL}\to\mathrm{BULK}}$ is the net rate of injection (in Fourier space) of the electrons from the double layer into the bulk (the part of the material satisfying the electroneutrality conditions). The latter term indicates that the local linearized behavior of Γ_5, the Ceria | Metal interface, is capacitive-resistive; from the definition of Z_{surf}, equation (5.6), it follows that

$$\begin{aligned} Z_{surf} &= U_T \frac{< \hat{\mu}_{ion}^{\star} >_{\Gamma_5} - < \hat{\mu}_{eon}^{\star} >_{\Gamma_5}}{\hat{j}_{IP}^{(1)}\Big|_{\mathrm{DL}\to\mathrm{BULK}}} \\ &= \frac{1}{\dfrac{1}{\dfrac{1}{2}\left(1 + W_1/W_2\right)\dfrac{U_T}{ek_f\tilde{p}_{H_2}}} + i\omega \dfrac{C_Q}{U_T\left(1 + \dfrac{c_{eon}^0}{4c_{ion}^0}\right)}} \dfrac{1}{1 + W_1/W_2}. \end{aligned} \tag{6.16}$$

Hence, the chemical reactions reduce to an RC circuit with the following resistance and

capacitance:

$$R_{surf} = \frac{1}{2}\left(1 + W_1/W_2\right)\frac{U_T}{e k_f \tilde{p}_{H_2}}, \tag{6.17a}$$

$$C_{surf} = \frac{C_Q}{U_T\left(1 + \dfrac{c^0_{eon}}{4c^0_{ion}}\right)}\frac{1}{1 + W_1/W_2}. \tag{6.17b}$$

The equations above show that the surface resistance depends linearly on $(1 + W_1/W_2)$, an important geometrical feature of the system, while the capacitance is inversely proportional with respect to the latter.

The mathematical description of the model will need to change in order to account for non-penetration of electrons into the ionic conductor and the resistive capacitive behavior of the surface. Analogously what we did for equations (2.40), we will need to solve:

$$\begin{aligned}\omega\tau_n^\star \int_\Omega \hat{n}^{(1)}_{Im} m_{Re}\,\mathrm{d}\tilde{A} &- \int_\Omega \nabla\hat{n}^{(1)}_{Re}\cdot\nabla m_{Re}\,\mathrm{d}\tilde{A} + \int_{\Gamma_5}\left(\tilde{A}_n\hat{n}^{(1)}_{Re} - \tilde{A}^C_n\hat{n}^{(1)}_{Im}\right)m_{Re}\,\mathrm{d}\tilde{x} + \dots \\ &- 4\frac{\bar{p}}{\bar{n}}\int_{\Gamma_4}\partial_{\tilde{y}}\hat{\phi}^{(1)}_{Re} m_{Re}\,\mathrm{d}\tilde{x} - \int_{\Gamma_1}\partial_{\tilde{y}}\hat{\phi}^{(1)}_{Re} m_{Re}\,\mathrm{d}\tilde{x} = 0\end{aligned} \tag{6.18a}$$

$$\begin{aligned}\omega\tau_n^\star \int_\Omega \hat{n}^{(1)}_{Re} m_{Im}\,\mathrm{d}\tilde{A} &+ \int_\Omega \nabla\hat{n}^{(1)}_{Im}\cdot\nabla m_{Im}\,\mathrm{d}\tilde{A} - \int_{\Gamma_5}\left(\tilde{A}_n\hat{n}^{(1)}_{Im} + \tilde{A}^C_n\hat{n}^{(1)}_{Re}\right)m_{Im}\,\mathrm{d}\tilde{x} \\ &+ 4\frac{\bar{p}}{\bar{n}}\int_{\Gamma_4}\partial_{\tilde{y}}\hat{\phi}^{(1)}_{Im} m_{Im}\,\mathrm{d}\tilde{x} + \int_{\Gamma_1}\partial_{\tilde{y}}\hat{\phi}^{(1)}_{Im} m_{Im}\,\mathrm{d}\tilde{x} = 0\end{aligned} \tag{6.18b}$$

$$\begin{aligned}\omega\tau_\phi^\star \int_\Omega \hat{n}^{(1)}_{Im}\psi_{Re}\,\mathrm{d}\tilde{A} &- \int_\Omega \nabla\hat{\phi}^{(1)}_{Re}\cdot\nabla\psi_{Re}\,\mathrm{d}\tilde{A} + \cdots \\ &+ \int_{\Gamma_5}\left(\tilde{A}_\phi\hat{n}^{(1)}_{Re} - A^C_\phi\hat{n}^{(1)}_{Im}\right)\psi_{Re}\,\mathrm{d}\tilde{x} = 0\end{aligned} \tag{6.18c}$$

$$\begin{aligned}\omega\tau_\phi^\star \int_\Omega \hat{n}^{(1)}_{Re}\psi_{Im}\,\mathrm{d}\tilde{A} &+ \int_\Omega \nabla\hat{\phi}^{(1)}_{Im}\cdot\nabla\psi_{Im}\,\mathrm{d}\tilde{A} + \cdots \\ &- \int_{\Gamma_5}\left(\tilde{A}_\phi\hat{n}^{(1)}_{Im} - \tilde{A}^C_\phi\hat{n}^{(1)}_{Re}\right)\psi_{Im}\,\mathrm{d}\tilde{x} = 0\end{aligned} \tag{6.18d}$$

with the additional conditions that:

$$\hat{\phi}^{(1)}_{Re} = 0 \qquad \& \qquad \hat{\phi}^{(1)}_{Im} = 0 \qquad \text{on} \qquad \Gamma_1, \tag{6.19a}$$

$$\hat{\phi}^{(1)}_{Re} = 1 \qquad \& \qquad \hat{\phi}^{(1)}_{Im} = 0 \qquad \text{on} \qquad \Gamma_4, \tag{6.19b}$$

and where the parameters $\tilde{C}_Q$, $\tilde{A}^C_\phi$ and A^C_n are given by the following expressions:

$$C_Q = 2\frac{D_{ion}}{l_c}\tilde{C}_Q, \tag{6.20a}$$

$$A^C_n = -\frac{C_0}{1+\frac{c^0_{eon}}{4c^0_{ion}}}\omega l_c \frac{1+4\frac{c^0_{ion}}{c^0_{eon}}\frac{D_{ion}}{D_{eon}}}{4c^0_{ion}D_{ion}}\frac{U_T}{e}, \tag{6.20b}$$

$$\tilde{A}^C_\phi = -\frac{C_0}{1+\frac{c^0_{eon}}{4c^0_{ion}}}\omega l_c \frac{1-\frac{D_{ion}}{D_{eon}}}{4c^0_{ion}D_{ion}}\frac{U_T}{e}. \tag{6.20c}$$

6.2 Discussion of the Results

The input parameters for the model are reported in Tab. 2.1. Two main input model parameters were systematically changed: the $\tilde{k}^0_f$ and the $\tilde{C}_Q$ defined in Eqn 6.20a. Unless it is otherwise specified, the horizontal length-scales of the sample W_1 and W_2 were fixed to the values 1.5 and 2.5μm respectively, while l_2, the thickness of the sample, was allowed to vary. The experimental data was taken from recent work of Chue and Haile [CH09].

6.2.1 Qualitative Considerations

We first ran the thin film model in the steady state regime $\omega = 0\ Hz$ in order to check for consistency with the intuitive flux configuration of figure 6.1. In figure 6.4 we report the results for $\tilde{k}^0_f = 10^{31}$ at $T = 650^oC$ and $\tilde{p}_{O_2} = 10^{-25}$ We note that the expected qualitative

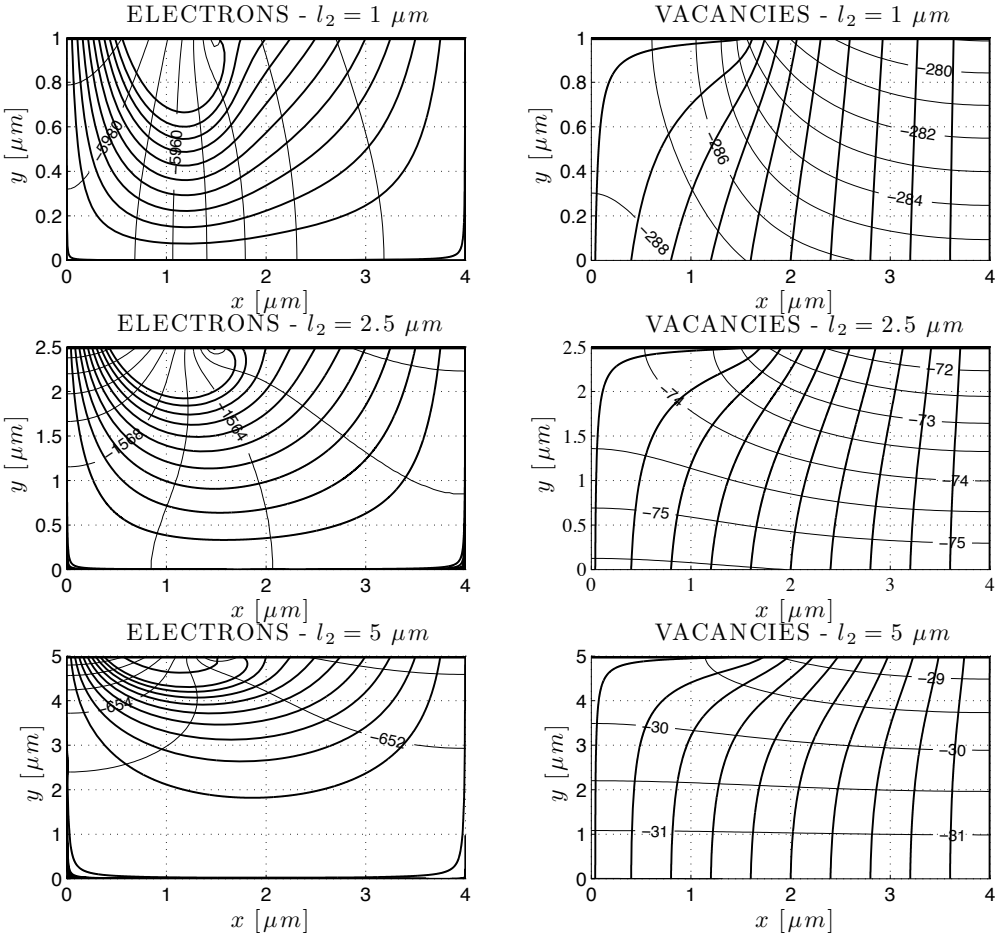

Figure 6.4: Computation of the equipotential lines in the thin film MIEC for $\tilde{k}_f^0 = 10^{31}$ at 650^oC and $\tilde{p}_{O_2} = 10^{-25}$, varying the film thickness: (left) The computed electron electrochemical potentials in the thin film MIEC. (right) The computed ionic electrochemical potentials.

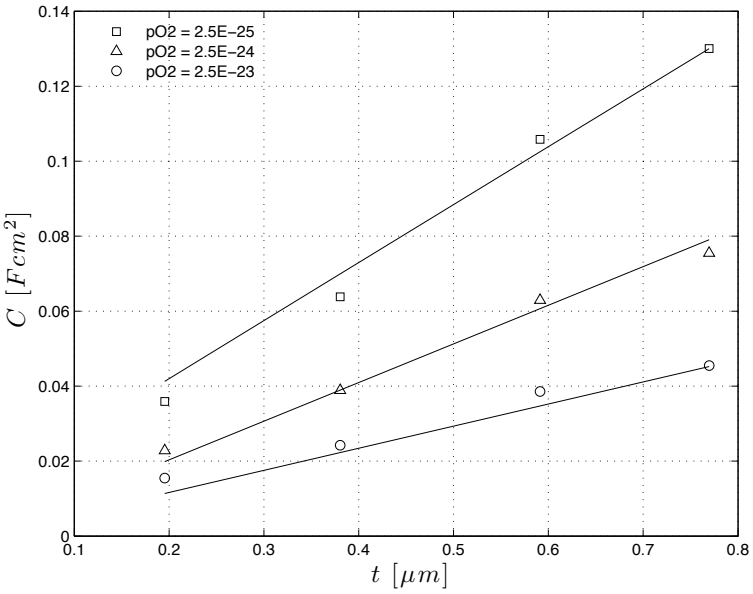

Figure 6.5: Total capacitance versus thickness at $T = 650^oC$, $\tilde{p}_{O_2} = 2.5 \times 10^{-25}$ 2.5×10^{-24} 2.5×10^{-23}, the solid lines are the computational results while the symbols are the experimental data of [CH09]

features are recovered, the electrons flow from the gas | Ceria interface onto the current collector while the ions move from the ionic conductor | Ceria interface through the mixed conductors to react with the species adsorbed on the surface. We remark also that by increasing the thickness of the sample the electron current lines change significantly while the vacancy current lines change very little. It is also interesting to note that, in the case where the thickness $l_2 = 5\mu m$, the vast majority of the electrons move from the gas up to 3 μm down into the MIEC; this hints that by increasing the thickness of the thin film, the active layer active might be limited to a few microns near the gas | Ceria surface in accordance with previous calculations.

6.2.2 Comparison with Experiments

For thin films of thickness of approximately $1\mu m$ we recover the result of Section 3.2.2 ($R_{eon} \approx R_{ion} \ll R_{surf}$ and $C_{chem} \approx C_{surf}$): the frequency response of the system under study fits well a resistor-capacitor circuit. Two-dimensional calculations against the experimental impedance ($T = 650^oC$ and the O_2 partial pressure is of the order of $10^{-25}atm$) are shown in figure 6.3 where the typical RC feature of the impedance are recovered. Also the location of the low frequency point in the Nyquist plot depends only on $\tilde{k}_f^0$. The capacitance of the thin film can also be fitted using this model, we show 2D computations and measured values of the capacitance in figure 6.5. By parametrically varying $\tilde{C}_Q$, we note that the capacitance plots move upward with increasing $\tilde{C}_Q$ indicating that the total capacitance of the sample is the sum of the surface capacitance (6.17b) and the one-dimensional chemical capacitance reported in Tab. 3.2. This linear dependence is valid for "low" $\tilde{k}_f^{(0)}$ (for fitted values $\tilde{k}_f^0 \approx 10^{31}$ we notice that the capacitive effects are additive). If chemical reactions are sufficiently fast, as shown in figure 6.7, then the deviations from the one-dimensional (additive or linear) behavior is more pronounced. This can be understood if we go back to the definition of Z_{surf}, (6.16), which shows that if k_f is big then the contribution of the capacitance decreases to the surface impedance increases, hereby shifting its behavior to a simple resistor for sufficiently small ω. Furthermore as k_f increases, we expect that the deviations from the one-dimensional behavior will be enhancing giving a non-linear correlation between total capacitance and injection rate.

6.2.3 Polarization Resistance

The study of the polarization resistance and its separation into a surface and a drift diffusion component is a key quantity that helps understand anodic polarization losses. It is thus

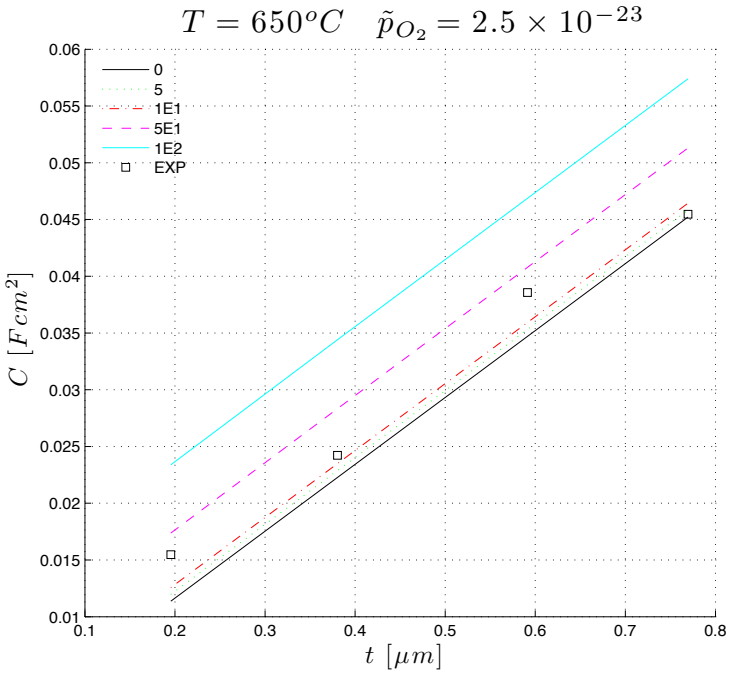

Figure 6.6: The capacitance of the Ceria thin film at $T = 650^oC$ and $\tilde{p}_{O_2} = 2.5 \times 10^{-23}$ and $\tilde{k}_f^0 = 5 \times 10^{31}$ as a function of thickness varying the interfacial capacitance parameter C_Q from 0 to 100.

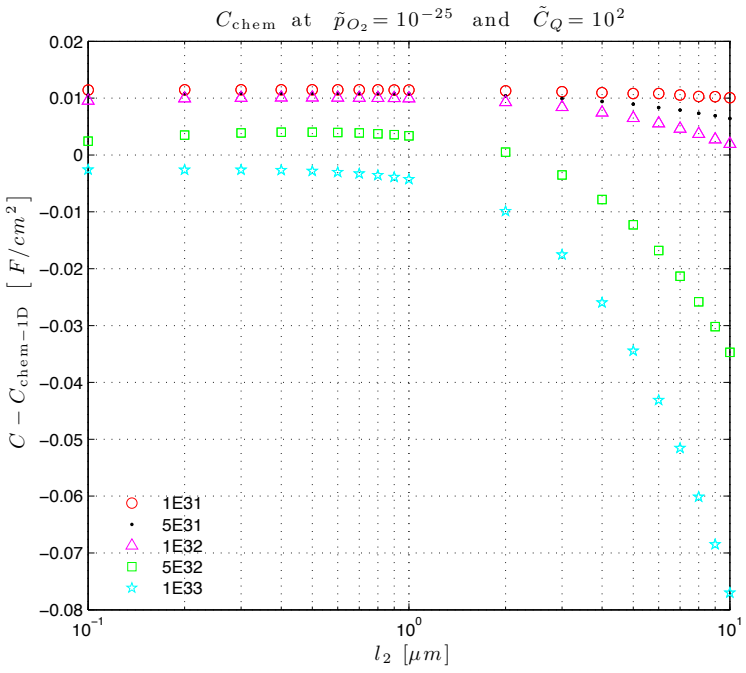

Figure 6.7: Difference between the thin film capacitance and the one-dimensional capacitance for a thin film of varying thickness at $T = 650^oC$ and $\tilde{p}_{O_2} = 10^{-25}$ with $\tilde{C}_Q = 10^2$.

interesting to plot f_{surf}, the ratio of the surface resistive losses to the total polarization losses, (4.12a), as a function of $\tilde{k}_f^0$ (or R_{surf}) for varying W_1 and W_2. We set $W_1 = W_2$ and we vary $W_1 = 2.5\mu m,\ 10\mu m,\ 80\mu m$. We report the results of the calculations in figure 6.8. One feature is most striking, as W_1 increases the f_{surf} decreases. Keeping the injection rate and $\frac{W_2}{W_1}$ fixed while varying W_1 will keep R_{surf} constant, (6.17a), and, at the same time, the distance that electrons need to travel in order to reach the metal current collector will increase, hereby increasing the drift-diffusion component of the polarization resistance. The latter in turn corresponds to a decrease of f_{surf}. The monotonically decreasing dependence of $R_{ion}^{\perp}$ with $\tilde{k}_f^0$ is also recovered. This is in accordance with the results of Chapter 3.

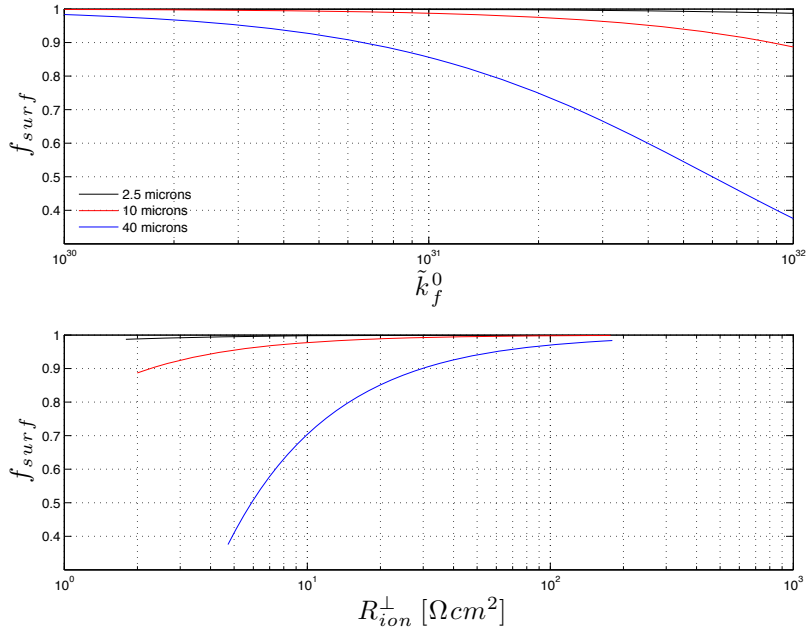

Figure 6.8: Plot of f_{surf} versus $\tilde{k}_f^0$ and $R_{ion}^{\perp}$ for $W_1 = W_2 = 2.5,\ 10,\ 40\mu m$ at $T = 650^oC$ and $\tilde{p}_{O_2} = 10^{-25}$. The fractional resistance decreases with increasing spacing W_1 while the R_{surf} is kept constant.

6.3 Extension of the Model to Cathode Materials

The model we have employed to study thin film Ceria electrodes can be extended to the study thin film cathodic materials in a circular symmetric configuration. Here we shall consider one system widely studied in Maier's group at Max Planck Institute in Stüttgart, the thin film Lanthanum Manganite (LSM- $(La_{0.8}Sr_{0.2})_{0.92}MnO_3$) Model Cathode [BMF08], [FBB$^+$06] [FKJM08].

The system studied consists of cylindrical LSM microelectrodes from 20 to 100μm diameter that are deposited on top of a YSZ substrate and a small current collector is placed on top of the microelectrodes (during impedance measurements the LSM is contacted with a tungsten-carbide tip whose diameter is around 4μm). Thus the configuration Fleig et al. [FKJM08] studied is very similar to the one studied here, however the materials' properties are entirely different. For instance, LSM conducts vacancies and holes, and the latter are the dominant conductive species. Hence LSM is characterized by a very high electronic conductivity and a fairly low ionic conductivity. Also LSM is a cathode material working under oxidizing atmosphere, thus its electrochemistry is entirely different from Ceria's. However the linear tools we have developed thus far can be applied, with minor modifications, to the study of LSM thin films. We shall focus on a cylindrical LSM thin film of thickness $l_2 = 250nm$, of radius W_2 of exactly 30μm and with a current collecting tip of radius $W_1 = 2\mu m$ which is perfectly centered with respect to the LSM. We suppose that the behavior of the LSM | gas interface is capacitive resistive and we consider as well that a double layer forms at the YSZ | LSM interface. The latter is characterized by a generalized capacitive behavior, having a CPE element response with characteristic $\alpha = 0.8$.

Equations (6.18) with the extra conditions given by (6.19) and a local CPE element

Table 6.1: Input data for the cathode model, the ionic conductivity is given by σ_{ion}, the surface RC behavior is described by an area specific resistance R_S and area specific capacitance C_S. The ionic concentration in given as a chemical capacitance via C_{chem} and Q_i is the generalized capacitance of the CPE element.

$T = 800^oC$	$\tilde{p}_{O_2} = 4 \times 10^{-5}$	$\tilde{p}_{O_2} = 1.5 \times 10^{-2}$
σ_{ion} $[\Omega^{-1}cm^{-1}]$	7.3×10^{-7}	6.37×10^{-8}
R_S $[\Omega cm^2]$	5.3×10^4	2.7×10^3
C_{chem} $[F/cm^2]$	5.5×10^{-4}	5.5×10^{-4}
C_S $[F/cm^2]$	7×10^{-4}	7×10^{-4}
Q_i $[F/cm^2]$	4.2×10^-5	4.2×10^{-5}

on Γ_1 are taken in cylindrical coordinates $(\tilde{r}, \tilde{y})$ such that $\mathrm{d}\tilde{x} = \tilde{r}\,\mathrm{d}\tilde{r}$ and $\mathrm{d}\tilde{A} = \tilde{r}\,\mathrm{d}\tilde{r}\,\mathrm{d}\tilde{y}$. We computed the impedance response of the system for the values in Tab. 6.1, taken from Fleig et al. [FKJM08]. We compare the cylindrical coordinate computations against the experimental results of [FKJM08] and find good qualitative agreement both at low and high frequency for various pressures, figures 6.9 and 6.10. This shows that the framework developed in this thesis can be also used to study cathodic materials and, to the author's knowledge, this work is first to compute the impedance response of a cathode mixed conductor.

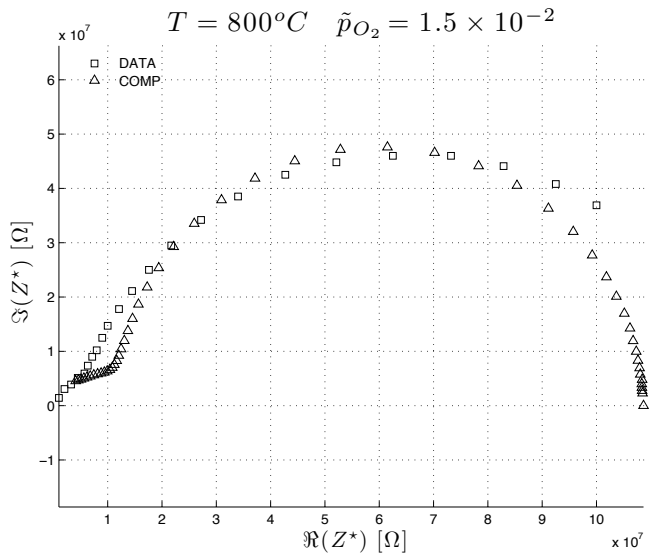

Figure 6.9: Impedance spectrum of the LSM thin film microelectrodes at 800 C for $\tilde{p}_{O_2} = 1.5 \times 10^{-2}$. The triangles indicate the computation while the squares indicate the data.

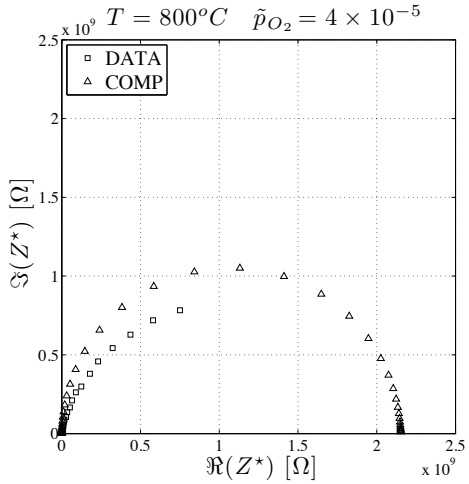

(a) Full impedance in coarse scale

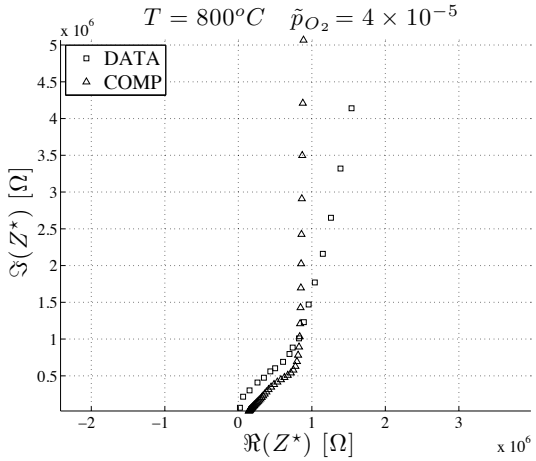

(b) Magnification of the high frequency part of the spectrum

Figure 6.10: Impedance spectrum of the LSM thin film microelectrodes at 800 C for $\tilde{p}_{O_2} = 4 \times 10^{-5}$. The triangles indicate the computation while the squares indicate the data of Fleig et al. [FKJM08]

Chapter 7

Conclusions

In this thesis we have derived a new way to analyze the impedance response of mixed conducting materials for use in fuel cells. Our main focus was the study new anodic materials, in particular doped cerium oxides, but we show that the approach presented in the thesis also works well for mixed conducting cathode.

First we have analyzed the impact of mixed conductivity coupled to electro-catalytic behavior in the linear time-independent domain for a thick ceria sample. We have derived that, for a promising fuel cell material, i.e., SDC-15, chemical reactions are the determining component of the polarization resistance. We have also have shown that first principle parameters, such as chemical reaction rates and diffusivities, can be connected in a fairly straightforward way to directly measurable electrochemical quantities, like resistances to ionic and electronic diffusion and area specific resistance. Finally, the results obtained match well the experimental results of Lai and Haile [LH05].

As a second step we have extended the previous model to the time dependent case, where we focused on single harmonic excitation, i.e., the impedance spectroscopy conditions. Again the computed results compare very well to experimental impedance spectra and some interesting physical phenomena can be understood using a 2D model. We show that the 1D equivalent circuit approximation is sufficiently accurate to fit data in the case of a

thick symmetric mixed conductor and, for the given conditions, the deviations from the 1D approximation are in general limited to the vicinity of the electroactive area. It is important to remark also that in the case of ceria if the aspect ratio (the ratio between thickness of the mixed conductor and the current collector length scale) drops below 10 the sample deviates significantly in the frequency domain from the 1D case. We confirm that for both harmonic and steady state excitation, the chemistry is rate limiting; however, as frequency increases, the chemistry dominance decreases. The impedance spectra model can be extended to the case where some input parameters are not uniform. For instance we considered the case where diffusivities change significantly in the vicinity of the electro-catalytic region. Again, we show that such effects impact very little the impedance spectra for the projected chemical reaction rates; if the chemical reactions are sufficiently fast compared to diffusive phenomena, such non-linearities could play an important rôle.

As a third and final step we extended the model to capture the two-dimensional behavior in thin films, where the aspect ration drops significantly and where the electrons' motion from one side of the sample to the other is impeded. Such conditions are similar to those encountered in fuel cells where an electrolyte conducting exclusively oxygen ions is placed between the anode and the cathode. Even though electronic transmission is not particularly fast in cerium oxide and the samples are geometrically two-dimensional (in this case the aspect ratio drops below unity), one-dimensional models still are likely to be valid and the effects influencing the most the polarization are always confined close to the interface for thickness comparable to current collector spacing length-scale. This is another strong indication that in order to improve the performance of cerium-based anodes one should work on enhancing the catalytic capability of the material. The framework developed was also extended to study a widely used cathode material, e.g. Lanthanum Strontium Manganite

(LSM), in the thin film setting. The calculations were compared to the work of Fleig et al. [FKJM08] on microelectrodes. Good agreement was achieved between numerical results and experimental work.

7.1 Ongoing Work

Our ongoing work features a few topics that were briefly addressed in the thesis, in particular:

- non-linear impedance spectroscopy;
- deconvolution of hydrogen electrochemistry of ceria using the thin film data.

Non-linear impedance spectroscopy (NLIS) could help deconvolve the chemistry of electroactive materials. The experimental work of to Wilson et al. [WSA06] is first to have shown the capability of NLIS as a tool for electrochemistry. Even though the techniques used in NLIS are seemingly a mere extension of the analysis in Appendix C, for a 1D a thick MIEC sample, there is no experimental work in support to cerium oxide NLIS computations. It is important to stress that due to the intrinsic non-linearity, this technique could help understand more physical phenomena than traditional impedance spectroscopy. In particular, we are currently attempting the deconvolution of plausible mechanistic models against the polarization resistance and capacitance data for the thin ceria samples and NLIS could help select the correct electro-chemical hydrogen reduction mechanism among all the plausible ones. It is key to stress that understanding chemistry of hydrogen on ceria could be extremely important for the future SOFC development and that this methodology could be extended to the study of other mixed conductors.

7.2 Future Work

The future work we propose will focus on understanding and optimizing fuel cell electrodes that are used in real industrial applications. Fuel cell electrodes are typically geometrically extremely complex and can be idealized as a collection of spherical elements of variable sizes having characteristic properties similar to the thin film systems studied here. In fact the characteristic length-scale is in the order of microns and their local behavior is typically linear or a few orders non-linear. However in real electrodes are strongly coupled with the gas-phase chemistry and diffusion of reacting species. Hence, the research presented in the thesis and the ongoing work could be used as the foundation for multi-particles models, such as the ones developed in Goodwin's group at Caltech, and it will help extend them to the interesting case of mixed conductors.

Classically, the effective properties are derived via averaging or homogenization. In particular homogenization [BLP78] replaces a micro and heterogenous system by one that macroscopically behaves in the same effective manner as the original. One of the goals of our future work is not only to develop complex multi-particle models but also to understand via analytical homogenization techniques the main properties of real world electrodes, possibly leading to their local optimization [All01]

Appendix A

Error Estimator and Refinement Strategy

The goal of this appendix is to find a weak residual estimator for the variational discretization of the problem (2.40). This approach is rather standard in numerical finite element methods [BS00]. We will set this error estimator in $H^1(\Omega) = W_2^1(\Omega) = \left\{ f \in L^1_{loc}(\Omega) : ||f||_{L_2} + ||\nabla f||_{L_2} \right\}$ where Ω is a polyhedral domain of $\mathbb{R}^2$ and it is where (2.40) is defined. Such error estimator will guarantee that the discretized solution is close to the exact solution in term of both $(\hat{n}, \hat{\phi})$ and its gradients $(\nabla\hat{n}, \nabla\hat{\phi})$ ensuring that both voltages and currents are correctly computed. We consider that the problem is discretized on a triangular mesh $\mathcal{T}_h$, where $T \in \mathcal{T}_h$ is a triangle of the mesh, we assume an edge of T is indicated by e. The approximation space is indicate by V_h which is the space of piecewise polynomials of degree k on $\mathcal{T}_h$.

We indicate the exact complex valued solution is $(\hat{n}, \hat{\phi}) \in H^1(\Omega)$, while the discretized solution is $(\hat{n}_h, \hat{\phi}_h) \in V_h$ and we choose the test functions $(m_h, \hat{\phi}_h) \in V_h$. We shall consider only the first equation in the system (2.40) and we recall that it satisfies

$$\begin{aligned} \omega\tau_n^\star \int_\Omega \hat{n}^{(1)}_{Im} m_{Re}\, \mathrm{d}\tilde{A} - \int_\Omega \nabla\hat{n}^{(1)}_{Re} \cdot \nabla m_{Re}\, \mathrm{d}\tilde{A} \quad &+ \quad \int_{\Gamma_5} \tilde{A}_n \hat{n}^{(1)}_{Re} m_{Re}\, \mathrm{d}\tilde{x} \\ &- \quad 4\frac{\bar{p}}{\bar{n}} \int_{\Gamma_4} \partial_{\tilde{y}} \hat{\phi}^{(1)}_{Re} m_{Re}\, \mathrm{d}\tilde{x} = 0 \end{aligned} \tag{A.1}$$

while the discretized problem satisfies

$$\begin{aligned} & \omega\tau_n^\star \int_\Omega \hat{n}^{(1)}_{Im,h} m_{Re,h}\,\mathrm{d}\tilde{A} - \int_\Omega \nabla \hat{n}^{(1)}_{Re,h}\cdot\nabla m_{Re,h}\,\mathrm{d}\tilde{A} \\ + & \int_{\Gamma_5} \tilde{A}_n \hat{n}^{(1)}_{Re,h} m_{Re,h}\,\mathrm{d}\tilde{x} - 4\frac{\bar{p}}{\bar{n}}\int_{\Gamma_4} \partial_{\tilde{y}}\hat{\phi}^{(1)}_{Re,h} m_{Re,h}\,\mathrm{d}\tilde{x} = 0 \end{aligned} \tag{A.2}$$

In general, a weak formulation can be written as $a(u,v)=0$ and its discretized version is $a(u_h,v_h)$ then we can recast the error formulation $e_h = u - u_h$ as $a(e_h, v = R(u_h,v)$ where R is the residual. The residual can be in general bound with $|R(e_h,e_h)| \leq ||R||_{H^{-1}}\,||e_h||_{H^1}$ (Hölder inequality), if the problem is coercive then $|a(e_h,e_h)| \geq \alpha_0\,||e_h||^2_{H^1}$ (a "weak" Gårding inequality can be used for systems of elliptic equations [Gia93]), using the last two we can get $||e_h||^2_{H^1} \leq C\,||R||_{H^{-1}}$. In order to bound the error, one can compute the H^{-1} norm of the residual R, a quantity that involves only the data of the problem and its approximation. Since the negative norm of a function is hard to compute, we will then need to find an appropriate approximation. The reminder of this appendix is devoted to this task.

In the ∞ dimensional case we can use m_h as test function so that the difference of (A.1) and (A.2) is given by

$$\begin{aligned} \omega\tau_n^\star \int_\Omega \left(\hat{n}^{(1)}_{Im} - \hat{n}^{(1)}_{Im,h}\right) m_{Re,h}\,\mathrm{d}\tilde{A} \quad & - \quad \int_\Omega \nabla\left(\hat{n}^{(1)}_{Re} - \hat{n}^{(1)}_{Re,h}\right)\cdot\nabla m_{Re,h}\,\mathrm{d}\tilde{A} \\ & + \quad \int_{\Gamma_5} \tilde{A}_n \left(\hat{n}^{(1)}_{Re} - \hat{n}^{(1)}_{Re,h}\right) m_{Re,h}\,\mathrm{d}\tilde{x} \\ & - \quad 4\frac{\bar{p}}{\bar{n}}\int_{\Gamma_4} \partial_{\tilde{y}}\left(\hat{\phi}^{(1)}_{Re} - \hat{\phi}^{(1)}_{Re,h}\right) m_{Re,h}\,\mathrm{d}\tilde{x} = 0 \end{aligned} \tag{A.3}$$

We now note that the term $\int_\Omega \nabla(\hat{n}_{Re} - \hat{n}_{Re,h}) \cdot \nabla m_{Re}$ can be rewritten using (A.3) as

$$\begin{aligned}\int_\Omega \nabla(\hat{n}_{Re} - \hat{n}_{Re,h}) \cdot \nabla m_{Re} &= \int_\Omega \nabla(\hat{n}_{Re} - \hat{n}_{Re,h}) \cdot \nabla(m_{Re} - m_{Re,h}) \\ &+ \omega\tau_n^\star \int_\Omega \left(\hat{n}_{Im}^{(1)} - \hat{n}_{Im,h}^{(1)}\right) m_{Re,h} \\ &+ \tilde{A}_n \int_{\Gamma_5} \left(\hat{n}_{Re}^{(1)} - \hat{n}_{Re,h}^{(1)}\right) m_{Re,h} \\ &- 4\frac{\bar{p}}{\bar{n}} \int_{\Gamma_4} \partial_{\tilde{y}} \left(\hat{\phi}_{Re}^{(1)} - \hat{\phi}_{Re,h}^{(1)}\right) m_{Re,h}.\end{aligned} \tag{A.4}$$

The function $(m_{Re} - m_{Re,h})$ is an admissible test function for the full ∞ dimensional problem, then it follows that

$$\begin{aligned}&\int_\Omega \nabla(\hat{n}_{Re} - \hat{n}_{Re,h}) \cdot \nabla m_{Re} = -\int_\Omega \nabla \hat{n}_{Re,h} \cdot \nabla(m_{Re} - m_{Re,h}) \\ &+ \omega\tau_n^\star \left[\int_\Omega \left(\hat{n}_{Im}^{(1)} - \hat{n}_{Im,h}^{(1)}\right) m_{Re,h} + \int_\Omega \hat{n}_{Im}^{(1)} (m - m_{Re,h})\right] \\ &+ \tilde{A}_n \left[\int_{\Gamma_5} \left(\hat{n}_{Re}^{(1)} - \hat{n}_{Re,h}^{(1)}\right) m_{Re,h} + \int_{\Gamma_5} \hat{n}_{Re}^{(1)} (m_{Re} - m_{Re,h})\right] \\ &- 4\frac{\bar{p}}{\bar{n}} \left[\int_{\Gamma_4} \partial_{\tilde{y}} \left(\hat{\phi}_{Re}^{(1)} - \hat{\phi}_{Re,h}^{(1)}\right) m_{Re,h} + \int_{\Gamma_4} \partial_{\tilde{y}} \hat{\phi}_{Re}^{(1)} (m_{Re} - m_{Re,h})\right].\end{aligned} \tag{A.5}$$

We also have that over a triangulation $\mathcal{T}_h$ that covers Ω with $T \in \mathcal{T}_h$ the following holds:

$$\begin{aligned}\int_\Omega \nabla \hat{n}_{Re,h} \cdot \nabla(m_{Re} - m_{Rr,h}) &= \sum_{T\in\mathcal{T}_h} \int_T \triangle \hat{n}_{Re,h}(m_{Re} - m_{Re,h}) \\ &- \sum_{T\in\mathcal{T}_h} \int_{\partial^+ T} \frac{\partial \hat{n}_{Re,h}}{\partial \mathbf{n}}(m_{Re} - m_{Re,h}) \\ &= \sum_{T\in\mathcal{T}_h} \int_T i\omega\tau_n^\star n_{Re,h}(m_{Re} - m_{Re,h}) \\ &- \sum_{T\in\mathcal{T}_h} \int_{\partial^+ T} \frac{\partial \hat{n}_{Re,h}}{\partial \mathbf{n}}(m_{Re} - m_{Re,h})\end{aligned} \tag{A.6}$$

We recall that the residual for the problem discussed here is then given by

$$\begin{aligned} r_{n_{Re}} &= \omega\tau_n^\star \int_\Omega \left(\hat{n}_{Im}^{(1)} - \hat{n}_{Im,h}^{(1)}\right) m_{Re} - \int_\Omega \nabla\left(\hat{n}_{Re}^{(1)} - \hat{n}_{Re,h}^{(1)}\right)\cdot\nabla m_{Re} \\ &+ \tilde{A}_n \int_{\Gamma_5} \left(\hat{n}_{Re}^{(1)} - \hat{n}_{Re,h}^{(1)}\right) m_{Re} - 4\frac{\bar{p}}{\bar{n}} \int_{\Gamma_4} \partial_{\tilde{y}} \left(\hat{\phi}_{Re}^{(1)} - \hat{\phi}_{Re,h}^{(1)}\right) m_{Re}\, \mathrm{d}\tilde{x}. \end{aligned} \tag{A.7}$$

Using the previous results we can deduce that over the triangulation $\mathcal{T}_h$

$$\begin{aligned} r_{n_{Re}} &= \int_\Omega \left(\triangle\hat{n}_{Re,h}^{(1)} - \omega\tau_n^\star \hat{n}_{Im,h}^{(1)}\right)(m_{Re} - m_{Re,h}) \\ &- \sum_{T\in\mathcal{T}_h} \int_{\partial^+ T\setminus\partial\Omega} \frac{\partial \hat{n}_{Re,h}^{(1)}}{\partial \mathbf{n}}(m_{Re} - m_{Re,h}) \\ &+ \int_{\partial\Gamma_5} \left(A_n n_{Re,h}^{(1)} - \partial_{\tilde{y}} n_{Re,h}^{(1)}\right)(m_{Re} - m_{Re,h}) \\ &+ \int_{\partial\Gamma_5} \left(\partial_{\tilde{y}} n_{Re}^{(1)} - 4\frac{\bar{p}}{\bar{n}}\partial_{\tilde{y}} n_{Re,h}^{(1)}\right)(m_{Re} - m_{Re,h}). \end{aligned} \tag{A.8}$$

Hence, the local residual $r_{n_{Re}}$ can be bounded using classical approximation theory as follows $|r_{n_{Re}}| \leq \sum_{T\in\mathcal{T}_h} \eta_{T,n_{Re}} = \eta_{n_{Re}}$. Each summation term in the latter can be expressed as

$$\begin{aligned} \eta_{T,\, n_{Re}} &= \int_T \left|\triangle\hat{n}_{Re,h}^{(1)} - \omega\tau_n^\star \hat{n}_{Im,h}^{(1)}\right| h^2 \\ &+ \left[\!\left[\frac{\partial \hat{n}_{Re,h}^{(1)}}{\partial \mathbf{n}}\right]\!\right]_T h_T^{1/2} \\ &+ \int_{\Gamma_5\cap T} \left|A_n \hat{n}_{Re,h}^{(1)} - \partial_{\tilde{y}} \hat{n}_{Re,h}^{(1)}\right| h^2 \\ &+ \int_{\Gamma_4\cap T} \left|\partial_{\tilde{y}} \hat{n}_{Re}^{(1)} - 4\frac{\bar{p}}{\bar{n}}\partial_{\tilde{y}} \hat{n}_{Re,h}^{(1)}\right| h^2 \\ &+ \int_{(\Gamma_2\cup\Gamma_3)\cap T} \left|\partial_{\tilde{x}} \hat{n}_{Re}^{(1)}\right| h^2 \end{aligned} \tag{A.9}$$

where $[\![\cdot]\!]$ is the jump across T, h is the length scale of T and h_T is the maximum side length of the triangle T. Similar residuals can be found for $n_{Im}^{(1)}$, $\phi_{Re}^{(1)}$, $\phi_{Im}^{(1)}$. Their sum $(\eta_{n_{Re}} + \eta_{n_{Im}} + \eta_{\phi_{Re}} + \eta_{\phi_{Im}})$ constitutes a reasonable error estimate and it is an upper bound for $(|\eta_{n_{Re}}| + |\eta_{n_{Im}}| + |\eta_{phi_{Re}}| + |\eta_{phi_{Im}}|)$ which is itself an upper bound for the variational error $a(u-u_h, v)$. The latter can be bounded from below by $a\|u\|_{L_2} - b\|\nabla u\|_{L_2}$ where a and

b are constants [Agm65]. So the sum $(\eta_{n_{Re}} + \eta_{n_{Im}} + \eta_{phi_{Re}} + \eta_{phi_{Im}})$ is a weak H^1 bound for the the solution of the problem.

A similar bound can be found for the general quasi-linear problem, for example, the $\eta_{T,\ n_{Re}}$ term can be written as

$$\begin{aligned}
\eta_{T,\ n_{Re}} &= \int_T \left| \nabla \cdot \left(a_{11} \nabla \hat{n}^{(1)}_{Re,h} + a_{12} \nabla \hat{\phi}^{(1)}_{Re,h} \right) - \omega \tau_n^\star \hat{n}^{(1)}_{Im,h} \right| h^2 \\
&+ \left[\!\!\left[a_{11} \frac{\partial \hat{n}^{(1)}_{Re,h}}{\partial \mathbf{n}} + a_{12} \frac{\partial \hat{\phi}^{(1)}_{Re,h}}{\partial \mathbf{n}} \right]\!\!\right] h_T^{1/2} \\
&+ \int_{\Gamma_5 \cap T} \left| \tilde{A}_{n,2} \hat{n}^{(1)}_{Re,h} - \partial_{\tilde{y}} \hat{n}^{(1)}_{Re,h} \right| h^2 + \int_{\Gamma_4 \cap T} \left| \partial_{\tilde{y}} \hat{n}^{(1)}_{Re} - 4 \frac{\bar{p}}{\bar{n}} \partial_{\tilde{y}} \hat{n}^{(1)}_{Re,h} \right| h^2 \\
&+ \int_{(\Gamma_2 \cup \Gamma_3) \cap T} \left| \partial_{\tilde{x}} \hat{n}^{(1)}_{Re} \right| h^2 .
\end{aligned} \tag{A.10}$$

Appendix B

Derivation of the Nonlinear Impedance Spectra Equations

We consider here the condition such that

1. the diffusivities vary through the system or that the activity changes through the sample;

2. the electroneutrality condition is enforced.

We shall start with the electro-neutral form of the drift-diffusion equations, where we assume that the diffusion coefficients normalized with respect to their bulk value $D_m^\star = D_m^{\mathrm{SURF}}/D_m^{\mathrm{BULK}}$:

$$\frac{\tau_n}{\tau}\partial_{\tilde{t}} n^{(1)} + \nabla_{\tilde{x}} \cdot \left(-D_{eon}^\star \left(\nabla_{\tilde{x}} n^{(1)} - \nabla_{\tilde{x}} \tilde{\phi}^{(1)}\right)\right) = 0, \tag{B.1a}$$

$$\frac{\bar{n}}{4\bar{p}}\frac{\tau_p}{\tau}\partial_{\tilde{t}} n^{(1)} + \nabla_{\tilde{x}} \cdot \left(-D_{ion}^\star \left(\frac{\bar{n}}{4\bar{p}}\nabla_{\tilde{x}} n^{(1)} + \nabla_{\tilde{x}} \tilde{\phi}^{(1)}\right)\right) = 0. \tag{B.1b}$$

We first sum the (B.1a) and (B.1b) and obtain

$$\left(\frac{\tau_n}{\tau} + \frac{\bar{n}}{4\bar{p}}\frac{\tau_p}{\tau}\right)\partial_{\tilde{t}} n^{(1)} + \nabla_{\tilde{x}} \cdot \left(-\left(D_{eon}^\star + \frac{\bar{n}}{4\bar{p}} D_{ion}^\star\right)\nabla_{\tilde{x}} n^{(1)} - \left(D_{ion}^\star - D_{eon}^\star\right)\nabla_{\tilde{x}} \tilde{\phi}^{(1)}\right) = 0. \tag{B.2}$$

Finally we multiply (B.1b) by $\frac{4\bar{p}}{\bar{n}}$ and sum to (B.1a):

$$\left(\frac{\tau_p}{\tau} - \frac{\tau_n}{\tau}\right)\partial_{\tilde{t}} n^{(1)} + \nabla_{\tilde{x}} \cdot \left(- \left(D^{\star}_{ion} - D^{\star}_{eon}\right) \nabla_{\tilde{x}} n^{(1)} - \left(D^{\star}_{eon} + \frac{4\bar{p}}{\bar{n}} D^{\star}_{ion} \right) \nabla_{\tilde{x}} \tilde{\phi}^{(1)} \right) = 0 \quad \text{(B.3)}$$

From (B.2) and (B.3), the equations (5.14) follow immediately and so do their coefficients given in (5.15).

Appendix C

Nonlinear Impedance Spectroscopy: a Perturbative Approach

We study here the regular expansion of Eqn.s 2.14 with $\alpha \to \infty$, i.e.,

$$\triangle_{\tilde{x}}\tilde{\phi} = \lambda^2 \left(1 + \bar{n}n - 2\bar{p}p\right), \tag{C.1a}$$

$$\frac{\tau_n}{\tau}\partial_{\tilde{t}} n + \nabla_{\tilde{x}} \cdot \left(n\nabla_{\tilde{x}}\tilde{\phi} - \nabla_{\tilde{x}} n\right) = 0, \tag{C.1b}$$

$$\frac{\tau_p}{\tau}\partial_{\tilde{t}} p - \nabla_{\tilde{x}} \cdot \left(2p\nabla_{\tilde{x}}\tilde{\phi} + \nabla_{\tilde{x}} p\right) = 0. \tag{C.1c}$$

We then derive a formal expansion in order to study the effects of a medium sized perturbation of the electric potential at the electrodes of a mixed conducting sample; we will take, with the usual convention

$$\tilde{\phi} = \tilde{\phi}^{(0)} + \tilde{\phi}^{(1)} + \ldots + \tilde{\phi}^{(k)} + \ldots, \tag{C.2a}$$

$$n = n^{(0)} + n^{(1)} + \ldots + n^{(k)} + \ldots, \tag{C.2b}$$

$$p = p^{(0)} + p^{(1)} + \ldots + p^{(k)} + \ldots. \tag{C.2c}$$

If we plug in the latter into the Eqn.s C.1 and obtain

$$\begin{aligned}
\triangle_{\tilde{x}}\tilde{\phi}^{(k)} &= \lambda^2\left(\bar{n}n^{(k)} - 2\bar{p}p^{(k)}\right), && \text{(C.3a)}\\
\frac{\tau_n}{\tau}\partial_{\tilde{t}}n^{(k)} &- \triangle n^{(k)} + \triangle\tilde{\phi}^{(k)} + \nabla\cdot\left(\sum_{k>l\in\mathbb{Z}^+} n^{(l)}\nabla\tilde{\phi}^{(k-l)}\right) = 0, && \text{(C.3b)}\\
\frac{\tau_p}{\tau}\partial_{\tilde{t}}p^{(k)} &- \triangle p^{(k)} - 2\triangle\tilde{\phi}^{(k)} - 2\nabla\cdot\left(\sum_{k>l\in\mathbb{Z}^+} p^{(l)}\nabla\tilde{\phi}^{(k-l)}\right) = 0. && \text{(C.3c)}
\end{aligned}$$

We then Fourier transform the equations above using the unitary convention

$$\begin{aligned}
\triangle_{\tilde{x}}\hat{\phi}^{(k)} &= \lambda^2\left(\bar{n}\hat{n}^{(k)} - 2\bar{p}\hat{p}^{(k)}\right), && \text{(C.4a)}\\
i\omega\tau_n\hat{n}^{(k)} &- \triangle\hat{n}^{(k)} + \triangle\hat{\phi}^{(k)} + \nabla\cdot\left(\sum_{k>l\in\mathbb{Z}^+} \hat{n}^{(l)} * \nabla\hat{\phi}^{(k-l)}\right) = 0, && \text{(C.4b)}\\
i\omega\tau_p\hat{p}^{(k)} &- \triangle\hat{p}^{(k)} - 2\triangle\hat{\phi}^{(k)} - 2\nabla\cdot\left(\sum_{k>l\in\mathbb{Z}^+} \hat{p}^{(l)} * \nabla\hat{\phi}^{(k-l)}\right) = 0, && \text{(C.4c)}
\end{aligned}$$

where $*$ indicates the convolution [Fol09]. We specialize (C.4) to the 1D case; it will transform (C.4) as follows:

$$\begin{aligned}
\frac{d^2\hat{\phi}^{(k)}}{d\tilde{x}^2} &= \lambda^2\left(\bar{n}\hat{n}^{(k)} - 2\bar{p}\hat{p}^{(k)}\right), && \text{(C.5a)}\\
i\omega\tau_n\hat{n}^{(k)} &- \frac{d^2\hat{n}^{(k)}}{d\tilde{x}^2} + \frac{d^2\hat{\phi}^{(k)}}{d\tilde{x}^2} + \frac{d}{d\tilde{x}}\left(\sum_{k>l\in\mathbb{Z}^+} \hat{n}^{(l)} * \frac{d\hat{\phi}^{(k-l)}}{d\tilde{x}}\right) = 0, && \text{(C.5b)}\\
i\omega\tau_p\hat{p}^{(k)} &- \frac{d^2\hat{p}^{(k)}}{d\tilde{x}^2} - 2\frac{d^2\hat{\phi}^{(k)}}{d\tilde{x}^2} - 2\frac{d}{d\tilde{x}}\left(\sum_{k>l\in\mathbb{Z}^+} \hat{p}^{(l)} * \frac{d\hat{\phi}^{(k-l)}}{d\tilde{x}}\right) = 0, && \text{(C.5c)}
\end{aligned}$$

In order to keep the algebraic manipulations simple we choose the case such that $\tilde{\phi}(0) = n(0) = p(0) = 0$. In frequency space the latter can be rewritten as $\hat{\phi}^{(k)}(0) = \hat{n}^{(k)}(0) = \hat{p}^{(k)}(0) = 0$. We shall also consider that potential is given by a single harmonic $\tilde{\phi}^{(1)}(l) = \frac{1}{\sqrt{2\pi}} e^{i\omega_0 \tau \tilde{t}}$ so its Fourier transform is $\hat{\phi}^{(1)}(l) = \delta(\omega - \omega_0)$ and in turn $\hat{\phi}^{(k)}, \hat{n}^{(k)}, p^{(k)} \propto \delta(\omega - k\omega_0)$. Hence, the terms $\sum_{k>m\in\mathbb{Z}^+} \hat{p}^{(m)} * \frac{d\hat{\phi}^{(k-m)}}{d\tilde{x}} \propto \delta(\omega - k\omega_0)$ are harmonics of order k. We solve (C.5) with the condition $\hat{\phi}^{(1)}(l) = 1$ and with $\phi^{(k)}(l) = 0$ and we remark that the remaining boundary condition on $n^{(k)}$ and $p^{(k)}$ are conditions on their fluxes. Thus we will need to solve at order k, the following three equations need to be solved:

$$\frac{d^2\hat{\phi}^{(k)}}{d\tilde{x}^2} = \lambda^2 \left(\bar{n}\hat{n}^{(k)} - 2\bar{p}\hat{p}^{(k)} \right), \tag{C.6a}$$

$$ik\omega_0\tau_n\hat{n}^{(k)} - \frac{d^2\hat{n}^{(k)}}{d\tilde{x}^2} + \frac{d^2\hat{\phi}^{(k)}}{d\tilde{x}^2} + \frac{d\gamma_n^{(k)}}{d\tilde{x}} = 0, \tag{C.6b}$$

$$ik\omega_0\tau_p\hat{p}^{(k)} - \frac{d^2\hat{p}^{(k)}}{d\tilde{x}^2} - 2\frac{d^2\hat{\phi}^{(k)}}{d\tilde{x}^2} - 2\frac{d\gamma_p^{(k)}}{d\tilde{x}} = 0, \tag{C.6c}$$

with the appropriate conditions and with the following definition of the γ_k's:

$$\gamma_n^{(k)} = \left(\sum_{k>m\in\mathbb{Z}^+} \hat{n}^{(m)} \frac{d\hat{\phi}^{(k-m)}}{d\tilde{x}} \right), \tag{C.7}$$

$$\gamma_p^{(k)} = \left(\sum_{k>m\in\mathbb{Z}^+} \hat{p}^{(m)} \frac{d\hat{\phi}^{(k-m)}}{d\tilde{x}} \right). \tag{C.8}$$

If we define $\mathbf{u}^{(k)} = \left(\hat{\phi}^{(k)}, \frac{d\hat{\phi}^{(k)}}{d\tilde{x}}, \hat{n}^{(k)}, \frac{d\hat{n}^{(k)}}{d\tilde{x}}, \hat{p}^{(k)}, \frac{d\hat{p}^{(k)}}{d\tilde{x}} \right)$, we can write(C.6) in compact form as follows:

$$\dot{\mathbf{u}}^{(1)} = A(\omega_0)\ \mathbf{u}^{(1)}, \tag{C.9a}$$

$$\dot{\mathbf{u}}^{(2)} = A(2\omega_0)\ \mathbf{u}^{(2)} + \mathbf{b}_2(\tilde{x}, \omega), \tag{C.9b}$$

$$\cdots \quad , \tag{C.9c}$$

$$\dot{\mathbf{u}}^{(k)} = A(k\omega_0)\ \mathbf{u}^{(k)} + \mathbf{b}_k(\tilde{x}, \omega), \tag{C.9d}$$

where the $A(\omega) : \mathbb{R} \to \mathbb{C}^{6\times 6}$ is given by

$$A(\omega) = M + i\omega K, \tag{C.10}$$

$\mathbf{b}_k$ is given by the summation above and is dependent on $\mathbf{u}^{(k-1)}, \mathbf{u}^{(k-2)}, \ldots, \mathbf{u}^{(1)}$. specifically, we will have

$$\mathbf{b}(k) = \begin{pmatrix} 0 \\ 0 \\ 0 \\ \gamma_n^{(k)} \\ 0 \\ -2\gamma_p^{(k)} \end{pmatrix}. \tag{C.11}$$

The matrices K and M can be written as follows ($\alpha_n = \lambda^2\bar{n}$, $\alpha_p = -2\lambda^2\bar{p}$):

$$M = \begin{pmatrix} 0 & 1 & 0 & 0 & 0 & 0 \\ 0 & 0 & \alpha_n & 0 & -\alpha_p & 0 \\ 0 & 0 & 0 & 1 & 0 & 0 \\ 0 & 0 & \alpha_n & 0 & -\alpha_p & 0 \\ 0 & 0 & 0 & 0 & 0 & 1 \\ 0 & 0 & -2\alpha_n & 0 & 2\alpha_p & 0 \end{pmatrix}, \quad K = \begin{pmatrix} 0 & 0 & 0 & 0 & 0 & 0 \\ 0 & 0 & 0 & 0 & 0 & 0 \\ 0 & 0 & 0 & 0 & 0 & 0 \\ 0 & 0 & \tau_n & 0 & 0 & 0 \\ 0 & 0 & 0 & 0 & 0 & 0 \\ 0 & 0 & 0 & 0 & \tau_p & 0 \end{pmatrix}. \tag{C.12}$$

It is elementary to notice that the closed form solution of (C.9) is then given by the following cascade of equations:

$$\mathbf{u}^{(k)}(\tilde{x},\omega) = e^{A(k\omega)\tilde{x}} \left\{ \mathbf{u}^{(k)}(0,\omega) + \int_0^{\tilde{x}} e^{-A(k\omega)x'} \mathbf{b}_k(x',\omega)\,\mathrm{d}x' \right\}, \tag{C.13}$$

where $\mathbf{u}^{(k)}(0,\omega)$ is determined by the boundary conditions. If we enforce electroneutrality, i.e. $\bar{n}n^{(k)} = 2\bar{p}p^{(k)}$, we recover at first order the IS equations whose 1D solution is given in Eqn.s 2.42. It is clear that the kth order, electroneutral, homogeneous problem is such that one eigenvalue is zero and twice degenerate while the other two are such $|\lambda_k| \propto \sqrt{k\omega_0}$.

C.1 Linearization of the Chemical Boundary Conditions

We will now study the linear dynamics of chemical reactions, we will start from an equilibrium condition and then look at the small order harmonic perturbations. The objective of the section is to prove that a Chang-Jaffé boundary condition fully describe the DC characteristic of the response of surfaces. In general the following holds at the exposed surface

if there is no diffusion

$$\frac{d\boldsymbol{\theta}}{dt} = g_f\left(\boldsymbol{\theta}, c_{eon}, \mathbf{D}\cdot\mathbf{e}_n, \tilde{p}_{H_2}, \tilde{p}_{H_2O}\right) - g_b\left(\boldsymbol{\theta}, c_{eon}, \mathbf{D}\cdot\mathbf{e}_n, \tilde{p}_{H_2}, \tilde{p}_{H_2O}\right), \tag{C.14}$$

at 0th order (superscript (0)) under steady state condition the (C.14) can be written as

$$0 = \frac{d\boldsymbol{\theta}^{(0)}}{dt} = g_f\left(\boldsymbol{\theta}, c_{eon}^{(0)}, \mathbf{D}\cdot\mathbf{e}_n, \tilde{p}_{H_2}, \tilde{p}_{H_2O}\right) - g_b\left(\boldsymbol{\theta}, c_{eon}^{(0)}, \mathbf{D}\cdot\mathbf{e}_n, \tilde{p}_{H_2}, \tilde{p}_{H_2O}\right). \tag{C.15}$$

If we assume that there is no dependence on the electric field $\mathbf{D}\cdot\mathbf{e}_n$ we will have that

$$\begin{aligned} \boldsymbol{\theta}^{(0)} &= \boldsymbol{f}_{\boldsymbol{\theta}}\left(\tilde{p}_{H_2}, \tilde{p}_{H_2O}\right), \\ c_{eon}^{(0)} &= f_{eon}\left(\tilde{p}_{H_2}, \tilde{p}_{H_2O}\right). \end{aligned} \tag{C.16}$$

Linearization of (C.14) leads to the following expression:

$$\frac{d\boldsymbol{\theta}^{(1)}}{dt} = J_{\boldsymbol{\theta}\boldsymbol{\theta}}\boldsymbol{\theta}^{(1)} + J_{\boldsymbol{\theta}n}c_{eon}^{(1)} + J_{\boldsymbol{\theta}D}D, \tag{C.17}$$

where we indicate Jacobians or gradients with the capital letter J; $J_{\boldsymbol{\theta}\boldsymbol{\theta}} = \frac{\partial}{\partial\boldsymbol{\theta}}\left(\boldsymbol{g}_f - \boldsymbol{g}_b\right)$ is an $n \times n$ real matrix, $J_{\boldsymbol{\theta}n} = \frac{\partial}{\partial c_{eon}}\left(\boldsymbol{g}_f - \boldsymbol{g}_b\right)$ and $J_{\boldsymbol{\theta}D} = \frac{\partial}{\partial D_n}\left(\boldsymbol{g}_f - \boldsymbol{g}_b\right)$ are two vectors in $\mathbb{R}^n$. The Fourier transform of the coverages is

$$\hat{\theta}^{(1)} = \left(J_{\boldsymbol{\theta}\boldsymbol{\theta}} - i\omega Id\right)^{-1}\left[J_{\boldsymbol{\theta}n}\hat{c}_{eon}^{(1)} + J_{\boldsymbol{\theta}D}\hat{D}\right]. \tag{C.18}$$

If we suppose that the vector $J_{\boldsymbol{\theta}D_n} = 0$ (no field contribution) and we consider only steady state conditions, we will get that

$$\boldsymbol{\theta}^{(1)} = -\left(J_{\boldsymbol{\theta}\boldsymbol{\theta}}\right)^{-1}J_{\boldsymbol{\theta}n}c_{eon}^{(1)}. \tag{C.19}$$

the boundary condition on Γ_5 reads at steady state

$$-\dot{\omega}_{eon} = J_{n\boldsymbol{\theta}}\theta^{(1)} + J_{nn}c_{eon}^{(1)} = \left[-J_{n\boldsymbol{\theta}}\left(J_{\boldsymbol{\theta}\boldsymbol{\theta}}\right)^{-1}J_{\boldsymbol{\theta}n} + J_{nn}\right]c_{eon}^{(1)}, \tag{C.20}$$

where the prefactor of $c_{eon}^{(1)}$ is a function of $\tilde{p}_{H_2}$ and $\tilde{p}_{H_2O}$. This justifies the use of Chang-Jaffé boundary conditions at Γ_5 if $\omega = 0$.

Bibliography

[AF03] R.A. Adams and J. Fournier. *Sobolev Spaces.* Academic Press, New York, Second edition, 2003.

[Agm65] S. Agmon. *Lectures on Elliptic Boundary Value Problems.* A Van Nonstrand Mathematical Study. D. Van Nonstrand Company, 1965.

[AH97] R.D. Armstrong and B.R. Horrocks. The Double Layer Structure at the Metal-Solid Electrolyte Onterface. *Solid State Ionics*, 94:181–187(7), 1997.

[AHW+00] S.B. Adler, B.T. Henderson, M.A. Wilson, D.M. Taylor, and R.E. Richards. Reference Electrode Placement and Seals in Electrochemical Oxygen Generators. *Solid State Ionics*, 134(1-2):35 – 42, 2000.

[All01] G. Allaire. *Shape Optimization By the Homogenization Method.* Springer, 2001.

[ALS96] S.B. Adler, J.A. Lane, and B.C.H. Steele. Electrode Kinetics of Porous Mixed-Conducting Oxygen Electrodes. *Journal of the Electrochemical Society*, 143(11):3564, 1996.

[AOGR92] P. Agarwal, M.E. Orazem, and L.H. Garcia-Rubio. Measurement Models for Electrochemical Impedance Spectroscopy. *Journal of The Electrochemical Society*, 139(7):1917–1927, 1992.

[ASS+06] D.A. Andersson, S.I. Simak, N.V. Skorodumova, I.A. Abrikosov, and B. Johansson. Optimization of ionic conductivity in doped ceria. *Proceedings of the National Academy of Sciences of the United States of America*, 103(10):3518–3521, 2006.

[BD49] R. Bott and R. J. Duffin. Impedance Synthesis without Use of Transformers. *Journal of Applied Physics*, 20(8):816–816, 1949.

[Bes07] W.G. Bessler. Rapid Impedance Modeling via Potential Step and Current Relaxation Simulations. *Journal of The Electrochemical Society*, 154(11):B1186–B1191, 2007.

[BIG03] A. Ben-Israel and N.E. Greville. *Generalized Inverses: Theory and Applications*. Springer, Second edition, 2003.

[Bis02] J. Bisquert. Theory of the Impedance of Electron Diffusion and Recombination in a Thin Layer. *The Journal of Physical Chemistry B*, 106(2):325–333, 2002.

[BLP78] A. Bensoussan, J.L. Lions, and G. Papanicolau. *Asymptotic Methods in Periodic Media*. North Holland, 1978.

[BM05] E. Barsoukov and J.R. Macdonald, editors. *Impedance Spectroscopy: Theory, Experiment, and Applications*. Wiley and Sons, New York, 2005.

[BMF08] F. S. Baumann, J. Maier, and J. Fleig. The Polarization Resistance of Mixed Conducting SOFC Cathodes: A Comparative Study using Thin Film Model Electrodes. *Solid State Ionics*, 179(21-26):1198–1204, SEP 15 2008.

[Bou95] B.A. Boukamp. A Linear Kronig-Kramers Transform Test for Immittance Data Validation. *Journal of The Electrochemical Society*, 142(6):1885–1894, 1995.

[BP37] E. Baur and H. Preis. *Zeitschrift für Elektrochemie*, 43:727, 1937.

[BS00] S.C. Brenner and L.G. Scott. *The Mathematical Theory of Finite Element Methods*, volume 15 of *Applied Mathematical Sciences*. Springer-Verlag, First edition, 2000.

[BSBR06] S.L. Bogart, K. Schulz, L. Brown, and B. Russ. Production of Liquid Synthetic Hydrocarbon Fuels From Air, Water, and Nuclear Power on Ships and at Shore Bases for Military Use. In *International Congress on Advances in Nuclear Power Plants*, Reno, NV, 2006.

[BvD70] A. J. Bosman and H. J. van Daal. Small-polaron versus band conduction in some transition-metal oxides. *Advances in Physics*, 19(77):1 – 117, 1970.

[CG07] F. Ciucci and D.G. Goodwin. Non-Linear Modeling of Mixed Ionic Electronic Conductors. *SOFC X*, 2(9):2027–2037, 2007.

[CH09] W.C. Chueh and S.M.. Haile. *Physical Review Letters*, 2009.

[CJ52] H.C. Chang and G. Jaffé. Polarization in Electrolytic Solutions 1. Theory. *Journal of Chemical Physics*, 20(7):1071–1077, 1952.

[CKC00] B. Corry, S. Kuyucak, and S.-H. Chung. Tests of Continuum Theories as Models of Ion Channels. II. Poisson-Nernst-Planck Theory versus Brownian Dynamics. *Biophysical Journal*, 78(5):2364 – 2381, 2000.

[CLH08] W.C. Chueh, W. Lai, and S.M. Haile. Electrochemical Behavior of Ceria with Selected Metal Electrodes. *Solid State Ionics*, 179(21-26):1036–1041, SEP 15 2008.

[CW51] H.B. Callen and T.A. Welton. Irreversibility and Generalized Noise. *Physical Review*, 83(1):34–40, Jul 1951.

[CWHG09] F. Ciucci, Chue W.C., S.M. Haile, and D.G. Goodwin. Two-Dimensional Electrochemical Model for Mixed Conductors: a Study of Ceria. *Physical Chemistry Chemical Physics*, 2009.

[Dav04] T.A. Davis. Algorithm 832: UMFPACK V4.3—an unsymmetric-pattern multifrontal method. *ACM Transactions Mathematical Software*, 30(2):196–199, 2004.

[DGM84] S.R. De Groot and P. Mazur. *Non-Equilibrium Thermodynamics*. Dover, 1984.

[DS98] N.R. Draper and H. Smith. *Applied Regression Analysis*. Wiley-Interscience, Third edition, 1998.

[FBB+06] J. Fleig, F. S. Baumann, V. Brichzin, H. R. Kim, J. Jamnik, G. Cristiani, H. U. Habermeier, and J. Maier. Thin film microelectrodes in sofc electrode research. *FUEL CELLS*, 6(3-4):284–292, JUL 2006.

[Fic65] G. Fichera. *Linear Elliptic Differential Systems and Eigenvalue Problems*, volume 8 of *Lecture Notes in Mathematics*. Springer-Verlag, 1965.

[FKJM08] J. Fleig, H.R. Kim, J. Jamnik, and J. Maier. Oxygen Reduction Kinetics of Lanthanum Manganite (LSM) Model Cathodes: Partial Pressure Dependence and Rate-Limiting Steps. *Fuel Cells*, 8(5):330–337, 2008.

[Fle04] J. Fleig. Impedance Spectroscopy on Solids: The Limits of Serial Equivalent Circuit Models. *Journal of Electroceramics*, 13:637–644(8), 2004.

[Fle05] J. Fleig. On the Current-Voltage Characteristics of Charge Transfer Reactions at Mixed Conducting Electrodes on Solid Electrolytes . *Physical Chemistry Chemical Physics*, 7(9):2027–2037, 2005.

[FMM07] J. Fleig, R. Merkle, and J. Maier. The p(o-2) dependence of oxygen surface coverage and exchange current density of mixed conducting oxide electrodes: model considerations. *PHYSICAL CHEMISTRY CHEMICAL PHYSICS*, 9(21):2713–2723, JUN 7 2007.

[Fol09] G.B. Folland. *Fourier Analysis and Its Applications*. Pure and Applied Undergraduate Texts. American Mathematical Society, 2009.

[Gia93] M. Giaquinta. *Introduction to Regularity Theory for Nonlinear Elliptic Systems*. Lecture Series-ETH Zürich. Birkäser, 1993.

[Goo06] D.G. Goodwin. *SOFC IX*, 2(9):2027–2037, 2006.

[HA99] B.R. Horrocks and R.D. Armstrong. Discreteness of Charge Effects on the Double Layer Structure at the Metal/Solid Electrolyte Interface. *The Journal of Physical Chemistry B*, 103(51):11332–11338, 1999.

[Hen01] M. Hendriks. *Solid state supercapacitors - Based on metal/yttria-stabelised zirconia composites*. PhD in inorganic materials science, University of Twente, 2001.

[HJBSM07] A. Hauch, S.H. Jensen, J.B. Bilde-Sorensen, and M. Mogensen. Silica Segregation in the Ni/YSZ Electrode. *Journal of The Electrochemical Society*, 154(7):A619–A626, 2007.

[Hol59a] T. Holstein. Studies of Polaron Motion Part I. The Molecular-Crystal Model. *Annals of Physics*, 8(3):325–342, 1959.

[Hol59b] T. Holstein. Studies of Polaron Motion Part II. The Small Polaron . *Annals of Physics*, 8(3):343–389, 1959.

[HP07a] B. Hallouet and R. Pelster. 3d-simulation of topology-induced changes of effective permeability and permittivity in composite materials. *Journal of Nanomaterials*, 2007(1):8–8, 2007.

[HP07b] F. Hecht and O. Pironneau. *FreeFem++*. Universite Pierre et Marie Curie, 2007. on the web at `http://www.freefem.org/ff++/ftp/freefem++doc.pdf`.

[Jam03] J. Jamnik. Impedance Spectroscopy of Mixed Conductors with Semi-Blocking Boundaries. *Solid State Ionics*, 157(1-4):19–28, FEB 2003.

[JM01] J. Jamnik and J. Maier. Generalised Equivalent Circuits for Mass and Charge Transport: Chemical Capacitance and its Implications. *Physical Chemistry Chemical Physics*, 3(9):1668–1678, 2001.

[JMP99] J. Jamnik, J. Maier, and S. Pejovnik. A Powerful Electrical Network Model for the Impedance of Mixed Conductors. *Electrochimica Acta*, 44(24):4139 – 4145, 1999.

[Kad63] L.P. Kadanoff. Boltzmann Equation for Polarons. *Physical Review*, 130(4):1364–1369, May 1963.

[Kru09] P. Krugman. Empire of Carbon. *New York Times*, 2009.

[KST06] A.A. Kilbas, H.M. Srivastava, and J.J. Trujillo. *Theory and applications of fractional differential equations*. Elsevier, First edition, 2006.

[Kub66] R. Kubo. The Fluctuation-Dissipation Theorem. *Reports on Progress in Physics*, 29(1):255–284, 1966.

[KV56] F.A. Kröger and H.J. Vink. Relations Between the Concentrations of Imperfections in Crystalline Solids. *Solid State Physics-Advances in Research and Applications*, 3:307–435, 1956.

[KZG05] R.J. Kee, H. Zhu, and D.G. Goodwin. Solid-oxide fuel cells with hydrocarbon fuels. *Proceedings of the Combustion Institute*, 30:2379–2404, January 2005.

[Lai07] W. Lai. *Impedance Spectroscopy as a Tool for the Electrochemical Study of Mixed Conducting Ceria*. PhD thesis, California Institute of Technology, 2007.

[LH05] W. Lai and S.M. Haile. Impedance Spectroscopy as a Tool for Chemical and Electrochemical Analysis of Mixed Conductors: a Case Study of Ceria. *Journal of the American Ceramic Society*, 88(11):2979–2997, NOV 2005.

[LH08] W. Lai and S.M. Haile. Electrochemical Impedance Spectroscopy of Mixed Conductors under a Chemical Potential Gradient: a Case Study of Pt—SDC—BSCF. *Physical Chemistry Chemical Physics*, 10(6):865–883, 2008.

[LN06] N.S. Lewis and D.G. Nocera. Powering the planet: Chemical challenges in solar energy utilization. *Proceedings of the National Academy of Sciences*, 103(43):15729–15735, 2006.

[Mac73] J.R. Macdonald. Theory of space-charge polarization and electrode-discharge effects. *The Journal of Chemical Physics*, 58(11):4982–5001, 1973.

[Mai04] J. Maier. *Physical Chemistry of Ionic Materials: Ions and Electrons in Solids*. John Wiley and Sons, 2004.

[MLL07] D.S. Mebane, Y. Liu, and M. Liu. A Two-Dimensional Model and Numerical Treatment for Mixed Conducting Thin Films. *Journal of The Electrochemical Society*, 154(5):A421–A426, 2007.

[MST00] M. Mogensen, N.M. Sammes, and G.A. Tompsett. Physical, Chemical and Electrochemical Properties of Pure and Doped Ceria. *Solid State Ionics*, 129(1-4):63 – 94, 2000.

[oE09] Department of Energy. Wind and Hydropower Technologies Program, 2009.

[Pri61] I. Prigogine. *Thermodynamics of Irreversible Processes*. Interscience, New York, Second edition, 1961.

[PVG00] S. Park, J.M. Vohs, and R.J. Gorte. Direct Oxidation of Hydrocarbons in a Solid-Oxide Fuel Cell. *Nature*, 404(6775):265–267, 2000.

[QV94] A. Quarteroni and A Valli. *Numerical Approximation of Partial Differential Equations*. Springer Series in Computational Mathematics. Springer-Verlag, New York, First edition, 1994.

[RW00] E. H. Rhoderick and R. H. Williams. *Metal-Semiconductor Contacts*. Monographs in Electrical & Electronic Engineering. Oxford University Press, Oxford, Second edition, 2000.

[SFK+05] V. A. Sadykov, Yu. V. Frolova, V. V. Kriventsov, D. I. Kochubei, E. M. Moroz, D. A. Zyuzin, Yu. V. Potapova, V. S. Muzykantov, V. I. Zaikovskii, E. B. Burgina, H. Borchert, S. N. Trukhan, V. P. Ivanov, S. Neophytides, E. Kemnitz, and K. K. Scheurell. Specificity of the Local Structure of Nanocrystalline Doped

Ceria Solid Electrolytes. *Material Research Society Symposium Proceedings*, K3.6:835, 2005.

[SK03] S.C. Singhal and K. Kendall. *High Temperature Solid Oxide Fuel Cells: Fundamentals, Design, and Applicatons.* Elsevier, 2003.

[Spa70] H.S. Spacil. Electrical Device Including Nickel-Containing Stabilized Zirconia Electrode. US Patent 3,558,360, 1970.

[Sze81] S.M. Sze. *Physics of Semiconductor Devices.* Wiley-Interscience, New York, Second edition, 1981.

[TN75] H.L. Tuller and A.S. Nowick. Doped Ceria as a Solid Oxide Electrolyte. *Journal of the Electrochemical Society*, 122(2):255–259, 1975.

[Tro01] A. Trovarelli, editor. *Catalysis by Ceria and Related Materials*, volume 2 of *Catalytic Science Series.* Imperial College Press, London, 2001.

[VK07] N.G. Van Kampen. *Stochastic Processes in Physics and Chemistry.* North Holland, Third edition, 2007.

[Vla99] V. Vlachy. Ionic Effects Beyond Poisson-Boltzmann Theory. *Annual Review of Physical Chemistry*, 50(1):145–165, 1999.

[WHB03] M. F. Wilkes, P. Hayden, and A. K. Bhattacharya. Surface segregation of lanthanum and cerium ions in ceria/lanthana solid solutions: comparison between experimental results and a statistical-mechanical model. *Applied Surface Science*, 206(1-4):12 – 19, 2003.

[WSA06] J.R. Wilson, D.T. Schwartz, and S.B. Adler. Nonlinear Electrochemical

Impedance Spectroscopy for Solid Oxide Fuel cell Cathode Materials. *Electrochimica Acta*, 51(8-9):1389–1402, 2006. Electrochemical Impedance Spectroscopy - Selection of papers from the 6th International Symposium (EIS 2004) 16-21 May 2004, Cocoa Beach, FL, USA.

[ZWTL01] Z. Zhan, T.-L. Wen, H. Tu, and Z.-Y. Lu. AC Impedance Investigation of Samarium-Doped Ceria. *Journal of The Electrochemical Society*, 148(5):A427–A432, 2001.